



UNIVERSITÀ
DEGLI STUDI
DI TRIESTE

Dipartimento di Fisica

CORSO DI LAUREA MAGISTRALE IN FISICA

Curriculum FISICA NUCLEARE E SUBNUCLEARE

TESI DI LAUREA MAGISTRALE

Application of the Dry Laser Cleaning technology
to gravitational-wave interferometers

Laureanda:
Chiara Leoni

Relatore:
Prof. Edoardo Milotti

Correlatori:
Dr. Livia Conti
Dr. Andrea Moscatello

ANNO ACCADEMICO 2024-2025

Abstract

Italian abstract

Gli interferometri per la rivelazione delle onde gravitazionali sono tra gli strumenti più avanzati e precisi mai costruiti. Sin dalla prima rivelazione nel 2015, hanno permesso l'osservazione di eventi cosmologici con straordinaria sensibilità, e la collaborazione LIGO-Virgo-KAGRA sta lavorando per minimizzare ogni possibile sorgente di rumore. La prestazione di questi strumenti dipende fortemente dalla pulizia e dalla qualità dei loro componenti ottici, e contaminanti come particelle di polvere o film sottili sulle superfici degli specchi possono degradare in modo significativo i segnali generando luce diffusa.

Questa tesi esplora l'applicazione della tecnica di Dry Laser Cleaning alle superfici delle ottiche degli interferometri, con l'obiettivo di rimuovere particelle contaminanti senza entrare in contatto con la superficie, e senza danneggiare gli specchi. È presentata un'analisi dei meccanismi fisici alla base dell'interazione laser-particella e laser-substrato, includendo le forze di adesione, il trasferimento di calore e i meccanismi di rimozione delle particelle.

I risultati sperimentali mostrano l'efficacia della pulizia con laser impulsato nella rimozione di particelle dell'ordine del micrometro da substrati di soda-lime glass, e la sua dipendenza dalla densità di energia incidente e dal numero di impulsi utilizzato.

Questi test offrono un punto di partenza per studi più avanzati con l'obiettivo di migliorare la prestazione dei componenti ottici nei rivelatori di onde gravitazionali della prossima generazione.

English abstract

Gravitational-wave (GW) interferometers are one of the most advanced and precise detectors ever built. Since the first detected signal in 2015, they have been enabling the observation of cosmic events with extraordinary sensitivity, and the LIGO-Virgo-KAGRA collaboration is making an effort to minimize any possible noise source. The performance of these instruments strongly depends on the cleanliness and quality of their optical components, and contaminants such as dust particles or thin films on mirror surfaces can significantly degrade the signals by generating stray light.

This thesis explores the application of the Dry Laser Cleaning technique to the surfaces of the interferometer optics, aiming to contactless remove particulate contaminants without damaging the mirrors. An analysis of the physical mechanisms underlying laser-particle and laser-substrate interactions is presented, including adhesion forces, heat transfer and particle removal mechanisms.

Experimental results show the effectiveness of pulsed laser cleaning in removing micrometer-sized particles from soda-lime glass substrates, and its dependence on incident energy density and pulse number.

These tests offer a starting point for more advanced studies aimed at improving the performance of optical components in next-generation gravitational-wave detectors.

Contents

Abstract	2
1 Introduction	5
2 Gravitational waves detection	6
2.1 Physics of gravitational waves	6
2.1.1 General relativity and weak field approximation	6
2.1.2 Polarizations of gravitational waves	8
2.2 Astrophysical sources of gravitational waves	10
2.2.1 Maximum strain for CBC systems	11
2.2.2 GW transient catalog	12
2.3 GW interferometers	12
2.3.1 Michelson interferometer	13
2.3.2 Lock-in detection	14
2.3.3 Fabry-Perot cavity	15
2.4 Noise sources	18
2.4.1 Quantum noise	19
2.4.2 Other noise sources	21
3 Stray light noise	23
3.1 Stray light as a noise source	23
3.2 Characterization of light scattering	24
3.2.1 Light scattering by surface roughness	25
3.2.2 Light scattering by dust particulates	27
4 Laser cleaning technology	33
4.1 Adhesion force	33
4.2 Laser-matter interaction	37
4.3 Main physical laser cleaning processes	38
4.4 Laser cleaning dependence on laser parameters	39
4.5 Estimates of thermal stress and radiation pressure	40
4.5.1 Absorbed energy and temperature rise	42
4.5.2 Force due to thermal stress	44
4.5.3 Force due to radiation pressure	46
5 Tests of Dry Laser Cleaning	48
5.1 Laser source	48
5.1.1 N ₂ flux	49
5.2 Preparation of the samples	50
5.3 Laser processing	51

6 Analysis of the samples	54
6.1 Microscope	54
6.1.1 Software for particle recognition	55
6.2 Automation of photo acquisition	56
6.3 DLC experiment and analysis procedure	56
6.4 Analyzed quantities: PAC and NoP	64
6.5 Luminosity threshold study	64
6.6 Particles' diameter distributions	66
6.7 Comparison of PAC and NoP before and after processing	71
6.8 Cleaning efficiency for a fixed diameter range	73
6.9 Study of the small particles	74
6.9.1 Circularity	75
6.9.2 Raman spectroscopy on the smaller particles	80
7 Conclusion	83
7.1 Future perspectives	84
A Setup photos	85
B Photos of the samples	86
C Analysis plots	91
C.1 Luminosity threshold 200 plots	96
C.1.1 PAC/NoP ratio	96

Chapter 1

Introduction

One of the most important goals of the gravitational waves community is to increase the sensitivity of the interferometers of the LIGO-Virgo-KAGRA collaboration at the lowest frequencies. Improvements to the detectors are implemented between the observation runs to increase the sensitivity and to detect weaker signals coming from more distant sources. As progress is made, we expect to achieve a better reconstruction of the source parameters and detect signals from the merging of black holes with higher masses. Stray light represents one of the main noise sources in the low-frequency band, therefore it is crucial to characterize and control the experimental facilities in order to minimize contributions to scattered light. A recent area of research involves studying stray light caused by dust particles in the environments of the Virgo interferometer. Ideally, we would be able to model and predict noise caused by scattered light and limit dust contamination in the clean environments of the detectors as much as possible.

This thesis aims to propose a new method of cleaning the Virgo interferometer's optics through an exploratory study of the Dry Laser Cleaning technique applied to glass substrates. To do so, soda-lime glass microscope slides with dust deposited on them are processed and analyzed. The laser used is a KrF excimer laser of the Physics and Astronomy Department of University of Padova, while the samples are imaged and analyzed using a digital microscope in the clean room of the Virgo group in Padova.

First, Chapter 2 provides an overview on the physics of gravitational waves: starting with the theory behind them, moving on to the astrophysical sources, and finally describing interferometric detectors. Chapter 3 defines stray light as a noise source and presents how stray light from dust particles is modeled. In Chapter 5 we give a description of the experimental setup, particularly the laser source, and we describe how the samples are prepared and processed. Finally, in Chapter 6 we discuss the analysis results, explain some unexpected phenomena observed and describe the tests conducted to study them.

Chapter 2

Gravitational waves detection

Before the first detection of a gravitational-wave (GW) event, GW150914, electromagnetic radiation and neutrinos were the primary messengers used to study the Universe. These signals can provide different, but complementary information [1].

Gravitational waves provide a completely new observational window on the Universe and open new avenues for exploring astrophysical sources. Consisting of ripples in the fabric of space-time, they emanate from many different kinds of sources, such as colliding black holes, which are mostly invisible to electromagnetic detectors.

A key feature of gravitational waves detected on Earth is their extreme weakness. This means that exploring signals coming from the deepest reaches of the Universe and studying times that have never been explored before — such as the period before the universe became transparent to radiation — requires a global minimization of all noise sources. If we can achieve this, we will be able to detect signals coming from regions of the universe that lie deeper in space and time.

In this chapter, Sect. 2.1 outlines the physical characteristics of gravitational waves, including their origin and the types of signals that we expect to detect. Sect. 2.2 presents the primary astrophysical sources capable of producing gravitational waves, including those that have already been observed and those that are anticipated for the future. An overview of the current status of the observed signals is also provided. This explains why gravitational wave interferometers must have certain properties and why eliminating potential sources of noise is crucial.

2.1 Physics of gravitational waves

2.1.1 General relativity and weak field approximation

General relativity (GR) is based on three key principles, formulated by A. Einstein in 1915. The principle of general covariance is an extension of the principle of relativity (one of the postulates of special relativity), which states that the laws of physics are the same in any inertial reference frame. In GR it is required that the laws of physics should be the same in all - inertial and accelerating- frames. This means that physical phenomena should not depend on the choice of the coordinate system used to describe them. The principle of consistency says that a new theory must reduce to an old one if what the old one states has been successfully verified experimentally. In the case of GR, this means that, in the weak-field and low-speed limit, it should follow the laws of Newtonian mechanics, while in the absence of gravity, it should reduce to special relativity. The principle of equivalence has two main facets. The first one is referred to as the Weak Equivalence Principle (WEP),

which states that the property of a body called "mass" is proportional to its "weight". This means that, for example, in the simplest case of dropping two different bodies in a gravitational field, they both fall with the same acceleration. The Einstein Equivalence Principle is a more powerful concept, since it states that:

1. WEP is valid
2. The outcome of a local non-gravitational experiment is independent of the velocity of the free-falling reference frame in which it is performed (Local Lorentz Invariance)
3. The outcome of a local non-gravitational experiment is independent of where and when it is performed (Local Position Invariance).

If EEP is valid, then gravitation must be a "curved spacetime" phenomenon. Mathematically, this means that we must turn to the so-called Riemann manifolds. An N -dimensional manifold has points that can be labeled by a system of coordinates $x^1, x^2 \dots, x^N$, so that the correspondence between the points and the labels is one-to-one. It can be embedded in a larger space and display extrinsic curvature, or it can exist without any embedding and display intrinsic curvature. A Riemann manifold can be described as a smoothly curved space locally flat. The metric tensor $g_{\mu\nu} = \mathbf{e}_\mu \cdot \mathbf{e}_\nu$ contains all the necessary information to describe the curvature of a manifold. The metric tensor is symmetric ($g_{\mu\nu} = g_{\nu\mu}$), and Riemann manifolds have positive defined metric. Actually, the manifolds of general relativity are pseudo-Riemann because the metric is not positive-defined. When formulating the main equation of general relativity, Einstein knew that there should have been a source term, since the idea is that curvature is related to the presence of mass/energy. This is described by the stress-energy tensor $T_{\mu\nu}$, and the interaction between spacetime geometry and the energy momentum is completely described by Einstein's Field Equations:

$$R_{\mu\nu} - \frac{1}{2}g_{\mu\nu}R = \frac{8\pi G}{c^4}T_{\mu\nu} \quad (2.1)$$

where G is the universal gravitational constant, c is the speed of light and $R_{\mu\nu}$ and R are the Ricci tensor and the Ricci scalar respectively. These two terms are defined as follows:

$$R_{\mu\nu} = R_{\mu\alpha\nu}^\alpha \quad (2.2)$$

$$R = g^{\mu\nu}R_{\mu\nu} \quad (2.3)$$

where $R_{\nu\rho\sigma}^\mu$ is the Riemann tensor and is defined as:

$$R_{\nu\rho\sigma}^\mu = \partial_\rho\Gamma_{\nu\sigma}^\mu - \partial_\sigma\Gamma_{\nu\rho}^\mu + \Gamma_{\alpha\rho}^\mu\Gamma_{\nu\sigma}^\alpha - \Gamma_{\alpha\sigma}^\mu\Gamma_{\nu\rho}^\alpha \quad (2.4)$$

and the Christoffel symbols (or connection coefficients) are defined from the metric tensor:

$$\Gamma_{\mu\nu}^\rho = \frac{1}{2}g^{\rho\sigma}(\partial_\mu g_{\sigma\nu} + \partial_\nu g_{\sigma\mu} - \partial_\sigma g_{\mu\nu}) \quad (2.5)$$

Eq. 2.1 directly connects the space-time geometry to the source of the curvature, since the left-hand side of the equation depends only on the metric tensor $g_{\mu\nu}$, while the right-hand side depends on the stress-energy tensor $T_{\mu\nu}$.

In order to study this set of non-linear differential equations, we can consider the weak-field limit, which allows us to say that the metric tensor is approximately equal to $\eta_{\mu\nu}$ (flat

Minkowski metric, $\eta_{\mu\nu} = \text{diag}(-1, 1, 1, 1)$, and add a small perturbation $h_{\mu\nu}$, such that $|h_{\mu\nu}| \ll 1$:

$$g_{\mu\nu} \simeq \eta_{\mu\nu} + h_{\mu\nu} \quad (2.6)$$

This is a reasonable approximation, since from Eq. 2.1:

$$\frac{8\pi G}{c^4} \simeq 10^{-43} s^2 m^{-1} kg^{-1} \quad (2.7)$$

which means that space-time is very hard to bend, since it takes a huge amount of matter to generate a very small curvature.

To further simplify things, trace-reversed perturbation variables are introduced:

$$\bar{h}_{\mu\nu} = h_{\mu\nu} - \frac{1}{2}\eta_{\mu\nu}h \quad (2.8)$$

where $h = h^\alpha_\alpha$ is the trace of the linear term in the metric tensor. This leads to the Einstein equation for linearized gravity with trace-reversed perturbation variables:

$$\square^2 \bar{h}_{\mu\nu} - \partial_\mu \partial^\alpha \bar{h}_{\alpha\nu} - \partial_\nu \partial^\alpha \bar{h}_{\mu\alpha} + \eta_{\mu\nu} \partial_\alpha \partial_\beta \bar{h}^{\alpha\beta} = \frac{8\pi G}{c^4} T_{\mu\nu} \quad (2.9)$$

where $\square^2 = \partial^\mu \partial_\mu = \frac{1}{c^2} \frac{\partial^2}{\partial t^2} - \nabla^2$ is the d'Alambertian operator. It can be demonstrated that it is possible to set the Lorentz gauge, meaning that we can fix the coordinate system so that $\partial_\nu \bar{h}^{\mu\nu} = 0$ to further simplify the Einstein equation. In this case, the formula reduces to the following system:

$$\begin{cases} \partial_\nu \bar{h}^{\mu\nu} = 0 \\ \square^2 \bar{h}^{\mu\nu} = \frac{16\pi G}{c^4} T_{\mu\nu} \end{cases} \quad (2.10)$$

The last equation has the form of a wave equation, which means that perturbations of the gravitational field propagate as waves, and they propagate at the speed of light c [2].

2.1.2 Polarizations of gravitational waves

In empty space, the system found in Eq. 2.10 reduces to:

$$\begin{cases} \partial_\nu \bar{h}^{\mu\nu} = 0 \\ \square^2 \bar{h}^{\mu\nu} = 0 \end{cases} \quad (2.11)$$

Eq. 2.11 describes the propagation of metric perturbations that satisfy a wave equation. These perturbations represent gravitational waves. We have to look for solutions in this form:

$$\bar{h}^{\mu\nu} = \text{Re}[A^{\mu\nu} e^{ik_\alpha x^\alpha}] \quad (2.12)$$

these must satisfy three main constraints:

- $A^{\mu\nu} = A^{\nu\mu}$, since the metric tensor is symmetric,
- $k^\alpha k_\alpha = 0$, which means that GWs group and phase velocities are equal to c ,
- $k_\nu A^{\mu\nu} = 0$, which comes from the Lorentz condition and means that GW are transverse waves.

The first and last conditions reduce the degrees of freedom of $\bar{h}_{\mu\nu}$ from 10 (since it is a 4×4 symmetric tensor) to 6.

The Lorentz gauge determines a whole class of gauge transformations, and we can still reduce the degrees of freedom by introducing the Transverse-Traceless Gauge (TT Gauge), defined by:

$$\bar{h}_{TT} = 0 \quad (2.13)$$

This also means that $h = 0$, so in this gauge there is no difference between perturbation variables and trace-reversed perturbation variables.

In all these specific conditions, the generic polarization state can be written as follows:

$$A^{\mu\nu} = A_+ \epsilon_+^{\mu\nu} + A_\times \epsilon_\times^{\mu\nu} \quad (2.14)$$

Where we have defined two linear polarization tensors:

$$\epsilon_+^{\mu\nu} = \begin{pmatrix} 0 & 0 & 0 & 0 \\ 0 & 1 & 0 & 0 \\ 0 & 0 & -1 & 0 \\ 0 & 0 & 0 & 0 \end{pmatrix} \quad \epsilon_\times^{\mu\nu} = \begin{pmatrix} 0 & 0 & 0 & 0 \\ 0 & 0 & 1 & 0 \\ 0 & 1 & 0 & 0 \\ 0 & 0 & 0 & 0 \end{pmatrix} \quad (2.15)$$

To understand how a passing gravitational wave affects matter, we can study the motion of freely falling test particles in the perturbed spacetime. The trajectories of such particles follow geodesics, which are determined by the Christoffel symbols of the perturbed metric through the following equation:

$$\frac{d^2x^\alpha}{d\tau^2} = -\Gamma_{\mu\nu}^\alpha \dot{x}^\mu \dot{x}^\nu \quad (2.16)$$

rewriting the connection coefficients (defined in Eq. 2.5) in linearized gravity and in the TT Gauge, and considering a particle initially at rest (meaning we can write its 4-velocity in the form $\dot{x}^\mu = (c, 0, 0, 0)$), Eq. 2.16 becomes:

$$\frac{d^2x^\alpha}{d\tau^2} = -\Gamma_{\mu\nu}^\alpha \dot{x}^\mu \dot{x}^\nu = -\Gamma_{00}^\alpha c^2 = 0 \quad (2.17)$$

This means that the 4-velocity remains constant and equal to the initial value: individual particles remain stationary in the TT gauge space-time.

However, the relative distance between two neighboring particles does change, since the metric itself is varying with time. If we consider two particles separated by a small spacelike 4-vector $\xi^\mu = (0, \xi^1, \xi^2, \xi^3)$, the spatial separation is not constant:

$$\begin{aligned} \Delta x^2 &= -g_{ij}\xi^i\xi^j = -(\eta_{ij} + h_{ij})\xi^i\xi^j = (\delta_{ij} - h_{ij})\xi^i\xi^j = \\ &= \xi_i\xi^j - h_{ij}\xi^i\xi^j \simeq \left(\xi_i - \frac{1}{2}h_{ik}\xi^k\right)\left(\xi^i - \frac{1}{2}h_k^i\xi^k\right) \end{aligned} \quad (2.18)$$

This indicates that measured distances oscillate as the wave passes, because the metric changes, while the coordinates of test particles remain constant. Here, it is notable that there is no deformation in the propagation direction, correctly meaning that the wave is transverse [3].

To study the effect of these perturbations on a distribution of particles, we consider the geodesic deviation for two very close particles. In the non-relativistic limit for the particles' velocity, we can write the following relation:

$$\frac{d^2\xi^i}{dt^2} = -R_{0j0}^i \xi^j \quad (2.19)$$

But, in the TT Gauge and for linearized gravity, the following equation holds:

$$R_{0j0}^i = -\frac{1}{2}\ddot{h}_{ij}^{TT} \quad (2.20)$$

Putting all together, and integrating twice the geodesic deviation equation in the case the two test particles are originally at rest, we get to the expression for the induced displacement:

$$\delta\xi^i(t) = \frac{1}{2}h_{ij}^{TT}(t)\xi_0^j \quad (2.21)$$

Applying this formula to the particular case of a GW with angular frequency ω and a ring of particles so that:

$$z_0 = 0 \quad (2.22)$$

$$x_0 + y_0 = R_0 \quad (2.23)$$

We can move to polar coordinates (r, ϕ) to describe the particles on the ring and show that:

$$\frac{R(\phi, t)}{R_0} = 1 + \frac{h_+}{2}e^{i\omega t}(\cos^2\phi - \sin^2\phi) + \frac{h_\times}{2}e^{i\omega t}\cos\phi \cdot \sin\phi \quad (2.24)$$

Fig. 2.1 shows the separate effect of the + and \times polarizations.

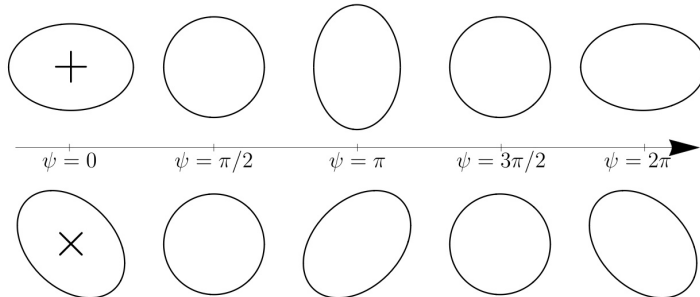


Figure 2.1: Effect of a GW on the proper distance from the origin to a circular ring of freely falling particles. The top row shows a + polarized GW ($h_+ \neq 0$ and $h_\times = 0$), the bottom row shows a cross polarized GW ($h_\times \neq 0$ and $h_+ = 0$). Time increases from left to right and the effect is shown for different values of the GW phase $\psi = \omega t$. Figure from [4].

2.2 Astrophysical sources of gravitational waves

The classification of astrophysical sources of gravitational waves is based on the type of signal that they emit: generally, it can be transient, continuous, or stochastic. Transient signals range from a few milliseconds to several minutes. They can be generated by short-lived events, such as a supernova explosion, or by events that last very long periods of

time, and of which we can observe only the final state, such as compact binary coalescences (CBC), which consist of the merger of binary systems of black holes or neutron stars. A signal that is classified as continuous can last months or even years. In general, these are weaker than the ones generated from a coalescence, but since they last so long it is possible for us to accumulate the signal in stretches of data. A typical source of a continuous signal could be a non-axisymmetric spinning object, such as a neutron star, even though they have never been detected so far. Finally, stochastic background results from the overlap of many gravitational-wave signals that are too weak to be detected individually, and it also may include signals that could come from the very early universe, approximately 10^{-36} to 10^{-32} seconds after the Big Bang. In this case, managing to detect these types of signal more precisely could enable us to explore a piece of history of the Universe that we are currently unable to investigate experimentally. [5]

2.2.1 Maximum strain for CBC systems

In order to understand the nature of the signals we expect to detect, we must first study the types of strain that a system of two rotating objects can produce. Looking back at Eq. 2.10, the solution is known from the general case in vacuum, and it is based on retarded potential. Under special conditions (source size $\ll \lambda \ll$ distance from the source r , $|\bar{h}^{\mu\nu}| \ll 1$ and the speed of the source is $\ll c$), we can write it as follows:

$$\bar{h}^{\mu\nu}(ct, \vec{x}) \simeq \frac{4G}{c^4 r} \int T^{\mu\nu}(ct - r, \vec{x}') d^3 \vec{x}' \quad (2.25)$$

Integrating and making some consideration, we can get to another form of the solution:

$$\bar{h}^{ij}(ct, \vec{x}) \simeq \frac{2G}{c^4 r} \ddot{Q}^{ij}(t - r/c) \quad (2.26)$$

where Q^{ij} is the quadrupole tensor of the mass distribution, and it is defined as follows:

$$Q^{ij} = \int \rho x^i x^j d^3 \vec{x} \quad (2.27)$$

We can evaluate this term in the case of a binary system, where one object orbits around the other in a circle of radius R . This leads to:

$$\bar{h}^{ij}(ct, \vec{r}) = \frac{4G(m_1 r_1^2 + m_2 r_2^2)\omega^2}{c^4 r} \begin{pmatrix} \cos(2\omega t + \phi) & \sin(2\omega t + \phi) & 0 \\ \sin(2\omega t + \phi) & -\cos(2\omega t + \phi) & 0 \\ 0 & 0 & 0 \end{pmatrix} \quad (2.28)$$

from this formula, we can derive the maximum strain:

$$h_{max} = \frac{4G(m_1 r_1^2 + m_2 r_2^2)\omega_0^2}{c^4 r} = \frac{4G^{\frac{5}{3}}}{c^4 r} \frac{m_1 m_2}{(m_1 + m_2)^{\frac{1}{3}}} \omega_0^{\frac{2}{3}} \quad (2.29)$$

where ω_0 is the maximum frequency, that can be obtained from the assumption that the distance between the two masses is equal to the sum of the Schwarzschild radii (for a system of two black holes). Doing the calculation for two black holes with 1 solar mass each and at the distance of the Virgo galaxy cluster, we obtain a maximum strain $h_{max} \simeq 2.9 \cdot 10^{-21}$. [6]

The strain h obtained in Eq. 2.29 represents the dimensionless fractional change in distance between two freely suspended test masses: $h = \Delta L/L$. In other words, a passing

GW periodically stretches and squeezes space, causing the length of an interferometer arm (see Sect. 2.3) to oscillate by a small amount ΔL . For an interferometric detector with orthogonal arms, a + polarized wave increases the length of one arm while decreasing that of the other, producing a measurable differential displacement. This means that the metric perturbation h derived above is directly observable as the relative change in the interferometer arm length. For example, with the obtained $h_{max} \simeq 2.9 \cdot 10^{-21}$ and an arm length of $L = 3$ km, the expected displacement is extremely small, of the order of 10^{-18} m.

2.2.2 GW transient catalog

On the 26th of August 2025 the interferometric strain data from the first part of the fourth observing run (O4a) were released in the transient catalog GWTC-4.0 [7]. It covers the period from 24th of May 2023 to 16th of January 2024. The release was announced by the Ligo-Virgo-Kagra collaboration. With the addition of 128 new candidate events, the cumulative catalog now contains over 200 confirmed sources, including binary black holes (BBH), binary neutron stars (BNS) and neutron star-black hole systems (NSBH). GWTC-4.0 provides astrophysical parameters of the events (masses, spins, distances, etc.) and the interferometric strain data [8]. This represents the most comprehensive dataset available to date for gravitational wave astronomy.

A series of milestone events are mentioned here:

- GW150914: the first ever GW signal detected. It was detected by the two LIGO detectors on the 14th of September 2015. The source was a coalescing black holes binary, with masses equal to $36M_\odot$ and $29M_\odot$. This event confirmed the existence of such systems and Einstein's prediction on the existence of gravitational waves. This detection led to the awarding of the 2017 Nobel prize to Rainer Weiss, Barry C. Barish and Kip S. Thorne, "for decisive contributions to the LIGO detector and the observation of gravitational waves".
- GW170817: this event has two characteristics that make it important for the history of GW detection. Firstly, it was the first detected event of a binary neutron stars system (BNS). Secondly, for the first time the same event was detected through two different messengers: a gamma-ray burst (GRB 170817A) was detected by INTEGRAL and FERMI 1.7s after the GW signal. This started the search of EM counterparts for GW events, and marked the birth of multimessenger astronomy.
- GW190521: the detection of a merger of two black holes, characterized by a final remnant mass of $142^{+28}_{-16}M_\odot$, which classifies it as a black hole of intermediate mass.
- GW231123: the most massive binary black hole event observed so far. The two starting black holes had masses equal to $137M_\odot$ and $103M_\odot$, and their coalescence produced a black hole of $\sim 225M_\odot$.

2.3 GW interferometers

When trying to detect gravitational wave signals, the aim is to measure changes in relative distance between two masses. In this case, a Michelson interferometer is ideal, since it allows to measure length differences of two perpendicular arms through interference patterns. In this section, I briefly explain how GW interferometers work and the main levels

of complexity that need to be added to successfully isolate the signal and achieve ideal detection.

2.3.1 Michelson interferometer

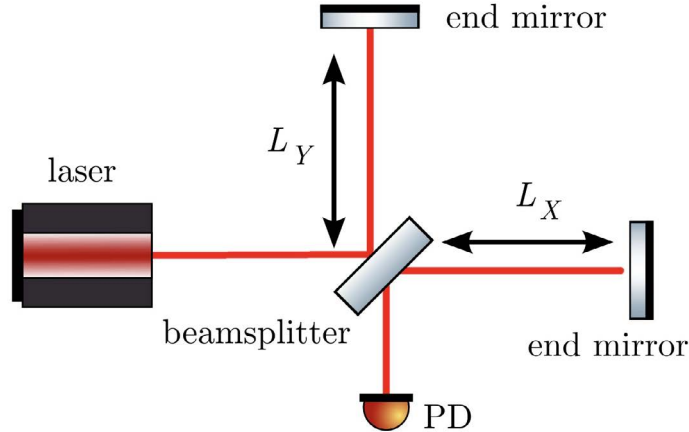


Figure 2.2: Simplified scheme of a Michelson interferometer. Figure from [9].

Fig. 2.2 shows the main scheme of a Michelson interferometer. A laser provides the input light, which is then split into two beams by a beam splitter (BS). At this point the two separate beams travel two distances L_X and L_Y , reflect off the end mirrors, and recombine at the BS. Depending on the difference of the phases induced by the difference of the two traveled lengths, the interference pattern measured at the photodetector changes accordingly.

A given spatial component of the field of the input laser light is written as:

$$E_{in} = E_0 e^{-i\omega_L t + ik_L \cdot x} \quad (2.30)$$

where E_0 is the amplitude of the electric field, ω_L is the frequency of the laser and k_L is the wave vector. If we work with a symmetric beam splitter, so that reflectance and transmittance are, respectively, $R = \frac{1}{2}$, $T = \frac{1}{2}$, and the end mirrors are highly reflective, we can write the expression for the two electric fields that recombine at time t at the output port after traveling the two arms:

$$E_1 = -\frac{1}{2} E_0 e^{-i\omega_L t + 2ik_L L_x} \quad (2.31)$$

$$E_2 = +\frac{1}{2} E_0 e^{-i\omega_L t + 2ik_L L_y} \quad (2.32)$$

Then, the total output electric field is simply $E_{out} = E_1 + E_2$. We can see that:

$$E_{out} = -E_0 e^{-i\omega_L t + ik_L (L_x + L_y)} \sin[k_L (L_x - L_y)] \quad (2.33)$$

This takes into account the additional minus sign contributed by the BS only in the y direction, because the reflection on the BS coating takes place on the substrate side. The power measured by the photodetector (PD) is:

$$P_{out} = |E_{out}|^2 = \sin^2[k_L (L_x - L_y)] P_{in} \quad (2.34)$$

Eq. 2.34 tells us that a variation in the arm lengths results in a variation of the power at the PD, and this is the idea behind the GW detection through an interferometer, since a gravitational wave causes a ripple in space-time that can stretch or contract the arms of the structure.

We can now visualize the effect of a certain polarization of a GW passing through the interferometer. First, let us define the transfer function of the interferometer:

$$H(\omega) = \frac{E_{out}}{E_{in}} = -ie^{ik_L(L_x+L_y)} \sin[k_L(L_x - L_y)] \quad (2.35)$$

If we have a GW with + polarization with respect to the interferometer arms, this means that the two arms stretch so that $L_x \rightarrow L_x + L_x \frac{h}{2}$ and $L_y \rightarrow L_y - L_y \frac{h}{2}$. Then, we can write the output power in the following way:

$$P_{out} = \sin^2[k(\delta L + Lh)]P_{in} \quad (2.36)$$

where we have defined:

$$L = \frac{L_x + L_y}{2} \quad (2.37)$$

$$\delta L = L_x - L_y \quad (2.38)$$

If we assume that the gravitational wave strain is sufficiently small, so that $kLh \ll 1$, we can expand the expression in 2.36 and obtain:

$$P_{out} \simeq P_{in} \sin^2(k\delta L) + P_{in} \left(\frac{d}{du} \sin^2 u \Big|_{u=k\delta L} \right) kLh + \frac{1}{2} P_{in} \left(\frac{d^2}{du^2} \sin^2 u \Big|_{k\delta L} \right) k^2 L^2 h^2 \quad (2.39)$$

We can choose an operating point and look at the perturbation in P_{out} around that point due to the gravitational wave. Intuitively, we would want to work at the point where the slope of the power curve as a function of δL is maximum, since this would maximize the effect of the gravitational wave on the output power. At this point $k\Delta L = \pi/4$, and:

$$P_{out} \simeq \frac{P_{in}}{2} (1 - 2kLh) \quad (2.40)$$

The problem here is that we are left with a large dc term; $\frac{P_{in}}{2}$, which means that both the photon shot noise and the laser relative intensity noise are quite large. To avoid this, we could choose to work at the dark fringe (the null point), where $k\delta L = n\pi$. In this case, the output power is:

$$P_{out} \simeq P_{in}(kLh)^2 \quad (2.41)$$

Now we do not have a dc term, but we have a signal that is $\propto h^2$, which means it is impossibly difficult to detect because of the typical order of magnitude of h . [10].

2.3.2 Lock-in detection

In order to work at the null point, we need to introduce a modulation in the phase, so that we can linearize the interferometer response. We can consider an input field in the following form:

$$\begin{aligned} E_{in} &= E_0 e^{i(\omega t + \beta \sin \Omega t)} \\ &\simeq E_0 [J_0(\beta) e^{i\omega t} + J_1(\beta) e^{i(\omega + \Omega)t} - J_1(\beta) e^{i(\omega - \Omega)t}] \end{aligned} \quad (2.42)$$

This is practically done by adding the so-called Pockels cells, made out of dielectric materials that have a refractive index that depends on the applied electric field.

The output field will now depend on the transfer function evaluated at three different frequencies:

$$E_{out} = E_0 \left(H_0 J_0(\beta) e^{i\omega t} + H_+ J_1(\beta) e^{i(\omega + \Omega)t} - H_- J_1(\beta) e^{i(\omega - \Omega)t} \right) \quad (2.43)$$

where we have defined $H_0 = H(\omega)$, $H_+ = H(\omega + \Omega)$ and $H_- = H(\omega - \Omega)$. Here, the term proportional to $J_0(\beta)$ is called the carrier, while the other two terms are called sidebands. In order to obtain a non-vanishing detector response at the side bands, we add a small length asymmetry between the two arms, called Schnupp asymmetry, so that $\cos(k\delta L) = 1$ and $\sin(k\delta L) = 0$. In this way interference is still destructive for the carrier, but not for the sidebands. Carrying out all the calculations, we find that the power at the output of the interferometer has a final expression with two terms in dc and two terms oscillating at Ω and 2Ω . The term oscillating at Ω is the one of interest to us, since it is proportional to the gravitational wave strain h . In order to measure the signal, we know that the PD response is proportional to the output power, and after some mixing, averaging and low-pass filtering, we obtain the expression for the final output signal as a function of the strain h :

$$V_{\text{signal}}(h) = 2R J_0(\beta) J_1(\beta) \sin\left(\frac{\Omega}{c}\delta L\right) \frac{2\pi L}{\lambda} h \quad (2.44)$$

where R is the responsivity of the PD. This means that we have successfully linearized the response of the interferometer around the dark fringe, and now we can work at this point to minimize noise.

2.3.3 Fabry-Perot cavity

An additional element that helps increasing the sensitivity of the interferometer is the Fabry-Perot cavity, that is placed in each arm of the Michelson interferometer. In order to do this, we have to add another mirror before the end mirror in each arm, so that we have two resonant cavities. The idea is that light can bounce multiple times between the two mirrors, and this increases the effective length of the arms, meaning that the effect of a gravitational wave is amplified. The principle is illustrated in Fig. 2.3. Considering two mirrors with equal transmission and reflection coefficients, t and r , and no absorption, we find the expression for the transmitted intensity:

$$I_T = |E_T|^2 = I_0 \frac{t^4}{|1 - r^2 e^{i\delta}|^2} \quad (2.45)$$

where $\delta = \frac{4\pi L}{\lambda}$ is the round-trip phase, and I_0 is the input intensity. We can rewrite the expression in the following way:

$$I_T = I_0 \frac{T^2}{|1 - R e^{i\Delta}|^2} \quad (2.46)$$

where the transmittance and reflectance are defined as $T = |t|^2$ and $R = |r|^2$, and Δ is the total phase difference. With further calculations, we find that:

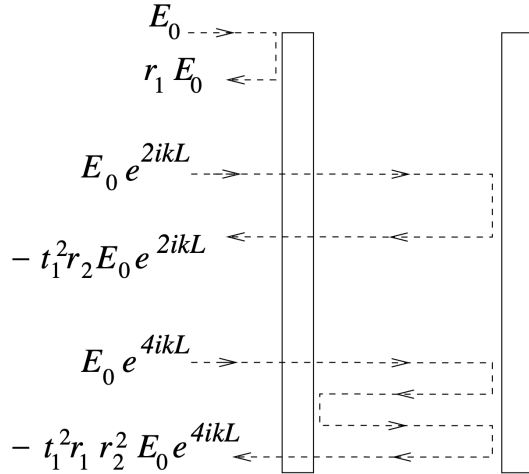


Figure 2.3: Scheme of a Fabry-Perot cavity, with an incoming electric field E_0 and two mirrors with transmission and reflection coefficients t_1, r_1 and t_2, r_2 respectively. Figure from [11].

$$\begin{aligned}
 I_T &= \frac{I_0 T^2}{(1-R)^2} \frac{1}{1 + \frac{4R\sin^2\Delta/2}{(1-R)^2}} \\
 &= \frac{I_0 T^2}{(1-R)^2} \frac{1}{1 + F\sin^2\Delta/2} \\
 &= \frac{I_0 T^2}{(1-R)^2} f(\Delta)
 \end{aligned} \tag{2.47}$$

where we have defined the coefficient of finesse $F = \frac{4R}{(1-R)^2}$ and the Airy function $f(\Delta) = \frac{1}{1+F\sin^2\Delta/2}$. $f(\Delta)$ can also be defined through the finesse, which has the following expression:

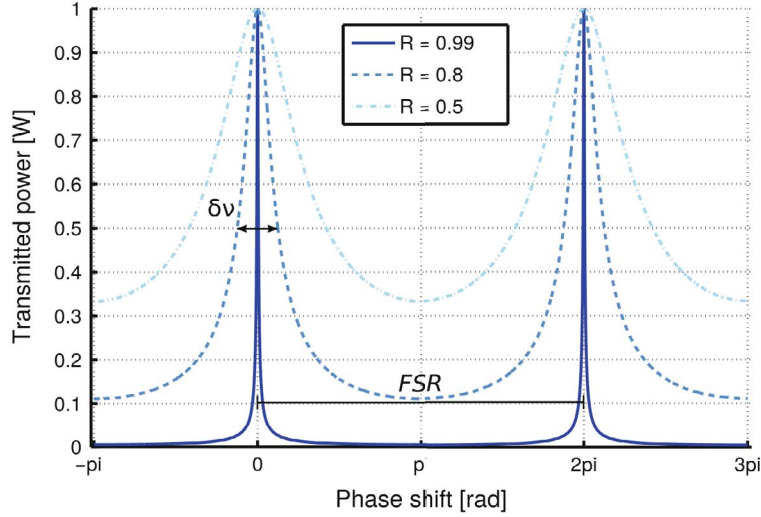
$$\mathcal{F} = \frac{\pi\sqrt{R}}{1-R} \tag{2.48}$$

and it gives us information on the sensitivity of the cavity to variations of its length or of the wavelength.

The Airy function has peaks when $\Delta = m2\pi$, with m integer, that correspond to the resonance condition, and the distance between two peaks is called Free Spectral Range (FSR). In Fig. 2.4 it can be seen how its shape changes with different values of R . In our case, since $\Delta/2 = kL$ with L being the distance between the two mirrors that make the cavity, we can find the relation between the peak width, the FSR and the finesse. In particular, we have:

$$\delta\nu = \frac{\text{FSR}}{\mathcal{F}} \tag{2.49}$$

By making an analogy with the harmonic oscillator, we can find the average number of back and forth passages of a photon inside the cavity. Recalling that the quality factor for a harmonic oscillator is defined as $Q = \frac{\omega_0}{\Gamma}$ and $\tau = 1/\Gamma$, in the same way we can find

Figure 2.4: Airy function for different values of R .

the "photon lifetime" inside the cavity as $\tau = \frac{1}{2\pi\delta\nu}$, and the average number of passes in the cavity: $n = \frac{c\tau}{2L} = \text{FSR}\tau = \frac{\mathcal{F}}{2\pi}$. This means that the effective length of the cavity is $L_{\text{eff}} = n \cdot L = \frac{\mathcal{F}}{2\pi}L$.

We can easily generalize the expression for the Finesse, found in Eq. 2.48 in the case of mirrors with unequal reflection coefficients:

$$\mathcal{F} = \frac{\pi\sqrt{r_i r_e}}{1 - r_i r_e} \quad (2.50)$$

With some calculations, it can be seen that the complex amplitude reflection coefficient of the cavity can be written so that it represents a circle in the complex plane, with its center and radius dependent on the reflection and transmission coefficients of the input and end mirror. There are now three cases that we need to consider: $r_i = r_e$, $r_i < r_e$ and $r_i > r_e$. In all of these situations, far from resonance the reflection coefficient is close to -1, and does not move that much if we change L or λ . Getting closer to resonance condition, the phase moves more rapidly towards the resonance point (achieved for a reflection coefficient equal to +1). This is the main reason why we want to work at resonance in our gravitational waves detectors: we have the highest sensitivity to changes in length differences.

If $r_i = r_e$, at resonance, all the light gets inside the cavity, none of it is reflected back. This happens when the amount of light that manages to get inside the cavity is exactly equal to the one that leaks from the cavity due to internal losses. This is the case of a critically coupled cavity. If $r_i < r_e$, the amount of light that the ITM (input test mass) allows inside the cavity is greater than the one that leaks: at each passage of the light inside the arm, the cavity accumulates more power until an equilibrium is reached. This is known as the overcoupled case. Finally, if $r_i > r_e$, too much light is reflected by the ITM and little light is transmitted through the cavity on resonance. This is what happens in undercoupled cavities.

Virgo mirrors work in the overcoupled regime, because we need the cavity to act as a tunable mirror in place of the single mirror of a standard Michelson interferometer where the light of the carrier enters the FP cavity while the sidebands are reflected by the input mirror. The mirrors have very low internal losses, and we need mirrors that are almost perfectly reflective. The precise values in Virgo are: $r_i = 0.993$, $r_e = 0.999998$, which gives

a Finesse $\mathcal{F} \simeq 450$.

By calculating the amplitude reflection coefficient at resonance, and considering losses due to mirror defects, we find the complete expression for the reflectance for the carrier:

$$r_{x,y} = \left(1 - \frac{\mathcal{F}}{\pi}\epsilon\right) \left(1 + 8i\mathcal{F}\frac{\delta L_{x,y}}{\lambda}\right) \quad (2.51)$$

where ϵ is the average loss per single pass and $\delta L_{x,y} = \pm h/2$. The sidebands are completely reflected by the input mirror. After taking into account the Schnupp asymmetries, one finds the following expression for the output power:

$$P_{out}(\Omega) = P_{in} \left[16J_0(\beta)J_1(\beta)\sin\left(\frac{\Omega}{c}\delta L\right)\mathcal{F}\frac{L}{\lambda}\left(1 - \frac{\mathcal{F}}{\pi}\epsilon\right)h \right] \quad (2.52)$$

Power recycling

An additional improvement in the interferometer scheme is the power recycling mechanism. Since we are working at the dark fringe of the carrier, when there is no signal, all the light at frequency ω is reflected back to the laser and would be lost. The idea is to recycle this light by placing a mirror between the laser source and the BS to reflect the light back into the interferometer. This creates a new Fabry-Perot cavity, made by the added mirror and the rest of the interferometer with its FP arms. At this point, the input power increases by a factor that is proportional to the finesse of the new cavity, since it is arranged to be resonant for the input laser light. [11]

2.4 Noise sources

The output of a GW detector discussed in the previous sections would be a combination of a true GW signal and different noise contributions. Since we are expected to detect arm length differences of the order $\delta L \sim hL \sim 3 \cdot 10^{-18}$ m, where L is the Virgo arm length of 3 km, it is crucial to be able to control mechanical noise at this level. This is also strongly connected to all the interferometer characteristics already discussed that aim to increase the signal amplitude: in this way, we are increasing the signal-to-noise ratio SNR (ratio between the effective signal amplitude and RMS noise amplitude). The sensitivity curve takes into account all the noise sources and describes the overall sensitivity of the detector. This curve represents the strain obtained after summing all the noise sources, as a function of the frequency, since the amplitude of a GW signal changes with frequency. Fig. 2.5 shows the theoretical noise budget for Advanced Virgo during the second observing run (O2).

The main types of noise are: quantum noise (with its two facets, shot noise and radiation pressure noise), thermal noise, noise due to ground vibration and noise due to stray light, which is the main focus of this thesis and is discussed in Chapter 3.

In order to study these processes, it is useful to introduce the Power Spectral Density (PSD). For a stationary noise process, $S_m(\omega)$ can be obtained from the Fourier transform of the auto-correlation function:

$$S_n(\omega) = \int_{-\infty}^{+\infty} \langle n(t)n(t + \tau) \rangle e^{-i\omega\tau} d\tau \quad (2.53)$$

the process n represents noise, and the corresponds to the strain h caused only by noise. The PSD gives us an idea of how much noise we have at each frequency.

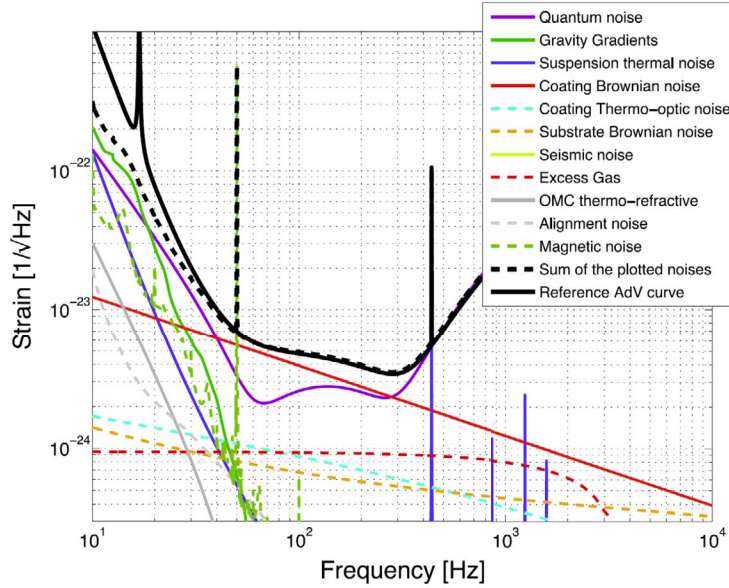


Figure 2.5: Sensitivity curve for the AdV detector. Different colors represent different noise sources. The dashed black line corresponds to the sum of all the noise contributions, while the solid black line is a reference AdV sensitivity. Figure from [12]

2.4.1 Quantum noise

The first type of quantum noise, shot noise, comes from the fact that laser light is quantized in photons, and they arrive randomly. This contribution can be reduced by increasing the laser power; however, this leads to another problem. Due to its quantum nature, shot noise has its corresponding conjugate noise. This is given by the radiation pressure of the photons on the mirrors, which produces a stochastic force that shakes the mirrors and becomes more important at higher laser power.

Let us consider a number of photons N_γ that arrive on the photodetector in a certain observation time T . The average measured power during this time is:

$$P = \frac{1}{T} N_\gamma \hbar \omega_L \quad (2.54)$$

Since we are counting a discrete independent events, the outcome follows the Poisson distribution. This means that, if we consider a large number of photons arriving on the mirror surface, the fluctuation in the number of photons will be given by:

$$\Delta N_\gamma = \sqrt{N_\gamma} \quad (2.55)$$

This leads to a fluctuation of laser power given by:

$$\begin{aligned} \Delta P &= \frac{1}{T} \sqrt{N_\gamma} \hbar \omega_L \\ &= \left(\frac{\hbar \omega_L}{T} P \right)^{1/2} \end{aligned} \quad (2.56)$$

From Eq. 2.52, we find the light power at the output port due to a GW signal:

$$\Delta P_{out} = P_{in} \left| 16J_0(\beta)J_1(\beta) \sin\left(\frac{\Omega}{c}\delta l\right) \mathcal{F} \frac{L}{\lambda} \left(1 - \frac{\mathcal{F}}{\pi}\epsilon\right) h \right| \quad (2.57)$$

Then, the signal-to-noise ratio related to shot noise is given by:

$$\frac{S}{N} = \frac{\Delta P_{out}}{\Delta P_{shot}} = \left(\frac{TP_{in}}{\hbar\omega} \right)^{1/2} \frac{16L}{\lambda} \sin\left(\frac{\Omega}{c}\delta l\right) \mathcal{F} \frac{L}{\lambda} \left(1 - \frac{\mathcal{F}}{\pi}\epsilon\right) h \quad (2.58)$$

We see that the higher the input power, the larger the SNR, and we can reduce the impact of shot noise by increasing P_{in} .

The respective conjugate comes from the uncertainty principle. The two main quantities here are the amplitude and the phase of the electromagnetic field, which cannot be simultaneously determined with arbitrary precision.

Let us consider a laser beam with power P that hits perpendicularly the mirror. At reflection, the momentum transferred to the mirror by each photon is $2|\vec{p}|$. Considering that the photon energy is $E_\gamma = |\vec{p}|/c$, the radiation pressure force is given by $F = 2P/c$. Taking ΔP from 2.56, we find the fluctuation in the radiation pressure force:

$$\Delta F = 2\sqrt{\frac{\hbar\omega_L P}{c^2 T}} \quad (2.59)$$

Shot noise has a white PSD (independent from the frequency), therefore we find the following expression for the PSD of the radiation pressure force:

$$\begin{aligned} S_F(\omega) &\simeq \frac{(\Delta F)^2}{\Delta f} = \frac{(\Delta F)^2}{1/T} = (\Delta F)^2 T \\ &= \frac{4\hbar\omega_L P}{c^2} \end{aligned} \quad (2.60)$$

this means that the amount of force noise at each frequency is $\propto P_{in}$. On the other hand, for mechanical oscillators like the suspension systems that hold the mirrors, the fluctuation in position are related to the force fluctuations by

$$\Delta x(\omega) = \frac{\Delta F(\omega)}{\omega^2} \quad (2.61)$$

This produces a $1/f^4$ noise which becomes all the more relevant at high laser power. Overall, when we try to minimize the impact of one type of quantum noise, we inevitably increase the impact of its conjugate. The goal is to minimize the total quantum noise as a function of frequency, and in order to do so we must consider the two terms.

The plot in Fig. 2.6 is a schematic representation of the situation (which also includes the interferometer response in the case of the flat PSD of the shot noise), and we find a minimum by changing P_{in} , so that the shot noise and radiation pressure contributions are balanced. All the points for which, for different values of P_{in} , the total strain due to quantum noise is minimized, is defined as the Standard Quantum Limit.

We can overcome the Standard Quantum Limit by introducing the concept of quantum squeezing and the injection of optical squeezed states of light inside the interferometer. Light can be described by the two quadratures of an electric field, both of which have an associated quantum operator:

$$\begin{aligned}\hat{X}_1 &= \frac{1}{2}(\hat{a} + \hat{a}^\dagger) \\ \hat{X}_2 &= \frac{i}{2}(\hat{a} - \hat{a}^\dagger)\end{aligned}\tag{2.62}$$

where \hat{a} and \hat{a}^\dagger are the creation and annihilation operators. Observation of either of these operators comes with a distribution or uncertainty, imposed by the quantization of light. When we deal with vacuum and coherent states, the uncertainties in the observable quadratures of amplitude and phase are symmetric and equal: $\Delta\hat{X}_A^2 = \Delta\hat{X}_\phi^2 = N$. In this case, N represents the scale of the SQL.

In squeezed states, the uncertainty in the two quadratures is no longer symmetric. Instead, quantum correlations reduce the uncertainty in one quadrature below the vacuum level, at the expense of increasing it in the conjugate one, in accordance with the Heisenberg uncertainty principle. A squeezed state can thus be defined as a state for which the variance of one quadrature is smaller than that of the vacuum state. The price to pay is an increase in the uncertainty of the orthogonal quadrature.

By injecting light that is squeezed in the appropriate quadrature into the interferometer, we can selectively reduce the quantum noise contribution that dominates in the measurement. In particular, amplitude squeezing reduces shot noise, while phase squeezing can mitigate radiation pressure noise, depending on the frequency region of interest. Therefore, by tuning the orientation of the squeezing ellipse in phase space, it is possible to surpass the Standard Quantum Limit and improve the interferometer sensitivity beyond what would be achievable with unsqueezed coherent light. [13]

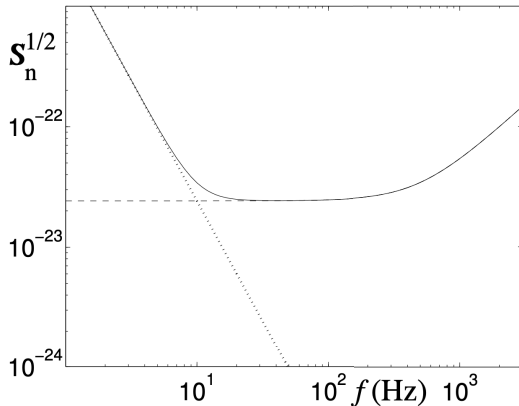


Figure 2.6: Total power spectral density given by quantum noise as a function of the frequency.

2.4.2 Other noise sources

Thermal noise is due to the thermal kinetic energy of the atoms of the detector. This induces vibrations of the whole structure, and the bouncing of light between the mirrors can amplify it. It can also happen that the mirrors absorb a small amount of the laser power, and this causes an increase of their temperature and, consequently, a change in the refraction index.

Brownian motion, that characterizes thermal noise, has been modeled by Einstein and Langevin in two different ways. The latter found an expression for the power spectral density, using Wiener-Kintchine theorem and assuming that the process n is white noise (independent of frequency):

$$S_n(\omega) = 4k_B T \gamma \quad (2.63)$$

here k_B is Boltzmann constant, T is the temperature of the system and γ is a friction coefficient, that accounts for dissipation in the system.

Another noise source is ground vibrations, which includes all the external mechanical vibrations that can come from seismic activity or any other kind of ground vibration. In order to minimize these effects, the test masses are kept suspended through systems based on pendulums. Since the ground noise frequency is higher with respect to the natural one of the suspension mechanism, this makes a good filter for this kind of noise.

Chapter 3

Stray light noise

In Sect. 2.4 we described the main noise sources affecting GW interferometers. Other "technical" noise sources can be defined, and one of these comes from stray light. In this chapter, Sect. 3.1 defines stray light and explains how it can be harmful to GW interferometers. Sect. 3.2 gives an overview of basic radiometry concepts and describes how surface roughness and dust particles scatter light, as the aim of this thesis is to remove harmful dust particles in a contactless way.

3.1 Stray light as a noise source

The laser beams of gravitational waves interferometers should follow a well-defined path and have very specific spatial properties. However, there are unavoidable phenomena that scatter light out of the intended path: if this scattered light is allowed to recombine with the main beam, it can originate a noise, called stray light noise, due to the motion of the surfaces that reflect the stray rays back into the main beam. The sources of this phenomenon are surface roughness of the optics, residual gas (which is the reason why the optics are in-vacuum), unstopped ghost beams and dust contamination. Scattered light can be harmful if it later recouples with the main interferometer beam with a different phase that is not constant over time, and can cause noise that can either mimic a gravitational wave signal or spoil control signals needed to keep the working point of the detector.

Stray light can cause transient noise signals, called glitches, which can affect the sensitivity at low frequencies, where mechanical and seismic noise are dominant. During the third LIGO-Virgo-Kagra observing run (O3), $\sim 20\%$ of GW signals overlapped with scattered light glitches, degrading the estimation of the source parameters [14]. Stray light noise depends in a non-linear way on the seismic noise: this means that the frequencies at which these noises manifest can be different. This happens because stray light noise depends on the phase given by the surface that reflects back the stray light toward the interferometer. This phase is limited in $[0, 2\pi]$, while the displacement due to seismic noise can be much greater, leading to a non-linear phenomenon called phase wrapping. Light scattering glitches have unusual features, like characteristic arches that repeat over time (an example is shown in Fig. 3.1), and such transients can last several minutes, with a typical frequency range of 20-60 Hz [15]. Their subtraction is essential, as the low frequency band is critical to Early Warning (EW) pipelines in the current observational campaign (O4). These are data analysis frameworks that monitor the output of the GW detectors in near-real time to identify the initial inspiral phase of compact binary coalescences. Another advantage of reducing the noise impact at lower frequencies is that it would allow us to observe signals from merging binaries with higher masses.

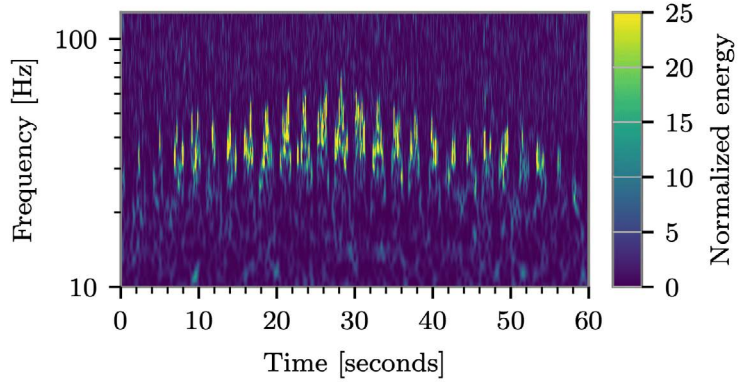


Figure 3.1: Time-frequency representation of fast scattering glitches. Figure from [16].

3.2 Characterization of light scattering

Let us first introduce a series of useful concepts to characterize stray light contribution. We consider a surface that is exposed to radiation coming from a certain direction, and part of this radiation is re-emitted or scattered by the surface into other directions, as shown in Fig. 3.2. The radiant flux is energy per unit time emitted by the surface, $\Phi = \epsilon/t$, where ϵ is energy and t is the unit of time. Radiance is the differential radiant flux emitted by a surface per unit solid angle and area, and it quantifies the amount of brightness of a surface:

$$L(\theta_s) = \frac{d^2\Phi}{dA \cos(\theta_s)d\Omega} \quad (3.1)$$

where $d\Phi$ is the differential flux emitted by the differential projected area of the source, $dA \cos(\theta)$, into the differential solid angle $d\Omega$. θ_s is the angle between the normal direction to the surface and the source-observer direction. Irradiance is the radiant flux received by the surface per unit area:

$$E = \frac{d\Phi}{dA} \quad (3.2)$$

With these definitions, the Bidirectional Scattering Distribution Function (BSDF) can be introduced, a function that quantifies the amount of light scattered by a surface. The BSDF is defined as the radiance of the scattering surface over the incident irradiance of the surface, and it allows a complete description of the scattering properties. Two different contributions can be recognized in it: the Bidirectional Transmission Distribution Function (BTDF) and the Bidirectional Reflectance Distribution Function (BRDF). The BTDF is the light that is transmitted by the scatterer ($\pi/2 \leq \theta_s \leq \pi$), while the BRDF is the light that is reflected by the scatterer ($0 \leq \theta_s \leq \pi/2$). Depending on the optical characteristics of the system, one contribution can be neglected, for example, in the case of an opaque surface, only the BRDF can be considered. The BSDF is:

$$\text{BSDF}(\theta_i, \phi_i, \theta_s, \phi_s) = \frac{dL(\theta_i, \phi_i, \theta_s, \phi_s)}{dE(\theta_i, \phi_i, \theta_s, \phi_s)} \quad (3.3)$$

where θ_i, θ_s and ϕ_i, ϕ_s are the elevation and azimuth angles of the incident and scattered ray respectively (see Fig. 3.2).

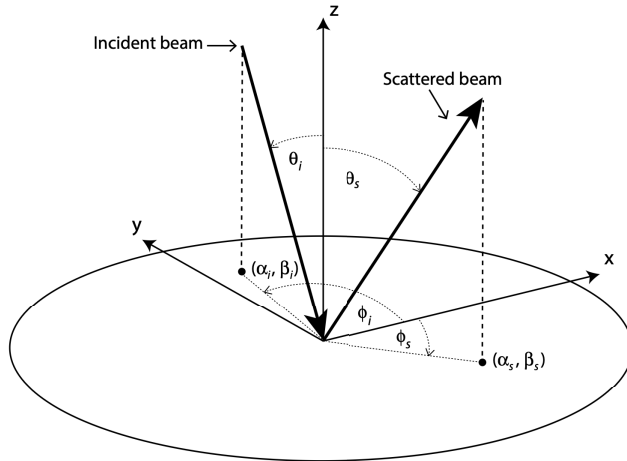


Figure 3.2: Angles used in the definition of the BSDF (Eq. 3.3). Figure from [17].

We can now introduce the Total Integrated Scattering (TIS), which is defined as the integral of the BSDF over a given domain in the solid angle. If we choose the half-sphere that covers the reflected or transmitted part of the scattering, we have:

$$\text{TIS}(\theta_i, \phi_i) = \int_0^{2\pi} \int_0^{\pi/2} \text{BSDF}(\theta_i, \phi_i, \theta_s, \phi_s) \cos \theta_s \sin \theta_s d\theta_s d\phi_s \quad (3.4)$$

Physically, the TIS is the fraction of the scattered power P_s over the incident power P_{in} in the given hemisphere:

$$\text{TIS} = \frac{P_s}{P_{in}} \quad (3.5)$$

From this definition, the conservation of energy implies $\text{TIS} \in [0, 1]$.

3.2.1 Light scattering by surface roughness

A rough surface scatters light depending on its statistical surface characteristics. We define as optical figure the shape of the surface at macroscopic scales. The so called surface roughness profile comprehends all the spatial deviations from the nominal surface height that influence the intensity and angular distribution of scattered light. These deviations are described by a function $z(x, y)$, where x and y are coordinates on the nominal surface. Fig. 3.3 shows a representation of the contributions to scattering by surface roughness. A quantity that can be computed from the profile $z(x, y)$ is the power spectral density (PSD):

$$S_2(f_x, f_y) = \lim_{L \rightarrow \infty} \frac{1}{L^2} \left| \int_{-L/2}^{L/2} \int_{-L/2}^{+L/2} z(x, y) \exp[-2\pi i(f_x x + f_y y)] dx dy \right|^2 \quad (3.6)$$

where f_x and f_y are the spatial frequencies and L is the length of the measured profile.

Another important quantity is the RMS roughness σ of the surface:

$$\sigma = \left\{ \lim_{L \rightarrow \infty} \frac{1}{L^2} \int_{-L/2}^{L/2} \int_{-L/2}^{L/2} [z(x, y)]^2 dx dy \right\}^{1/2} \quad (3.7)$$

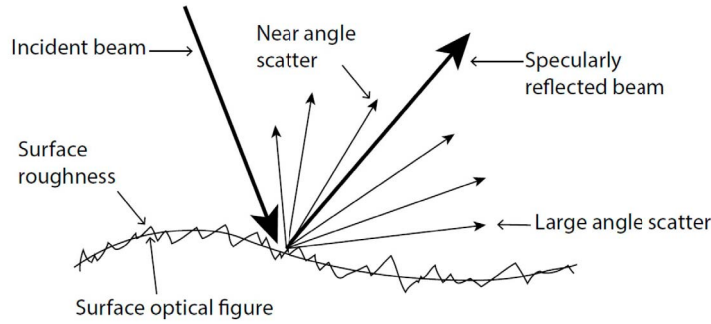


Figure 3.3: Scattering by a surface, with the distinction between the surface optical figure and the surface roughness. Figure from [17].

Generally, the PSD of most optical surfaces (for which the RMS roughness σ is much less than the wavelength of light λ) is well approximated by the *K-correlation model*, which has the following functional form:

$$S(f) = A[1 + (Bf)^2]^{-C/2} \quad (3.8)$$

where $f = (f_x^2 + f_y^2)^{1/2}$, A is the magnitude of the PSD at low frequencies, $1/B$ is the spatial frequency at which the "roll-off" in the PSD plot occurs (see Fig. 3.4) and C is the slope of the PSD at frequencies above $1/B$.

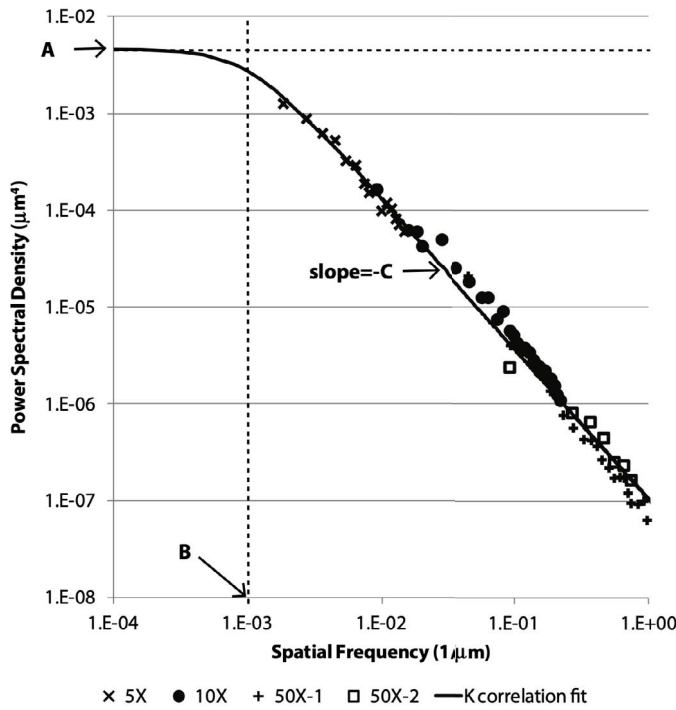


Figure 3.4: Measured PSD versus f for a typical mirror surface with $\sigma = 1.3$ nm. The different markers correspond to different magnifications used. Figure from [17].

The PSD is connected to the BSDF through the Rayleigh-Rice perturbation theory, for $\sigma \ll \lambda$ (which is verified for GW interferometers, that have $\lambda = 1064$ nm):

$$\text{BSDF}(\theta_i, \theta_s, \phi_s) = \frac{4\pi^2 \Delta n^2}{\lambda^4} \cos \theta_i \cos \theta_s Q S_2(f_x, f_y) \quad (3.9)$$

where the angles $\theta_i, \theta_s, \phi_s$ are the same defined in Fig. 3.2, Δn is the difference in refractive index across the boundary of the scattering surface, Q is the so called polarization factor, which is a function of the dielectric constant of the substrate, $\theta_i, \theta_s, \phi_s$ and the polarization states of the incident and scattered beams. S_2 is the PSD as defined in Eq. 2.53, and f_x, f_y can be written as:

$$f_x = \frac{\sin \theta_s \cos \phi_s - \sin \theta_i}{\lambda} \quad (3.10)$$

$$f_y = \frac{\sin \theta_s \sin \phi_s}{\lambda} \quad (3.11)$$

then Eq. 3.9 becomes:

$$\text{BSDF}(|\sin \theta_s - \sin \theta_i|) = \frac{4\pi^2 \Delta n^2}{\lambda^4} \cos \theta_s \cos \theta_i Q \left\{ A \left[1 + \left(\frac{B |\sin \theta_s - \sin \theta_i|}{\lambda} \right)^2 \right] \right\}^{-C/2} \quad (3.12)$$

this form of the equation is often parametrized as the 3-parameter Harvey model (*Harvey-Schack model*):

$$\text{BSDF}(|\sin \theta_s - \sin \theta_i|) = b_0 \left[1 + \left(\frac{|\sin \theta_s - \sin \theta_i|}{l} \right)^2 \right]^{s/2} \quad (3.13)$$

where:

$$\begin{aligned} b_0 &= \frac{4\pi^2 \Delta n^2 Q A}{\lambda^4} \\ l &= \frac{\lambda}{B} \\ s &= -C \end{aligned}$$

In this form, the parameters directly reflect the spectral structure of a lightly rough optical surface. A PSD that shows a low-frequency plateau followed by a roll-off at higher frequencies (shown in Fig. 3.4) produces a BSDF with the same qualitative behavior. The parameter b_0 sets the overall scattering level, reflecting the PSD amplitude in the plateau region. The scale parameter l defines the location of the “knee,” corresponding to the spatial frequency at which the PSD transitions from the flat region to the power-law descent. Finally, the exponent s represents the slope of the fall-off at high frequencies, determining how rapidly the scattered intensity decreases with angle.

3.2.2 Light scattering by dust particulates

In order to reduce scattered light by surface roughness, in GW interferometers like Virgo the optics have an extremely low roughness (hence low scattering): at this level of roughness, any dust that may deposit can become an additional and non negligible source of light scattering. For the wavelength of the Virgo laser (1064 nm), the particles that cause the larger concern for light scattering are the ones with a diameter between 0.1 μm and a few

$100 \mu\text{m}$ ¹, hence this is the dimension considered in this thesis for the study of the DLC technique.

Mie theory

The theory that describes scattering by small particulates is Mie Theory, developed by Gustav Mie in 1908 [18]. It is an analytical solution of Maxwell's equations with appropriate boundary conditions, and it describes the scattering of an incident plane wave by a spherical, isotropic and non-magnetic particle in a non-absorbing medium. Mie theory defines the scattering matrix, that allows us to compute the scattered field at a distant point from a particle irradiated by a polarized, monochromatic plane wave:

$$\begin{pmatrix} E_{s,\parallel} \\ E_{s,\perp} \end{pmatrix} = -\frac{1}{ikr} e^{ik(r-z')} \begin{pmatrix} S_2 & S_3 \\ S_4 & S_1 \end{pmatrix} \begin{pmatrix} E_{i,\parallel} \\ E_{i,\perp} \end{pmatrix} \quad (3.14)$$

here the propagation direction is defined by the \hat{z} axis, \vec{k} is the wavevector of the beam and r is the distance between the center of the particle and the point at which we want to compute the field. The subscripts s and i indicate the scattered and the incident fields respectively, while \parallel and \perp are used to indicate the polarizations perpendicular and parallel to the scattering plane (defined as the plane containing the incident and scattered directions) respectively. $S_{1,2,3,4}$ are the amplitude scattering functions, that depend on physical properties of the particle and on the scattering angle. For an isotropic sphere, the terms S_3 and S_4 are null. The terms S_1 and S_2 are connected with the P-polarized and S-polarized scattered light through the following formulas:

$$I_s^P = \frac{1}{k^2 r^2} |S_2|^2 I_0 \quad (3.15)$$

$$I_s^S = \frac{1}{k^2 r^2} |S_1|^2 I_0 \quad (3.16)$$

where I_0 is the incident irradiance and I_s^P , I_s^S are the scattered P-polarized and S-polarized irradiances respectively.

The angular distribution of the scattered light depends on the size parameter (also called reduced diameter), defined as follows:

$$x = \frac{\pi D}{\lambda} \quad (3.17)$$

where D is the particle diameter and λ is the laser wavelength. Particles with $x \lesssim 0.1$ exhibit a Rayleigh scattering pattern (which, indeed, is a limit case of Mie theory for particles smaller than the wavelength), which is isotropic for S-polarized incident light and symmetric in the forward and backward direction for P-polarized incident light. The general Mie scattering case should be applied for $0.1 \lesssim x \lesssim 10$. On the other side of the spectrum, for particles larger than the wavelength, Mie theory leads to classical optics. Fig. 3.5 shows the angular distribution of the scattered intensity for different size parameters.

Scattering from a distribution of particles on a surface

The total BRDF can be computed for a distribution of spherical and isotropic particles deposited on a surface and a laser beam incident on it under two main assumptions: first,

¹Although particles of around $100 \mu\text{m}$ are still critical for stray light induced noise, they are less likely to be found in a clean room environment.

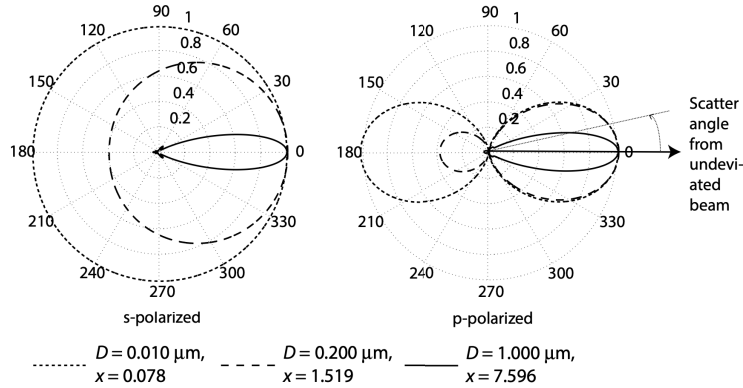


Figure 3.5: Angular distribution of the normalized intensity I for an s-polarized (left) and p-polarized (right) incident laser beam. The different line styles correspond to different particle diameters and size parameters. Figure from [17].

particles scatter according to Mie theory, and do so independently; secondly, the radiation that is scattered in the forward direction reflects from the surface and does not interact again with the particle. Fig. 3.6 shows how light can be scattered at an angle θ_s by a particle on a reflecting surface, where scattering from the surface is neglected.

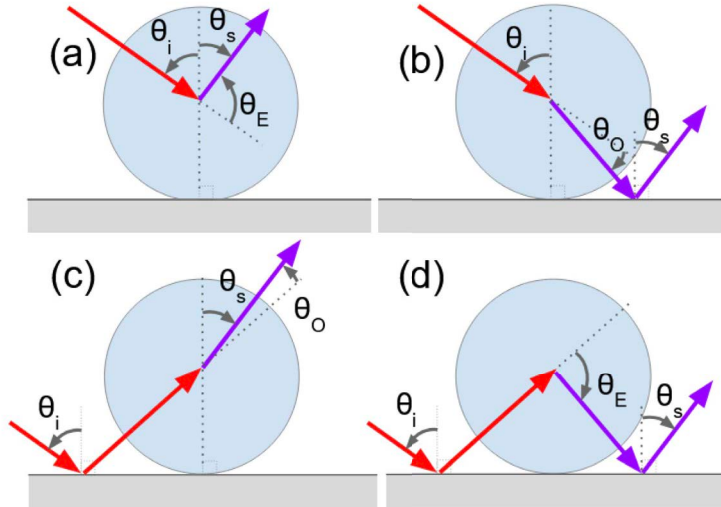


Figure 3.6: Geometrical scheme of the 4 different scattering processes by a dust particle on a surface. The red arrow represents the incident light, with an angle θ_i with respect to the normal of the surface; scattered light, at an angle θ_s , is represented as a purple arrow. (a): direct scattering by the particle, (b): scattering by the particle toward the surface and then reflection, (c): reflection by the surface to the particle, then scattering by the particle, (d): reflection by the surface to the particle, scattering by the particle to the surface, then reflection by the surface. Figure from [19].

Let $f(x)$ be the number of particles with reduced diameter x per unit area, all with the same refractive index m , and let $R_{S,P}(\theta_s,i)$ be the power reflectivity of the surface for S- or P- polarized light and at the θ_s or θ_i angle of light on the surface. Before expressing the

BRDF for polarized light, we have to consider two phase differences given by the reflections in the system. Firstly, each time light is reflected by a surface it gains a π phase. Secondly, in the cases where reflection is present ((b), (c) and (d) in Fig. 3.6) a contribution comes from the optical phase difference of the rays being reflected with respect to the rays that only interact with the particle. We can then write the BRDF due to dust for S and P polarizations [19]:

$$\text{BRDF}^{SS}(\lambda, m, \theta_s, \theta_i) = \frac{1}{k^2 \cos \theta_s} \int f(x) \left\{ [R_S(\theta_s) + R_S(\theta_i)]|S_1(x, m, \theta_O)|^2 + [1 + R_S(\theta_s)R_S(\theta_i)]|S_1(x, m, \theta_E)|^2 \right\} dx \quad (3.18)$$

$$\text{BRDF}^{PP}(\lambda, m, \theta_s, \theta_i) = \frac{1}{k^2 \cos \theta_s} \int f(x) \left\{ [R_P(\theta_s) + R_P(\theta_i)]|S_2(x, m, \theta_O)|^2 + [1 + R_P(\theta_s)R_P(\theta_i)]|S_2(x, m, \theta_E)|^2 \right\} dx \quad (3.19)$$

where the superscripts PP and SS indicate the polarization of the incident and scattered light. The angles $\theta_{E,O}$ represent the direction of the scattered light by the particle with respect to the incident light, in the case of even ($k = E$, cases (a) and (d) in Fig. 3.6) or odd ($k = O$, cases (b) and (c) in Fig. 3.6) number of reflections by the surface. Geometrically, it can be seen that $\theta_E = \pi - \theta_s - \theta_i$ and $\theta_O = \theta_s - \theta_i$. For unpolarized incident and scattered light (UU), the BRDF can be found by averaging the expressions in Eq. 3.19 and 3.18:

$$\text{BRDF}^{UU} = \frac{\text{BRDF}^{PP} + \text{BRDF}^{SS}}{2} \quad (3.20)$$

The scattering due to surface roughness only depends on the characteristics of the material, as seen in Sect. 3.2.1, while scattering by dust particles also depends on the size and number of the particles deposited. This means that, in cases like the Virgo optics, where the surface roughness is extremely low, dust particles give the main contribution to stray light noise, if they are large enough in size and numerosity. This is evident in the plots shown in Fig. 3.7, where a contaminated wafer gives a dominant contribution to scattered light with respect to a clean one.

Particle density function models

We can model the particle density function $f(D)$, which represents the number of particles with a diameter D per unit area, in a clean environment through the Institute of Environmental Sciences and Technology (IEST) CC1246D standard. This method quantifies the number of particles on a surface using a number, called the cleanliness level (CL). The particle density function can be written as follows:

$$f(S, \text{CL}, D) = -\frac{d}{dD} N_p(S, \text{CL}, D) \quad (3.21)$$

where N_p is the number of particles on a surface of 0.1 m^2 whose diameters are greater than or equal to D , a plot of which is shown in Fig. 3.8:

$$N_p(S, \text{CL}, D) = 10^{|S|[\log_{10}^2(\text{CL}) - \log_{10}^2(D)]} \quad (3.22)$$

here S is the particle distribution slope, CL is the cleanliness level and D is the particle diameter in μm . S is a function of the environment in which the particle contamination

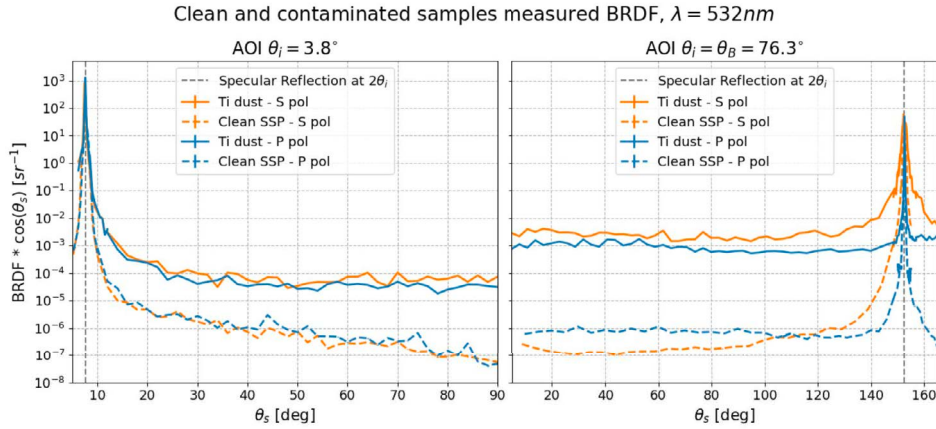


Figure 3.7: BRDF (multiplied by $\cos \theta_s$) measurements of a clean Si wafer (dashed lines) and a similar one contaminated with Ti dust particles (solid lines), both for S- and P-polarizations (orange and blue respectively). Left and right correspond to two different θ_i : 3.8° and 76.3° respectively. The latter corresponds to the Brewster angle. A wavelength of $\lambda = 532$ nm is used, and θ_s is the scatterometer's arm angular position. Figure from [20].

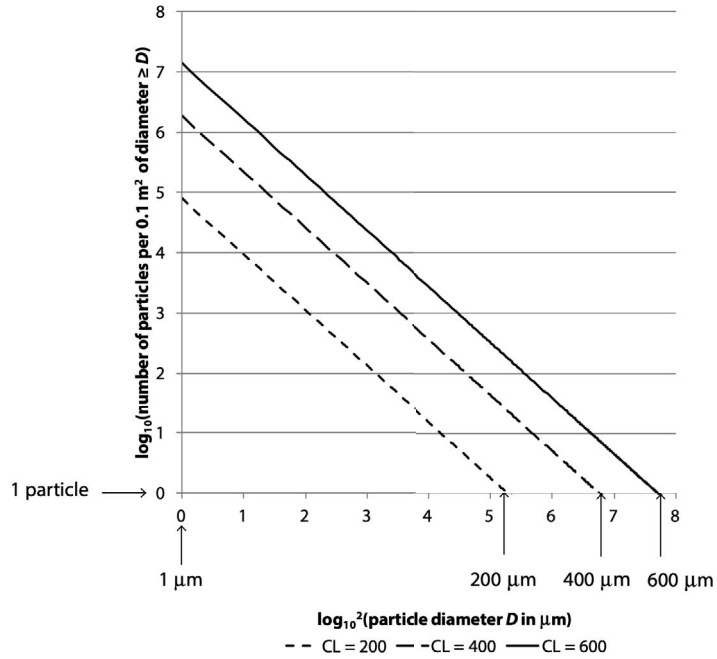


Figure 3.8: Number of particles with a diameter $\geq D$ per 0.1 m^2 versus D according to IEST-STD-CC1246D. Typical values of CL (for uncontaminated or visibly clean surfaces) and the standard slope value (-0.926) are assumed. Figure from [17].

occurred; the cleaner the environment, the lower the value of S . The IEST-STD-CC1246D defines a value of S equal to -0.926, which is representative of particle distributions on freshly cleaned surfaces. Other studies found a good description of particle distributions for clean room environments for $S = -0.383$. CL represents the particle diameter (in μm)

such that there is only 1 particle with a diameter bigger than CL per 0.1 m^2 . For example, a value of $\text{CL}=200$ (the long dashed line in Fig. 3.8) means that there is only 1 particle per 0.1 m^2 with a diameter $\geq 200\text{ }\mu\text{m}$. In general, uncontaminated surfaces have $\text{CL}<200$, visibly clean surfaces show $\text{CL}=600$ and for visibly dirty surfaces $\text{CL}>1000$.

Chapter 4

Laser cleaning technology

As we have seen in the previous chapters, stray light caused by dust particles (with a diameter between 0.1 and 50 μm approximately) deposited on the test masses can be a very limiting noise source. The purpose of this work is to test a new cleaning technique suitable for suspended optics, that could also be applied in vacuum. Dry Laser Cleaning (DLC), which is better characterized in this chapter, represents a promising tool, since it allows contactless cleaning. Laser cleaning technology uses the interaction between a laser and the materials of interest. Compared to other conventional physical cleaning technologies, it has many advantages [21]:

1. It can adopt "dry" cleaning, without the need of a cleaning medium
2. It can achieve localized cleaning using the characteristics of lasers
3. By controlling laser parameters (like intensity, wavelength, pulse width) it can achieve effective cleaning without damaging the substrate
4. It can remove very small pollutant particles, reaching even the sub-micron level
5. It can be applied to a wide range of materials both for the substrate and the contaminants

This technology can be applied to remove from a substrate a contaminant layer made of a different material and/or deposited unwanted particles. The latter is the case of interest for this thesis, since the presence of micron-level dust particles is unavoidable in air-based optics and cannot be excluded in vacuum environments, such as those of Virgo test masses.

In this chapter, Sect. 4.1 describes models for the adhesion force between a particle and a substrate to which it is in contact with. Sect. 4.2 gives an overview of the physics of laser-matter interaction, and on Sect. 4.3 the physical processes during a laser cleaning test are listed. This is followed by a description of the different laser cleaning regimes and their dependence on laser parameters in Sect. 4.4, and finally Sect. 4.5 shows a numerical simulation for a simplified model of a single Mo particle on a glass substrate.

4.1 Adhesion force

There exist several adhesion forces that make contaminants adhere to a surface. The three main ones are: Van der Waals force, capillary force and electrostatic force. For particles smaller than a few micrometers close to a substrate, the dominant adhesion is given by Van der Waals. This force is the main focus of this section.

Van der Waals force originates from the interaction between the dipole moment of one material and the induced dipole moment of the other one. To model contact between bodies, the pairwise interaction between two molecules must first be generalized to describe the interaction between a molecule and a flat surface, then between two spherical particles, and finally between a spherical particle and a flat surface. The purely attractive part of the potential w between two atoms or molecules is in the following form: $w(r) = -C/r^N$, where r is the distance between the two bodies that interact, C is a characteristic interaction constant, which depends on the nature of the atoms/molecules, and N describes how the interaction decreases with distance. Then, the interaction energy of a molecule and a surface of infinite thickness made up of many molecules will be the sum of its interaction with all the molecules in the body. We can calculate this by integrating the interaction of the molecule with each volume element over the volume of the surface. If the surface has a number density n and its distance from the molecule is D , this is expressed as follows:

$$w(D) = \int \left(-\frac{C}{r^N} \right) n dV \quad (4.1)$$

Moving to cylindrical coordinates (r, θ, z) , with the situation shown in Fig. 4.1, we can rewrite the integral:

$$w(D) = -2\pi n C \int_{z=D}^{+\infty} dz \int_{x=0}^{+\infty} \frac{x dx}{(x^2 + z^2)^{N/2}} \quad (4.2)$$

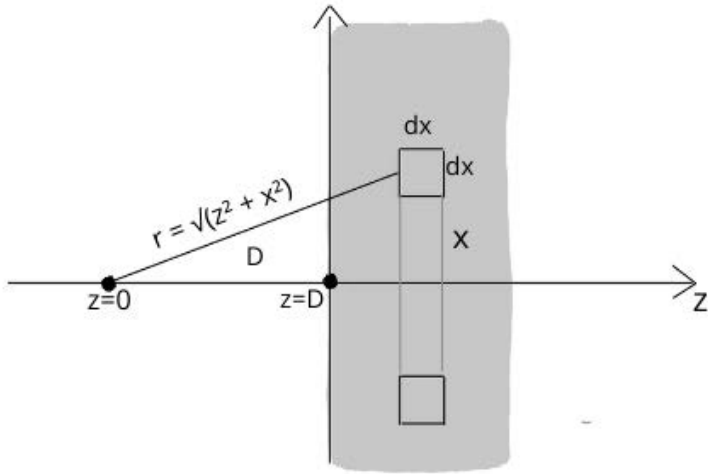


Figure 4.1: Method used for integrating the interaction energies between a molecule and all the molecules in a flat surface. The molecule is placed at $z = 0$ and is at a distance D from the flat surface. Figure adapted from [22].

For nonpolar atoms or molecules, the dominant long-range attraction is due to dispersion (London) forces, which arise from correlated fluctuations of the electron clouds. For these forces $N = 6$, and by integrating Eq. 4.2 we obtain the following result:

$$w(D) = -\frac{\pi Cn}{6} D^{-3} \quad (4.3)$$

In a similar way, we can find the expression for the case of a sphere approaching a plane. From geometric considerations, with the variables defined in Fig. 4.2, we can find that $x^2 = z(2R - z)$ (where R is the radius of the sphere). Then, the volume of a thin circular section of area πx^2 and thickness dz in the particle is $\pi x^2 dz = \pi(2R - z)z dz$, and the number of molecules inside this section is $\pi \rho(2R - z)z dz$, where ρ is the number density of molecules in the sphere. All the molecules are at a distance $D + z$ from the surface, then the net interaction energy is:

$$w(D) = -\frac{2\pi^2 Cn^2}{(N-2)(N-3)} \int_{z=0}^{z=2R} \frac{(2R-z)z}{(D+z)^{N-3}} dz \quad (4.4)$$

With the approximation $D \ll R$, only small values of z contribute to the integral, thus we can extend the integration upper limit to $+\infty$ and neglect z with respect to $2R$. We recall the definition of the Hamaker constant: $A_H = \pi^2 C n_1 n_2$, where n_1 and n_2 are the number densities of the sphere and the surface, and find the Van der Waals interaction between a sphere at a distance D from a plane, again for $N = 6$ [22]:

$$w(D) = -\frac{A_H R}{6D} \quad (4.5)$$

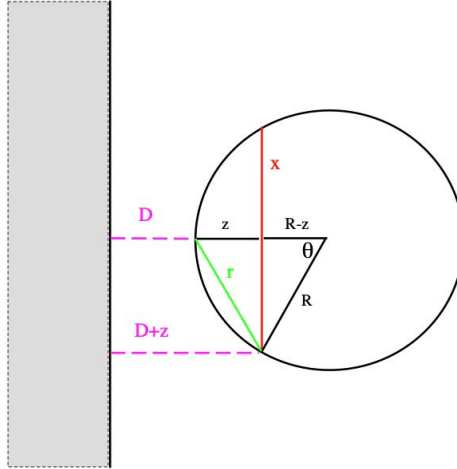


Figure 4.2: Method used for integrating the interaction energies between molecules to obtain the interaction energy between a sphere of radius R and a flat surface. Figure from [22].

This formula works if we have a sphere close to a plane (but still so that $D \gtrsim 0.5$ nm), but it is less suitable if the two are in contact, because it does not take into consideration the repulsive part of the Van der Waals interaction, which is not negligible for distances $\lesssim 0.3 - 0.4$ nm, and for $D \rightarrow 0$ it leads to a force $F_{adh} \rightarrow +\infty$. In addition, it does not include elastic deformation due to contact. Since we are interested in modeling particles deposited on a surface, hence in contact with it, we have to introduce models that can describe the contact case.

For spherical particles attached to a surface, the main models are based on the theoretical work of Johnson, Kendall and Roberts (JKR) and Derjaguin, Muller and Toporov (DMT) [23]. These models assume that the two bodies are elastic and in mechanical contact: in this regime, a finite interfacial gap is no longer defined, and the effective spacing between the two surfaces reduces to the atomic-scale separation at the interface. These two models give the following adhesion force estimations for a spherical particle on a substrate:

$$F_{adh}^{\text{DMT}} = 2\pi RW_{ij} \quad (4.6)$$

$$F_{adh}^{\text{JKR}} = \frac{3}{2}\pi RW_{ij} \quad (4.7)$$

where R is the particle radius and W_{ij} is the work per unit surface of adhesion between the two materials i and j (the particle and the substrate). Its general form is:

$$W_{ij} = \gamma_i + \gamma_j + \gamma_{ij} \quad (4.8)$$

where γ_i is the surface energy of the first material (for example, the particle), γ_j is the surface energy of the second material (the substrate) and γ_{ij} is the interface energy (usually, if the medium is air or vacuum, $\gamma_{ij} \simeq 0$) [24]. The surface energy is the energy required to create a new unit of area, thermodynamically it is the variation of the free energy per unit of surface due to the detachment of the particle from the surface.

The choice of the model depends on the specific cases: the JKR model generally applies for particles with larger radius (1-10 μm), strong adhesion and low elastic modulus, while the DMT model applies for particles with smaller radius (1-10 nm), weak adhesion and high elastic modulus. To distinguish between the two extreme cases, we define the Tabor parameter as follows:

$$\mu = \left(\frac{RW_{ij}^2}{E^{*2}z_0^3} \right)^{\frac{1}{3}} \quad (4.9)$$

where z_0 is the distance at which the adhesive interaction operates (0.2 - 0.4 nm) and E^* is the effective Young modulus, which has the following form:

$$\frac{1}{E^*} = \frac{1 - \nu_1^2}{E_1} + \frac{1 - \nu_2^2}{E_2} \quad (4.10)$$

and E_1 , E_2 and ν_1 , ν_2 are the Young modulus and Poisson ratio of the two materials (the particle and the substrate). Physically, the Tabor parameter compares the characteristic elastic deformation of the contact (which can be quantified by the elastic length $l_e = [(RW_{ij}^2)/E^{*2}]^{1/3}$) to the range of the interaction potential z_0 . This parameter indicates whether elastic effects or short-range adhesion dominate the contact behavior. Experimentally, one can define the following regimes: JKR model for $\mu \gtrsim 5$, DMT model for $\mu \lesssim 0.1$ and intermediate regime for $0.1 \lesssim \mu \lesssim 5$. Modeling the intermediate regime requires more sophisticated analyses. Since a precise estimation of adhesion forces was not required for the purposes of this study, only the two 'extreme' JKR and DMT cases were considered for the numerical simulations (see Sect. 4.5)[23].

Let us now briefly define the other two adhesion forces that are not the focus of this study, capillary and electrostatic force. If there is a liquid film on the surface, capillary forces cannot be ignored. This contribution is expressed in the following form:

$$F_c = 4\pi\gamma R \quad (4.11)$$

where γ is the surface energy per unit area of the liquid film (surface tension) and R is the particle radius. In certain conditions, an adsorbed water layer is sufficient to generate a stable meniscus, making capillary forces significant at moderate relative humidity.

Lastly, there is the electrostatic force, which can be expressed as follows:

$$F_e = \frac{\pi \varepsilon U^2 R}{z} \quad (4.12)$$

where U is the contact potential difference between the particle and the substrate, ε is the dielectric constant of the air between the particle and the substrate and z is the distance between the particle and the surface. Electrostatic adhesion becomes relevant when significant charge separation occurs, triboelectric effects or external charging.

All three types of adhesion forces mentioned before are proportional to the particle radius R . The gravity of the particle is:

$$F_g = mg = \rho \frac{4}{3} \pi R^3 g \quad (4.13)$$

where m is the mass of the particle, g is gravitational acceleration, ρ is the mass density of the particle. F_g is proportional to the third power of R , meaning that for a particle with a radius $R \sim 0.5 \mu\text{m}$, van der Waals force is 10^7 times gravity.

4.2 Laser-matter interaction

Let us consider a laser beam impinging on a certain material. Assuming that the laser is collimated, the field amplitude can be approximated as a plane wave. Therefore, in a uniform, non-absorbing propagation medium, the electric field can be expressed as follows:

$$E(z, t) = E_0 \exp \left[i \left(\frac{2\pi n z}{\lambda} - \omega t \right) \right] \quad (4.14)$$

where E_0 is the amplitude, z is the coordinate of the propagation direction, ω is the angular frequency, λ is the wavelength and n is the refraction index of the propagation medium. When a laser shines on a material, the observed phenomena are absorption, reflection, transmission and scattering. The total energy is conserved, which means:

$$I = I_r + I_a + I_t + I_s \quad (4.15)$$

where I is the total incident laser intensity, I_r is the reflected intensity, I_a is the absorbed intensity, I_t is the transmitted intensity and I_s is the scattered intensity. In the following formulas, scattering is neglected.

If the laser is vertically incident on a material, the electric field in Eq. 4.14 propagates in a medium with a refractive index n_1 and hits a medium with refractive index n_2 . The reflectivity is:

$$\mathcal{R} = \frac{(n_1 - n_2)^2}{(n_1 + n_2)^2} \quad (4.16)$$

If the material thickness is much larger than the optical penetration (see below), transmittance is negligible, so we can write $A = 1 - \mathcal{R}$, where A is the absorptivity.

Absorption is a crucial phenomenon for laser cleaning technique, since how much the contaminant and the substrate absorb determines the removal mechanism. The absorption of the laser by a material increases with its thickness l . The laser intensity satisfies Lambert's law:

$$I(l) = (1 - \mathcal{R})I_0 e^{-\mu_\alpha l} \quad (4.17)$$

where \mathcal{R} is the reflectivity, I_0 is the incident laser intensity and μ_α is the absorption coefficient, which is related to the material properties.

We define as absorption depth l_α the distance that the laser light travels inside the material before the intensity drops to $1/e$ of the incident laser energy. From Eq. 4.17 one gets $l_\alpha = 1/\mu_\alpha$. Absorption strongly depends on the type of material that is processes, in particular whether it is metal or non-metal. [25]

In case an electromagnetic (EM) field is incident on a metal, photons are absorbed by the electrons located in the conduction band, while for semiconductors electrons can jump from the valence to the conduction band: this is a threshold process, since the photon energy $h\nu$ must be higher than the energy gap. In both cases, the photon absorption creates excited states, and the physical processes that follow can be divided into two main categories: thermal processes and photochemical processes. In the first ones, the energy is mainly turned into heat, while the second ones involve chemical reactions between excited species, the photoelectric effect, or direct bond breaking.

Lasers can be continuous or pulsed. Both types are used for laser cleaning tests, for the purpose of this thesis a pulsed laser was engaged, and the pulse duration is a crucial parameter in the determination of the physical mechanism during laser-matter interaction. Let us consider a pulsed laser that irradiates a homogeneous surface, and let us assume that the pulse duration of the laser is equal to a characteristic time τ_L . Let us focus on thermal processes in metals. The typical relaxation time τ_r is around 10^{-12} - 10^{-14} s, and for typical values of τ_L this means $\tau_r \ll \tau_L$. Under this condition, the system can be modeled by the 1D heat diffusion equation. On the contrary, in the case of ultra-short laser pulses, the condition $\tau_r \ll \tau_L$ is not necessarily verified and the dynamic of the excited species must be included. This leads to the so-called Two-Temperature-Model (TTM), applied to systems characterized by femto and pico second pulses. [26]

The pulse duration has a central role in the mechanism that leads to damage. For very short pulse durations (from femtoseconds to picoseconds), there can be nonlinear effects, like multiphoton ionization and avalanche ionization, that can cause substrate damage. Pulse duration on the order of picoseconds to nanoseconds can lead to damage caused by dielectric breakdown and thermal effects, while for pulses $\geq 10^{-9}$ s thermal effects are dominant.

4.3 Main physical laser cleaning processes

Let us consider a substrate and a particle deposited on it that we want to detach through the action of a pulsed laser. The laser-matter interaction described in Sect. 4.2 leads to a variety of physical mechanisms in the system composed of the substrate, the contaminant and the environment during a laser cleaning procedure. The dominance of each mechanism depends on the optical penetration depth and on how heat spreads during the pulse, but also on physical parameters, such as the laser cleaning medium, substrate materials, and contaminants. [27] Here is a general overview of all possible physical processes, before focusing on the main ones involved in dry laser cleaning.

- Thermal ablation mechanism: during irradiation, the temperature of the system increases. When the laser's energy is sufficiently high, the temperature of the materials can exceed the melting point, making them undergo combustion, decomposition, or vaporization. If this happens to the particle without affecting the substrate, we obtain a successful removal.
- Thermal stress mechanism: during the pulse durations, both the particle and the substrate undergo a thermal expansion that, as explained in Sect. 4.5.2, can result in a lifting force. When it exceeds the Van der Waals force, the particle is detached from the surface.
- Momentum transfer: photons can transfer momentum to the deposited particle. This leads to a radiation force on the particle that can overcome the adhesion force.
- Electrostatic force modulation: high-energy photons (4-6 eV) can cause photoemission of electrons from the particle or the substrate, or intense laser pulses can ionize air near the surface, creating a transient plasma. Multiphoton and avalanche ionization can also occur. Only if both the particle and the substrate ionize a repulsive force is achieved, and the particle detaches from the substrate.
- Photochemical bond breaking: the direct breaking of molecular or interfacial bonds by absorption of photons, without significant heating. It can break organic residues into fragments.

Dry laser cleaning can be obtained when the laser beam directly irradiates the surface. The pollutant particles absorb the laser energy and then leave the surface through mechanisms such as thermal diffusion, vaporization, vibration, etc. In some cases, the thermal expansion of the substrate can produce a lifting force that overcomes Van der Waals force [28].

4.4 Laser cleaning dependence on laser parameters

The results of a laser cleaning procedure depend mainly on the laser parameters, such as intensity, wavelength, pulse duration and repetition rate; these parameters should be chosen carefully to get a cleaning effect and avoid damaging the substrate [29]. Here a short overview of the effects of the different laser parameters is given, a more complete numerical estimation is discussed in Sect. 4.5.

Laser intensity

In laser cleaning, two fluence or intensity thresholds can be defined: the cleaning threshold and the damage threshold. The former is the minimum power (energy) per unit area that can cause the contaminants' detachment from the substrate, while the latter is the power (energy) per unit area that causes damage to the substrate. Increasing the laser intensity, or reducing the laser beam spot area, generally promotes the cleaning efficiency, if it is kept below the damage threshold.

The laser induced damage threshold (LIDT) is the highest quantity of laser radiation incident upon a material for which the extrapolated probability of damage is zero. The quantity of laser radiation can be expressed in energy density or power density. For an optical component, there is no damage if, after the laser processing, there are no observable changes within the optical properties (for example reflectance, transmittance or wavefront). [30]

Laser wavelength

The material's absorption coefficient and consequently the penetration depth of the laser are related to its wavelength. When the wavelength is short (UV), due to its high photon energy, the light absorption depth is smaller than the thermal diffusion length (the scale of the depth at which heat penetrates during the pulse, better defined in Sect. 4.5), and energy is deposited in a shallower region. In this situation, photochemical ablation is the main cleaning process. When the wavelength is longer (IR), the optical absorption length increases, and photothermal ablation plays a leading role in the cleaning process.

Laser pulse duration

Under a long laser pulse, the heat penetrates most of the substrate. In this case, the cleaning process can be more aggressive and less selective. For short pulse durations, the thermal diffusion length is small. In this case, there is a minimal heat-affected zone, and little to no substrate damage. In the range of ultra-fast laser pulse durations (for ps or fs lasers), the time scale is shorter than most energy transfer processes. This means that, during the pulse, only electrons are excited, while the material's atomic lattice is not affected. The absorbed laser energy is then accumulated by the electrons on the surface, and it cannot be transmitted to the substrate by heat conduction. This is why laser cleaning with ultra fast lasers is called cold ablation.

Angle of incidence of the radiation

If the laser beam is irradiated vertically, the temperature rise at the interface is limited by the shadow of pollutant particles on the substrate. If the laser beam forms a certain angle with the surface of the substrate, the interface between the particle and the substrate can absorb laser energy, significantly improving the cleaning efficiency. If the substrate is made of a non-absorbing material, the cleaning efficiency is greater by irradiation from the reverse side than that from the front side.

4.5 Estimates of thermal stress and radiation pressure

The type and nature of the physical mechanisms that contribute to the removal of dust particles depend strongly on the substrate material and also on dust properties. Here, some simplified simulations are presented to give an idea of the order of magnitude of some physical processes. Because of the pulse duration regime of the conducted DLC tests (22 ns), the focus of this section is the thermal effects, since the time scale is longer than that of electronic excitation and charge relaxation and the deposited energy becomes almost fully thermalized during the pulse. Also a study of the force from radiation pressure is presented.

The specific case discussed here reflects the situation that was experimentally analyzed (see Sect. 5.2), even though some approximations are made. In particular, we consider a single Mo particle, and suppose that it is cylindrical, with the axis perpendicular to the substrate, for geometrical simplicity. The particle has a radius $R=7.5 \mu\text{m}$ (which is the typical dimension of the particles used for the tests, see Sect. 5.2) and a thickness h so that $h > \delta_{opt}^p$ (the optical depth of the particle, see Sect. 4.5.1) and $h > L_{th}^p$ (the thermal diffusion length of the particle, see Sect. 4.5.1), and it is on a glass substrate with a thickness $l = 1 \text{ mm}$ (equivalent to the thickness of the used microscope slides), perpendicularly irradiated by a UV laser with a spot size of $5 \text{ mm} \times 5 \text{ mm}$ and pulse

duration $\tau_L = 22$ ns. Simulations were performed for two types of substrate: soda-lime glass, which was used for the experiment, and fused silica (SiO_2), which is being considered for future tests. Although soda-lime glass (SLG) is made of $\sim 70\%$ by fused silica (see Fig. 4.3), it exhibits significantly different optical properties from pure fused silica. In particular, as it can be seen in Fig. 4.4, for the wavelength at which the experiment was conducted (248 nm, see Sect. 5.1), fused silica is highly transmissive [31], while soda-lime glass has a transmission percentage approaching zero.

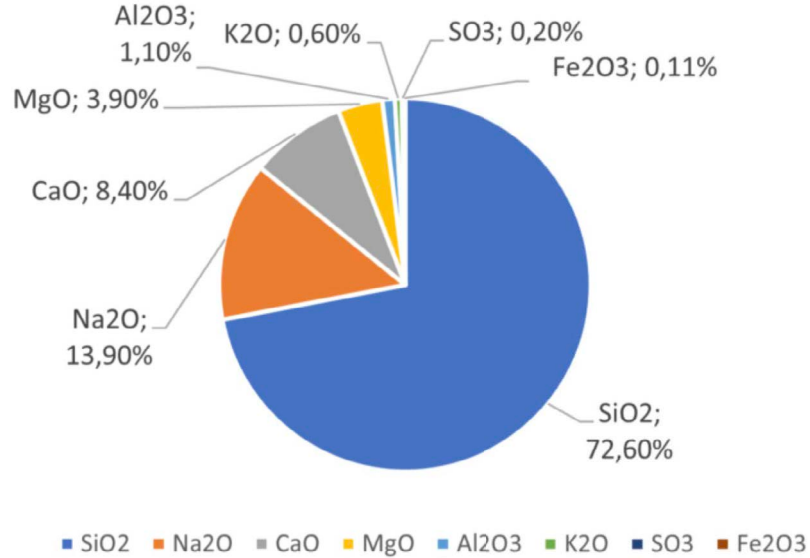


Figure 4.3: Chemical composition of soda-lime glass. Figure from [32].

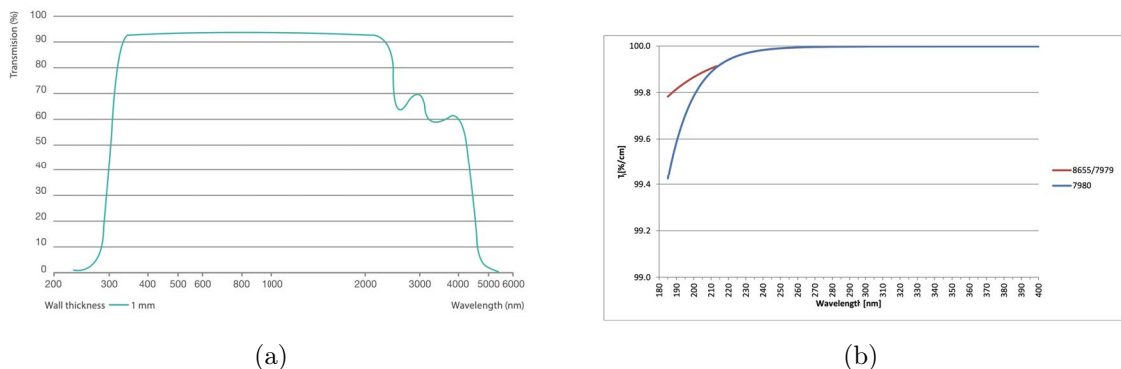


Figure 4.4: Percentage of transmission of the two different glasses as a function of the laser wavelength. Panel (a): 1 mm thick soda-lime glass substrate; panel (b): 1 cm thick fused silica substrate (two different types of fused silica are shown). Figures from [33] and [34].

All the numerical values used for this simulation are shown in Tab. 4.1. The absorption coefficient μ_α for soda-lime glass at 248 nm is taken from the Refractive Index database [35], while for fused silica it was calculated from the percentage of transmission T through the following relation (reflectivity \mathcal{R}^s for the glass is considered negligible):

$$T(x) = e^{-\mu_\alpha \cdot x} \quad (4.18)$$

where x is the considered thickness. Inverting the formula we find:

$$\mu_\alpha = -\frac{\ln T(x)}{x} \quad (4.19)$$

A lower limit for the percentage of transmission $T(x)$ of fused silica is given [34]: $T(x = 1 \text{ cm}) \geq 99.90\%$ at 248 nm. Through Eq. 4.19 this leads to an upper limit of $\mu_\alpha \leq 0.1 \text{ m}^{-1}$. For the simulation, the limit value $\mu_\alpha = 0.1 \text{ m}^{-1}$ was assumed.

	Mo	Soda-lime glass	Fused silica
$\rho [\text{g}/\text{cm}^3]$	10.22	2.5	2.20
$c_p [\text{J}/\text{kg}\cdot\text{K}]$	265	760	770
$k [\text{W}/\text{m}\cdot\text{K}]$	138	1.05	1.38
$T_m [\text{K}]$	2888	993	1873
$T_b [\text{K}]$	4912	—	—
$L_f [\text{J}/\text{kg}]$	$2.90 \cdot 10^5$	—	—
$L_v [\text{J}/\text{kg}]$	$6.25 \cdot 10^6$	—	—
$\gamma [\text{K}^{-1}]$	$5.2 \cdot 10^{-6}$	$8.9 \cdot 10^{-6}$	$0.5 \cdot 10^{-6}$
$\mu_\alpha [\text{m}^{-1}]$	$1.47 \cdot 10^8$	$6.3 \cdot 10^3$	$\lesssim 0.1$
$E [\text{Pa}]$	$3.29 \cdot 10^{11}$	$7.2 \cdot 10^{10}$	$7.3 \cdot 10^{10}$
ν	0.29	0.23	0.16
\mathcal{R}	0.6	~ 0	~ 0
$A_H [\text{J}]$	$5 \cdot 10^{-19}$	$8 \cdot 10^{-20}$	$8 \cdot 10^{-20}$

Table 4.1: Opto-thermal mechanical properties of the materials of interest: mass density ρ , specific heat c_p , thermal conductivity k , melting (or softening) and boiling temperature T_m and T_b , latent heat of fusion and vaporization L_f and L_v , thermal expansion coefficient γ , absorption coefficient μ_α , Young modulus E , Poisson ratio ν , reflectivity \mathcal{R} (which is assumed equal to zero for the glasses) and Hamaker constant A_H . Values from: [36], [37], [38], [39], [40].

4.5.1 Absorbed energy and temperature rise

First we study how much fluence and energy the two materials, substrate (defined by the superscript s) and particle (defined by the superscript p), absorb for different incident laser energy densities. From the absorption coefficient μ_α (Tab. 4.1) we can define the optical absorption depth: $\delta_{opt} = 1/\mu_\alpha$, which is reported in Tab. 4.2. For Mo $\delta_{opt} \simeq 7 \text{ nm}$, all the energy entering the particle is completely absorbed in a length that is thin with respect to the thickness h . The energy absorbed by the particle is:

$$E_{abs}^p = \mathcal{F}(1 - \mathcal{R}^p)\pi R^2 \quad (4.20)$$

where \mathcal{F} is the incident laser fluence in J/m^2 , \mathcal{R}^p is the particle reflectivity and R is the particle radius.

The energy absorbed by the substrate is (once again neglecting the glass reflectivity \mathcal{R}^s):

$$E_{abs}^s = \mathcal{F}(1 - e^{-\mu_\alpha^s \cdot l})A^s \quad (4.21)$$

where μ_α^s is the absorptivity of the substrate, l is the substrate thickness and A^s is the laser spot size. The difference here with respect to Eq. 4.20 is that we are not assuming $l > \delta_{opt}^s$ (a condition that is not verified for low-absorbing substrates, like fused silica, as shown in Tab. 4.2), hence we use Lambert-Beer's Law to calculate the absorbed fluence. In addition, we are neglecting a small correction due to the (small) glass reflectivity. Fig. 4.5 shows the absorbed energy and the absorbed fluence by the Mo particle and the two substrates as a function of the incident laser fluence. In all three cases the two quantities have a linear dependence on the incident laser fluence. The comparison of Fig. 4.5c and Fig. 4.5a shows that the Mo particle absorbs a fraction of the incident fluence, but the soda-lime glass substrate absorbs all of it, despite its absorption coefficient being orders of magnitude smaller than that of Mo. This is due to the reflectivity R^p , which limits the absorption. The energy absorbed by the Mo particle is a lot smaller than the one absorbed by the soda-lime glass, and this is due to the difference in the areas.

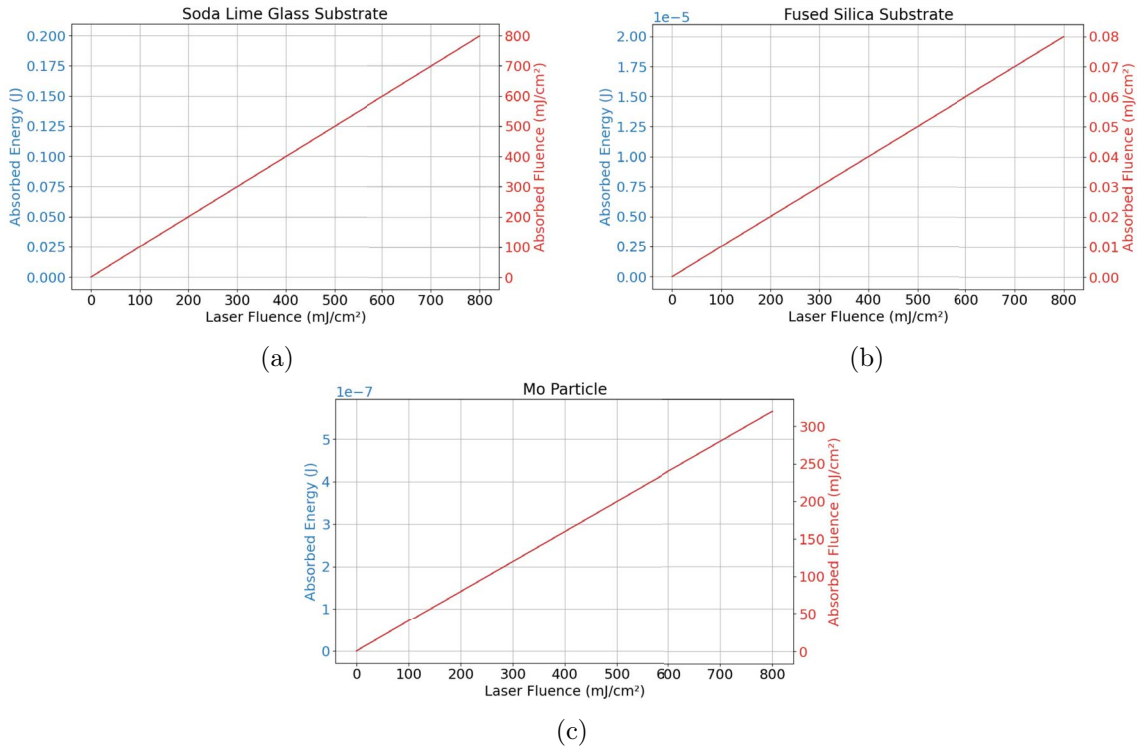


Figure 4.5: Plots of the absorbed energy and fluence for soda-lime glass (a), fused silica (b), and molybdenum (c). The scale for the absorbed energy is on the left (blue), while for the absorbed fluence (which for the substrate is calculated over the spot area $A^s = 5\text{ mm} \times 5\text{ mm}$) is on the right (red).

	δ_{opt} [m]	L_{th} [m]
Mo	$6.8 \cdot 10^{-9}$	$1.5 \cdot 10^{-6}$
SLG	$1.6 \cdot 10^{-4}$	$1.6 \cdot 10^{-7}$
Fused silica	$\gtrsim 10$	$1.9 \cdot 10^{-7}$

Table 4.2: Typical lengths for Mo, soda-lime glass and fused silica for an incident radiation of 248 nm and 22 ns.

Let us estimate how much the particle and the substrate heat up after one laser pulse. The two typical lengths for heat spread are the optical absorption depth δ_{opt} and the thermal diffusion length $L_{th} = \sqrt{(k\tau_L)/(\rho c_p)}$. By comparing these two, we find the mass for the two different materials (substrate and particle) that heats up after one pulse. For the Mo particle $L_{th}^p \gg \delta_{opt}^p$ ($L_{th}^p/\delta_{opt}^p \simeq 10^3$), the energy that was absorbed in the optical area, defined by the optical absorption depth, spread in L_{th}^p during the laser pulse, and the heated mass is proportional to L_{th}^p . For the substrates (soda-lime glass and fused silica) $L_{th}^s \ll \delta_{opt}^s$ ($L_{th}^s/\delta_{opt}^s \simeq 10^{-8}$ for fused silica and $\simeq 10^{-3}$ for soda-lime glass), there is no heat diffusion beyond the optical area. For fused silica, since $\delta_{opt}^s \simeq 10$ m $> l = 1$ mm, the heated mass is proportional to the thickness of the substrate. For soda-lime glass, $\delta_{opt}^s \simeq 10^{-5}$ m $< l = 1$ mm, and the heated mass is proportional to δ_{opt}^s . The temperature rise is:

$$\Delta T = \frac{E_{abs}}{m_h c_p} \quad (4.22)$$

where m_h is the heated mass. For the Mo particle $m_h^p = \pi R^2 \cdot L_{th}^p \cdot \rho^p = 9.7 \cdot 10^{-12}$ kg, while for the soda-lime glass substrate $m_h^s = A^s \cdot \delta_{opt}^s \cdot \rho^s = 9.9 \cdot 10^{-6}$ kg and for the fused silica substrate $m_h^s = A^s \cdot l \cdot \rho^s = 5.5 \cdot 10^{-5}$ kg. The temperature rise is a function of the incident laser fluence, and ΔT is shown for the three materials in Fig. 4.6. The temperature reached after the absorption, even at the highest incident laser fluence (800 mJ/cm²) is still far from the melting and boiling temperatures for the Mo particle, and from the softening temperature for the two glasses. The temperature rise is almost negligible for a fused silica substrate, due to the very low absorption, while the Mo particle shows the highest temperature rise of all three materials, reaching $\Delta T \simeq 800$ K for an incident laser fluence of 800 mJ/cm².

4.5.2 Force due to thermal stress

Let us estimate the impulsive force produced by the thermal expansion resulting from the absorption of the laser power. As an approximation, the contribution of the substrate's expansion is considered negligible, since $\Delta T^s \ll \Delta T^p$.

As a result of thermal expansion, the heated thickness of the particle L_{th}^p increases by:

$$\Delta L_{th}^p = L_{th}^p \gamma^p \Delta T^p \quad (4.23)$$

We assume that this length increases only upward. This comes from assuming that the rest of the particle volume that is not heated is rigid enough, so that the lower edge of L_{th}^p is at rest.

The center of mass of the layer that undergoes expansion moves up with an average speed equal to:

$$v = \frac{1}{2} \frac{\Delta L_{th}^p}{\tau_L} = \frac{1}{2} \frac{\gamma^p}{\tau_L} \frac{\mathcal{F}(1 - \mathcal{R}^p)}{\rho^p c_p^p} \quad (4.24)$$

and the average force that comes from this increase in speed is:

$$F = \frac{m_h^p v}{\tau_L} = \frac{\pi}{2} \mathcal{F}(1 - \mathcal{R}^p) R^2 \frac{\gamma^p}{c_p^p} \frac{L_{th}^p}{\tau_L^2} \quad (4.25)$$

The force induced by the thermal expansion of the particle must be compared with the estimated adhesion force, and the two contact models are the ones discussed in Sect. 4.1. The work of adhesion of the particle-surface system, W_{ij} , is calculated as: $W_{ij} =$

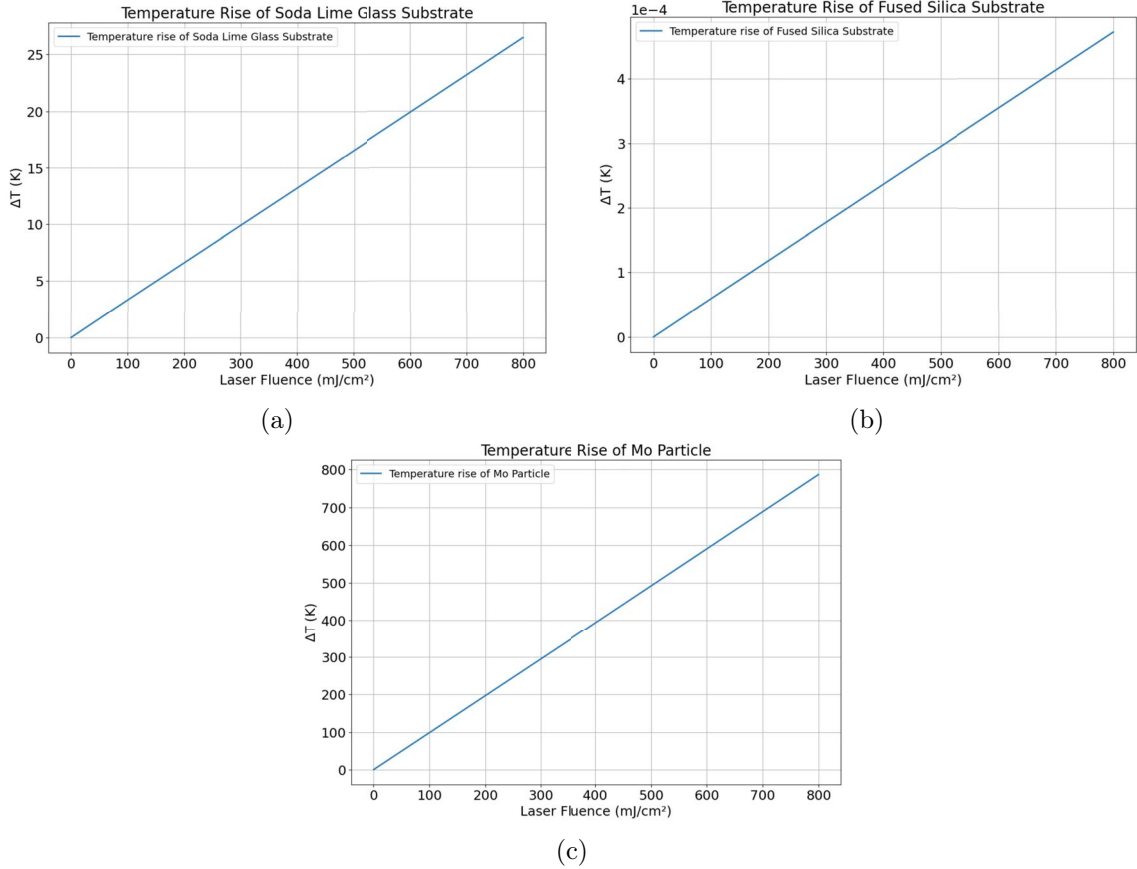


Figure 4.6: Plots of the temperature rise (with respect to room temperature) caused by one laser pulse versus the incident laser fluence. Panel (a) is for soda-lime glass, panel (b) fused silica, and panel (c) molybdenum.

$\sqrt{A_{Hi}A_{Hj}}/12\pi z_0^2$ [41], where $A_{Hi,j}$ is the Hamaker constant of the two materials (reported in Tab. 4.2), and $z_0 \sim 0.4$ nm is the assumed distance at contact [41]. Fig. 4.7 shows the force due to thermal stress as a function of the laser incident fluence, and the comparison with the contact models. The threshold fluence \mathcal{F}_{th} is the fluence corresponding to the intersection between the adhesion force and the thermal stress induced force, and is between 50 and 100 mJ/cm^2 for the JKR and DMT contact models, while $\mathcal{F} \simeq 200 \text{ mJ}/\text{cm}^2$ for the classical Hamaker model obtained integrating the attractive part of the potential at contact distance z_0 .

The same simulation was repeated for Mo particles of different size, to see the dependence of the threshold fluence \mathcal{F}_{th} on the particle diameter. This result is shown in Fig. 4.8. As expected, bigger particles require a lower incident energy density to be removed, due to their larger absorption cross-section and the relatively weaker effect of adhesion forces per unit mass.

These results are obtained through many approximations: only one cylindrical Mo particle is considered on a perfectly smooth glass substrate, thus we do not consider the effect of many Mo particles, that, even though are very uniform in size, are not perfectly spherical. The surface roughness of the substrate is also not taken into consideration when estimating the adhesion force, and the "kick" that comes from the rapid thermal expansion is calculated assuming that the substrate's expansion is negligible with respect to the particle's one.

4.5.3 Force due to radiation pressure

Radiation pressure can affect the cleaning efficiency. This mechanism can be studied under two hypothesis: the substrate is transparent and the laser irradiates the sample from the back, meaning it impinges on the clean face of the glass sample. Even if none of these conditions are met in the experiment described in this thesis (see Chapter 5), it is still worth discussing this effect and how it would compare with the force due to thermal stress. To estimate the force generated by this mechanism, we have to calculate the pressure due to momentum transfer. A fraction \mathcal{R}^p of the incident photons is reflected, a fraction $\mathcal{A}^p = 1 - \mathcal{R}^p$ (transmission is negligible) is absorbed. Under the hypothesis of a perpendicular incidence, an absorbed photon transfers a momentum of $h\nu/c$ (h is Planck's constant, ν is the photon frequency and c is the speed of light), a reflected one transfers $2h\nu/c$. The average transferred momentum per photon is [42]:

$$\Delta p = \mathcal{A}^p \frac{h\nu}{c} + \mathcal{R}^p \frac{2h\nu}{c} = \frac{h\nu}{c} (\mathcal{A}^p + 2\mathcal{R}^p) = \frac{h\nu}{c} (1 + \mathcal{R}^p) \quad (4.26)$$

The force is the rate of photons \dot{N} times the transferred momentum per photon:

$$F_p = \dot{N} \Delta p = \frac{IA^p}{h\nu} \cdot \frac{h\nu}{c} (1 + \mathcal{R}^p) = \frac{IA^p}{c} (1 + \mathcal{R}^p) \quad (4.27)$$

here, $I = \mathcal{F}/\tau_L$ is the laser intensity, \mathcal{R}^p is the reflectivity of the particle and A^p is the projected area of the particle on the substrate. Thus, if we neglect the absorption from the substrate and suppose that the laser beam impinges perpendicularly to the surface from the back, the resulting force as a function of the incident fluence is shown in Fig. 4.7.

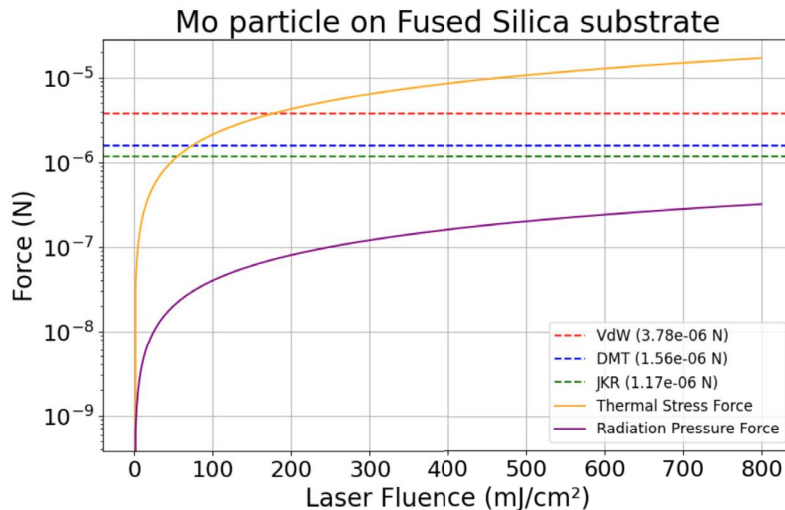


Figure 4.7: Comparison of the forces induced by thermal stress and radiation pressure with the adhesion force models. The system considered is one single Mo particle on a fused silica or soda-lime glass substrate, since the effect of the substrate's expansion is considered negligible here. The solid yellow and purple lines represent the forces induced by thermal stress and radiation pressure respectively. The dashed lines represent the adhesion force models: DMT in blue, JKR in green and the integration of the attractive part of the Van der Waals potential in red. This is calculated at a typical contact distance of 0.3-0.4 nm.

Even if we radiate from the back the particle and consider a perfectly transmissive substrate, the radiation pressure force is still much smaller than the one from thermal stress, and the generated force never overcomes the adhesion in the fluence range of interest.

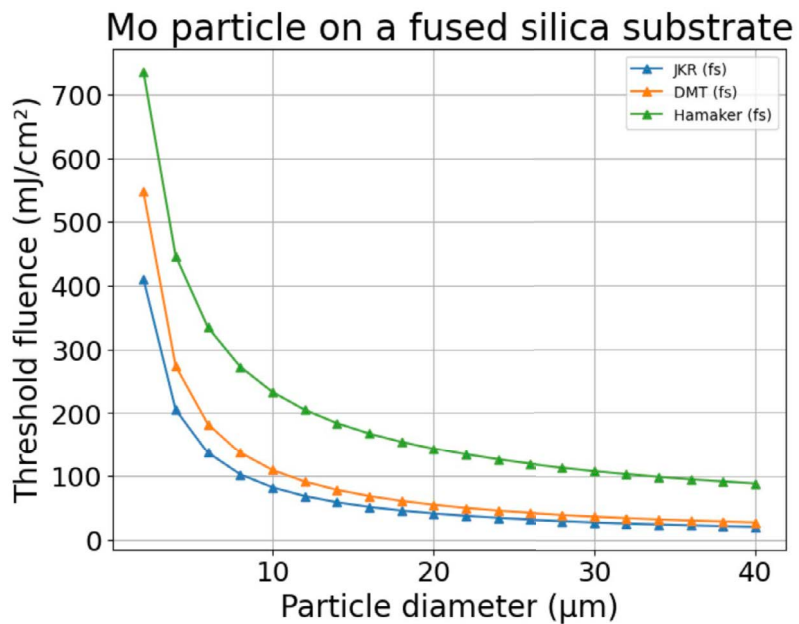


Figure 4.8: Threshold fluence (the intersection between the thermal stress curve and the dashed lines in Fig. 4.7) versus Mo particle diameter. The system considered is one single Mo particle on a fused silica or soda-lime glass substrate, since the effect of the substrate's expansion is considered negligible here. The trend is shown for the three different adhesion force models: DMT in orange, JKR in blue and the integration of the attractive part of the Van der Waals potential in green.

Chapter 5

Tests of Dry Laser Cleaning

In this thesis we conducted first tests of the DLC oriented towards application to GW detectors. As a source, we used the excimer laser available at the Physics and Astronomy Department of University of Padova. We considered dust particles of different materials (Mo and environmental dust) on SLG substrates. SLG was chosen as the available substrate, even if non-ideal for the laser wavelength as shown in Fig. 4.4. Different tests were done by changing not only the dust material, but also the laser fluence and number of pulses.

This chapter describes the laser experimental setup, in particular the different voltage settings, the energy density range and the pulse duration, and explains how the samples were prepared for the laser processing.

5.1 Laser source

The laser used for the laser cleaning tests is a Coherent - Compex PRO 201F, a KrF excimer laser, a type of gas laser that uses excimers as the gain medium. The main characteristic is that the gain medium is unstable. When an external energy excites the medium, the gas forms molecules with very short lifetimes (tens of nanoseconds), which are called excimers. Normally, chemically stable inert gases such as He, Ne, Ar, Kr, and chemically active halogens such as F, Cl, Br form a mixed gas, which is used as the gain medium, and they do not combine to form molecules. If the gas chamber is given appropriate excitation, the two types of atoms can form excited excimers, which have a very short lifetime and will quickly transition back to the ground state. These molecules have an even shorter lifetime and will immediately revert to the original two types of atoms. This mechanism easily forms population inversion. In the used source, the active medium is made of a mixture of Kr, F₂ and Ne. KrF excimers are generated through a high-voltage discharge. Their dissociation into elemental components releases a UV pulse (248 nm) with a pulse width of 22 ns.

The scheme of the laser delivery unit is reported in Fig. 5.1, and a photo is shown in Fig. 5.2. A double-mirror attenuator is placed right after the laser to reduce the energy of laser pulses, this is followed by a series of lenses and mirrors that shape and divert the beam. Two homogenizer arrays (matrices of micro-lenses used to split, mix and recombine the beam to obtain a uniform intensity) are used to turn the Gaussian intensity profile of the laser into a beam with uniform intensity over a square area of 5 mm × 5 mm. A beam splitter allows to monitor the intensity with a diode energy detector, a calibrated photodiode that receives a small fraction of the beam to measure its energy along the path. Its output is also used to drive the attenuator and stabilize the delivered energy. Before

being focused onto the sample, the beam is passed through a mask that crops its edges and transmits only the central region with the most uniform intensity. This ensures a well-defined beam shape and size on the target and removes residual edge inhomogeneities or stray light generated along the optical path. The sample is placed on a horizontal, XY translation stage and the laser impinges on it at null angle of incidence.

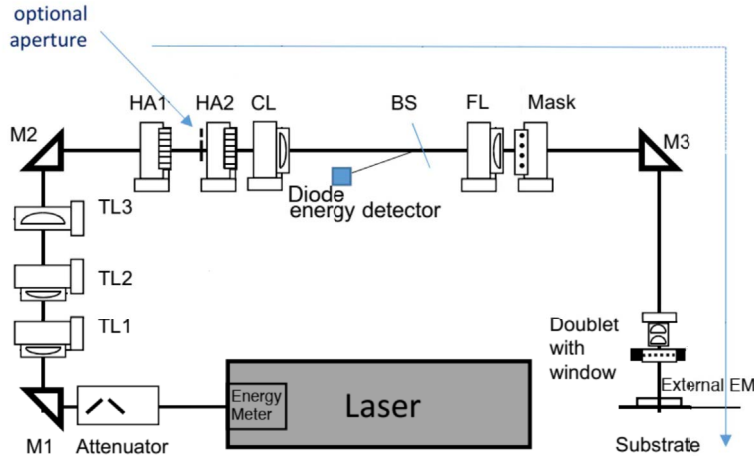


Figure 5.1: Scheme of the laser beam delivery unit. Figure from [43].

The energy density (ED) that can be delivered with this unit can range between 40 and 1200 mJ/cm² by adjusting the charging voltage, which charges the main capacitor. The capacitor is directly connected to the active medium chamber, and when it discharges through the KrF gas it generates the excimer molecules. At a given charging voltage, the laser can produce energy densities only within a specific limited range. The maximum repetition rate that can be reached by the laser is 10 Hz.

The setup can be controlled via software: for each sample, we could define a grid of spots in the XY plane (on the laser reference frame) to be shined by the laser, each at a specific combination of ED and number of pulses; during the laser processing the actual ED corresponding to each spot is measured and stored (this is possible thanks to the in-line diode detector).

Each time a new charging voltage is set, we need to conduct a stabilization procedure before the actual processing: each test is run on a dummy sample (a trial microscope slide), and the software then provides the EDs for every spot. During this phase, we aim to minimize the difference in percentage of the measured ED from the target (originally set) ED. This procedure is repeated two or three times, in order to obtain a percentage difference $\lesssim 5\%$ for each spot.

5.1.1 N₂ flux

It is possible to direct a constant N₂ flux toward the sample through a small tube. The flow rate can range from 0 to 20 liters/min. In the research conducted with this laser, the flux is required to reduce the oxygen concentration on the sample. In our laser cleaning tests we studied some samples that had been processed under the influence of the N₂ flux to determine its effect on the cleaning efficiency. During this phase, we took care that particles from unprocessed areas could not deposit on already processed spots, so not to mask the effect of the DLC. In this way, we tried to avoid any dust contamination on spots



Figure 5.2: Photo of the KrF excimer laser source.

previously treated. The photo in Fig. 5.3 shows the position of the N₂ tube with respect to the laser stage.

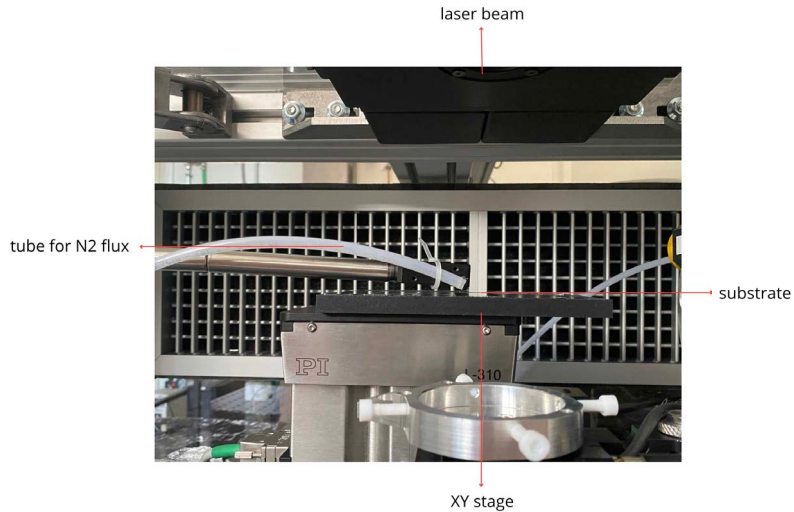


Figure 5.3: Front view of the laser stage. The tube on the left emits a constant N₂ flux from left to right and it is directed on the spot being processed. The laser beam impinges from the top on the substrate, placed on the mobile XY stage of the laser.

5.2 Preparation of the samples

The substrates are microscope slides made of soda-lime glass, with an area of 26 mm × 76 mm and a thickness of 1 mm. Every substrate was cleaned with isopropyl alcohol (IPA) before depositing the dust to test the DLC technique. Two types of contaminants were studied:

- Mo particles, of known size and shape. The 10th, 50th and 90th diameter percentiles are respectively 10.9 μm, 16.2 μm and 24.1 μm.

- Environmental dust particles, of unknown shape and composition. During the analysis, the size distribution of the environmental dust was characterized (see Sect. 6.6) and its composition was investigated (see Sect. 6.9.2).

Each substrate, regardless of the type of dust deposited on it, is divided into a 10×4 grid of $5 \text{ mm} \times 5 \text{ mm}$ squares. The columns and rows are spaced 1 mm apart. Each square is inspected at the microscope before and after the processing, as described in Chapter 6.

5.3 Laser processing

Different DLC tests were conducted at an exploratory level. These allowed us to identify the ED ranges and the numbers of pulses to use for the conclusive tests of this thesis. For brevity, I only describe the setting and procedure for these final tests.

The day before the laser processing, 7 samples were prepared, as explained in Sect. 5.2, and imaged using a microscope (see Sect. 6.1): 3 slides were covered with environmental dust, 3 with Mo dust, and one was left exposed to the air, without any dust being deposited on it.

Two types of laser settings were tested:

- One single voltage value (V_1) fed to the laser for the entire sample. In this case the sample is processed all at once, and the ED is made to vary from 100 mJ/cm^2 in the bottom row to 730 mJ/cm^2 in the top row; the number of pulses varies by column from 1 in the leftmost column to 2, 4 and 8 (in the rightmost column). In the following, these samples are labeled as "1 laser setting".
- Two different voltage values (V_2 and V_3) fed to the laser for one sample, to extend the ED range. In this case the same sample is treated for some spots with a lower voltage (V_2) to the laser so to vary the ED from 50 to 390 mJ/cm^2 , and for the remaining spots with a higher voltage (V_3) so to vary the ED from 475 to 815 mJ/cm^2 . In the following, these samples are labeled as "2 laser setting".

The reason for treating the same sample with two different laser voltages was not only to have a wider ED range, but also to study the effect of the laser stabilization: this is required each time the laser voltage is changed. Fig. 5.4 shows a scheme of a soda-lime glass sample, with the gray squares representing the different laser spots, and the order of the processing is also indicated.

Before starting a laser process, the precise spacing and dimensions of the imaged areas is checked by processing a piece of thermal paper with the same pattern and one single ED (around 50 mJ/cm^2). Then, a test on a dummy sample is conducted with the recipes that are going to be used for the actual processes. In this way, the pulse pattern is verified.

After the preliminary tests, the first samples are processed. First, we processed 2 samples (one with dust, one with Mo) with the two-voltages setting: for each sample we run the stabilization for the lower ED values, processed the first 5 rows (see Fig. 5.4); then we changed the voltage and did the stabilization and process again for the remaining 5 rows. Then we went on with the one-voltage setting: for each sample, we run the stabilization for the ED range of interest and then processed all 40 spots with the same voltage. This was done for 4 samples: 3 without the N_2 flux (Mo, dust and clean) and one with the N_2 flux (dust). The following actions were executed in this order:

1. Laser voltage is set at V_2

- Stabilization process for the recipe in the range 50 - 390 mJ/cm² on a dummy sample.
- Processing of the first 5 rows of a Mo sample (Mo1) in the range 50 - 390 mJ/cm².

2. Laser voltage is set at V_3

- Stabilization process for the recipe in the range 475 - 815 mJ/cm². During this procedure, the sample was removed from the laser stage and kept in its wafer box.
- Processing of the last 5 rows of Mo1 sample in the range 475 - 815 mJ/cm².

3. Laser voltage is set at V_2

- Stabilization process for the recipe in the range 50 - 390 mJ/cm² on a dummy sample.
- Processing of the first 5 rows of a dust sample (Dust1) in the range 50 - 390 mJ/cm²

4. Laser voltage is set at V_3

- Stabilization process for the recipe in the range 475 - 815 mJ/cm². During this procedure, the sample was removed from the laser stage and kept in its wafer box.
- Processing of the last 5 rows of Dust1 sample in the range 475 - 815 mJ/cm².

5. Laser voltage is set at V_1

- Stabilization on a dummy sample and processing of a Mo sample (Mo2) in the range 100 - 730 mJ/cm².
- Stabilization on a dummy sample and processing of a dust sample (Dust2) in the range 100 - 730 mJ/cm².
- Stabilization on a dummy sample and processing of a clean sample (Clean) in the range 100 - 730 mJ/cm².
- Stabilization on a dummy sample and processing of a dust sample (Dust3) in the range 100 - 730 mJ/cm², with the addition of a N₂ flux of 8 l/min.

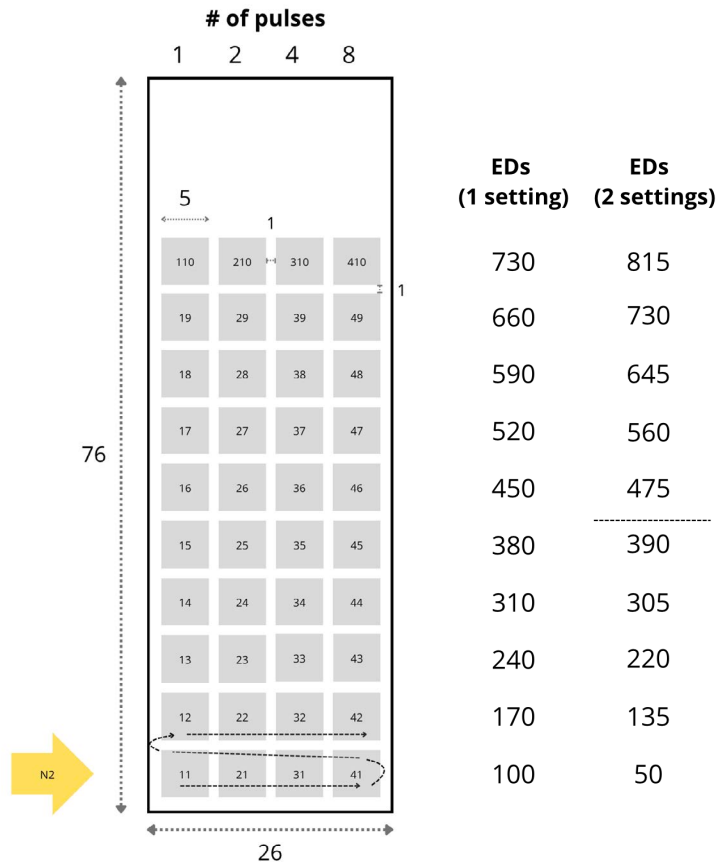


Figure 5.4: Representation of the substrate and the DLC scheme. All the lengths indicated are in mm. On the left: the microscope slide ($26 \text{ mm} \times 76 \text{ mm}$) is shown with black lines. The laser footprint for the DLC ($5 \text{ mm} \times 5 \text{ mm}$) is represented by gray squares, numbered as shown. On the right: EDs [mJ/cm^2] corresponding to each row, in the one-voltage case (leftmost column) and the two-voltages case (rightmost column). The number of pulses is fixed for each column and ranges from 1 to 8 as indicated at the top of the figure. The processing order of the squares is indicated by the dashed line, from the bottom left (square 11) to the top right (square 41). The N_2 flux is oriented from left to right and is always centered on the area being processed.

Chapter 6

Analysis of the samples

The analysis procedure consists of preparing the samples as described in Sect. 5.2, imaging and characterizing them, applying the processing steps outlined in Sect. 5.3, and finally repeating the imaging and analysis to determine the DLC efficiency by comparing the results obtained before and after processing. The photos were analyzed using a microscope to identify the particles left after the DLC process, and consequently study the efficiency of the process.

This chapter provides, in Sect. 6.1 - 6.3, an overview of the software used for particle recognition and describes the photo acquisition procedure. The plots and results enabling evaluation of the DLC efficiency are then presented in Sect. 6.4 - 6.9, showing the critical points that led to a deeper investigation of some observed phenomena.

6.1 Microscope

The microscope used for the analysis is a Keyence VHX-7000 digital microscope [44]. It is equipped with a monitor, a camera unit with a fully-integrated (FI) head and a console; two objectives, E20 and E500, incorporating different lenses are mounted on the microscope head, and are used depending on the required magnification level: each setting corresponds to a different field of view (FoV) and spatial resolution (quantified by the conversion factor from pixels to microns). The image is digitalized by a 1/1.7 inch CMOS¹ sensor with 12.2 megapixels and is 2160 × 2880 pixels in size (H × W). Focus can be adjusted both manually or automatically, thanks to the auto-focus function.

The microscope is equipped with a motorized stage that moves along the X, Y and Z axes, while the head is also motorized and moves along the Z axis. The movements have a resolution of 0.1 μm . Depending on the shape and type of samples to be analyzed, different sample holders can be mounted on the stage. For the purposes of this thesis, a microscope slide holder (shown in Fig. A.1) was used. This can hold up to four slides, but the microscope only allows the area of the two slides in the middle spots to be visualized. Most recently, a newer microscope holder was designed and produced which hosts 3 slides that can all be imaged within the movement range of the plate.

All the main photos of each treated spot were taken with a x50 magnification, which presents the characteristics reported in Tab. 6.1. At x50, the field of view is 6019.2 $\mu\text{m} \times$ 4514.4 μm : compared with the laser spot (a 5 mm × 5 mm square as discussed in Sect. 5.1), this means that, if the photo is centered on the center of each square (the coordinates of which are available in the laser frame), the left and right edges will be included, but not

¹Complementary Metal-Oxide-Semiconductor, converts light into an electric signal.

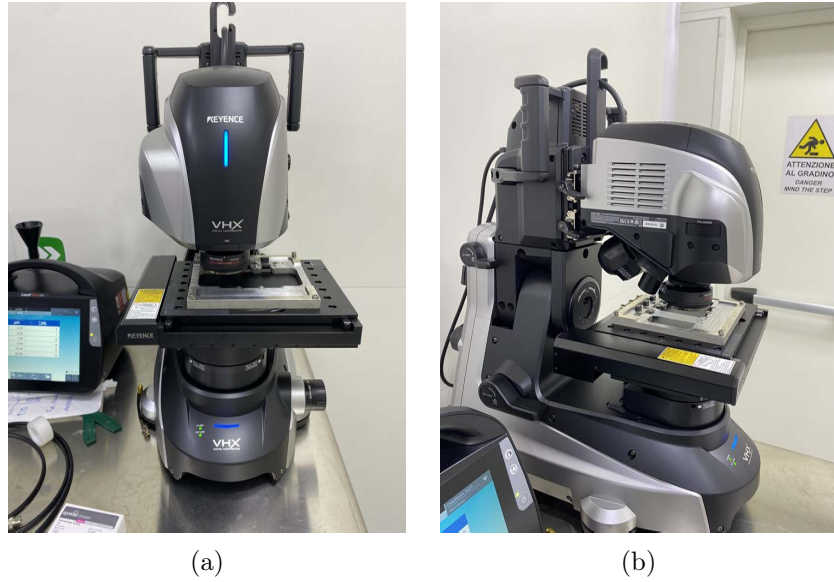


Figure 6.1: Front (a) and lateral (b) view of the FI head of the microscope.

the top and bottom ones.

Zoom	Res [$\mu\text{m}/\text{px}$]	H [μm]	W [μm]	FoV [mm^2]
x20	5.24	11318.4	15091.2	170.8
x30	3.51	7581.6	10108.8	76.6
x40	2.61	5637.6	7516.8	42.4
x50	2.09	4514.4	6019.2	27.2
x80	1.3	2808	3744	10.5
x100	1.04	2246.4	2995.2	6.7
x500	0.2	432	576	0.2
x700	0.15	324	432	0.14
x1000	0.1	216	288	0.06
x1500	0.07	151.2	201.6	0.03
x2000	0.05	108	144	0.012
x2500	0.04	86.4	115.2	0.01

Table 6.1: Properties and conversion factors for different magnification levels. It is specified the resolution (the value in microns of each pixel), the height (H), width (W) and the field of view (FoV) of a photo taken with each zoom.

6.1.1 Software for particle recognition

The Keyence microscope is equipped with a particle recognition software which we use to identify and size particles on our samples. The following procedure was applied, and then automatized, for the acquired photos: first, a luminosity threshold needs to be set. The threshold is used to binarize the image, and it is discussed in depth in Sect. 6.5. After that, the software identifies clusters of dark pixels as particles and produces a CSV file with a list of all the particles found and their characteristics. The first rows display some statistics of the recorded quantities for the interested image (average, standard deviation, maximum

value, minimum value and the sum of that value over all the particles). The rest of the file displays the same information for the single particles found, and each row corresponds to a particle. The columns record the following quantities (each with unit specified): "Area ratio", "Perimeter", "Circularity", "Area", "Circle equivalent diameter", "Gravity center X", "Gravity center Y", "Diagonal width", "Max diameter", "Min diameter", "Max diameter angle", "Min diameter angle".

6.2 Automation of photo acquisition

In order to study the effect of the laser processing on the particles deposited onto the substrates, we take a photo on the same area (centered on the laser spot) before and after the processing, and then compare the number of particles (NoP) and the percentage of area covered by dust particles (PAC).

To perform the image acquisition in an automated way, we adapted a script that was developed and is used to image silicon wafers for the purpose of monitoring dust deposition in Virgo [20]. The script requires as input the coordinates of the spot centers in its reference frame. The origin of the microscope's internal coordinate system is located at the top right: the y-coordinate goes from top to bottom, the x-coordinate from right to left. This must be taken into account when locating the centers of the spots given in the laser's coordinates, which have the origin on the bottom right. Since the coordinates are measured in the microscope frame, we have to apply a translation of the origin, the reflection of the Y axis (which is inverted in the two reference frames), and a possible rotation of the sample on the holder with respect to the original perpendicular position assumed during the processing. The automated sequence is the following:

1. Take as input the 4 corners of the glass sample (they need to be provided and adapted for each slide). They are ordered [1,2,3,4] in the following way: lower right (1), upper right (2), upper left (3), lower left (4)
2. From these points, calculate the rotation of the rectangular sample with respect to the coordinate frame of the microscope stage and the distance of corner (1) from the origin of the reference frame of the microscope stage
3. Apply the transformation to the grid points: translation, rotation and Y axis inversion.
4. Go at each point of the transformed grid at x50 and starts the auto-focus procedure
5. If auto-focus is successful, take the picture and move to the following spot

The total automated procedure takes around 17 minutes per sample [45]. The final result is a total of 40 photos (one for each spot) for each sample.

6.3 DLC experiment and analysis procedure

Once the photo acquisition procedure is automated, the DLC experiment procedure starts. In this section, we list all the steps applied to the samples:

1. The slides are cleaned with IPA and dust is deposited on them (Mo or environmental, as described in detail in Sect. 5.2).

2. The contaminated slides are photographed, with the automated procedure described in Sect. 6.2. The obtained photos are analyzed with the Keyence particle recognition software (Sect. 6.1.1).
3. The photographed slides are laser processed, with the different laser settings, as explained in Sect. 5.3.
4. Once the samples are processed, they are photographed again with the microscope and the photos after the DLC procedure are analyzed with the particle recognition software.

The 10×4 photos at x50 for the samples treated with one laser setting are shown in Fig. 6.2 and 6.3, 6.4 and 6.5, 6.6 and 6.7, while the photos for the two-settings samples are in Fig. B.1 and B.2, B.3 and B.4. Here the columns are inverted with respect to the actual processing scheme shown in Fig. 5.4: the top row shows the spots treated at the lowest ED, the bottom row the ones treated at the highest ED. The order of the number of pulses is unchanged, so it varies from 1 (in the leftmost column) to 2, 4 and 8 (in the rightmost column).

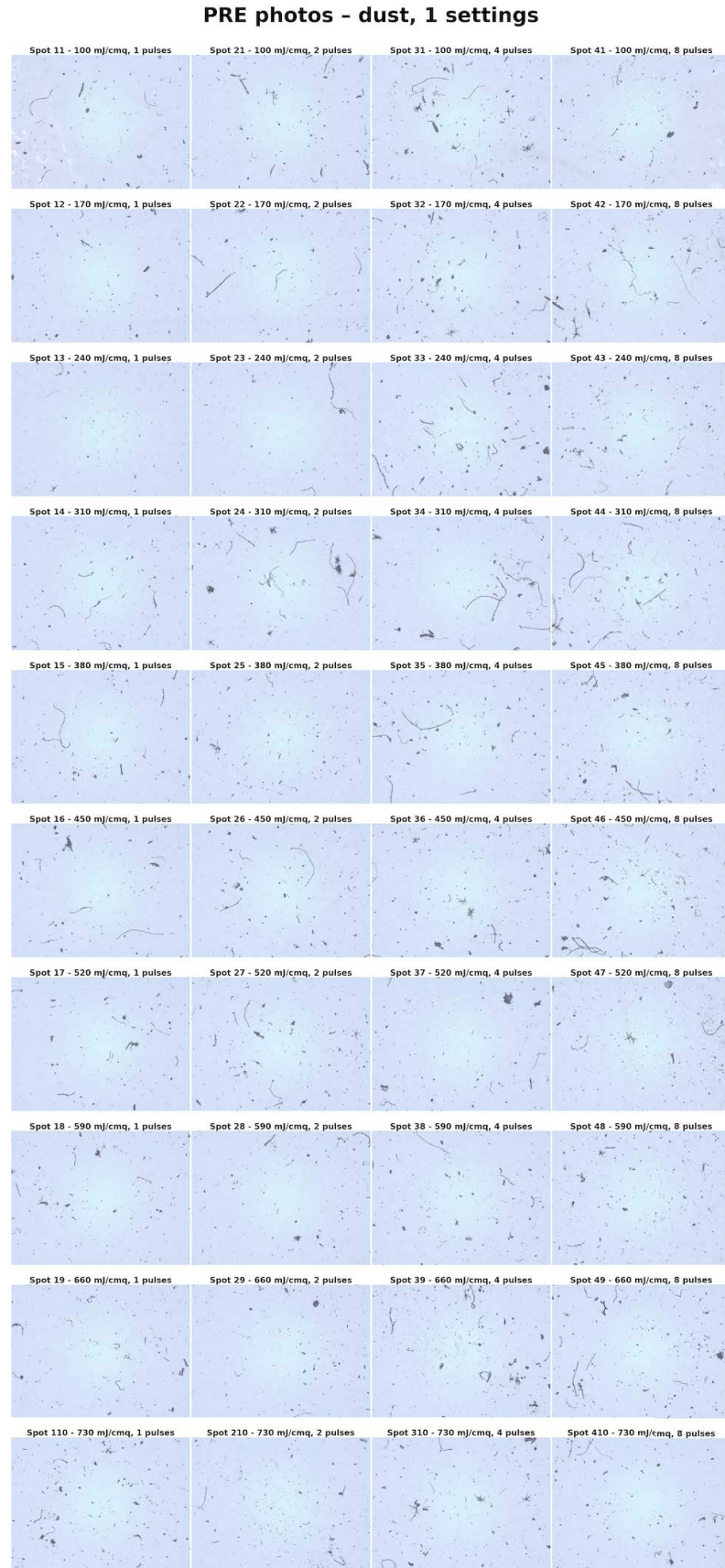


Figure 6.2: Photos of the dust sample treated with 1 laser setting before the laser process.

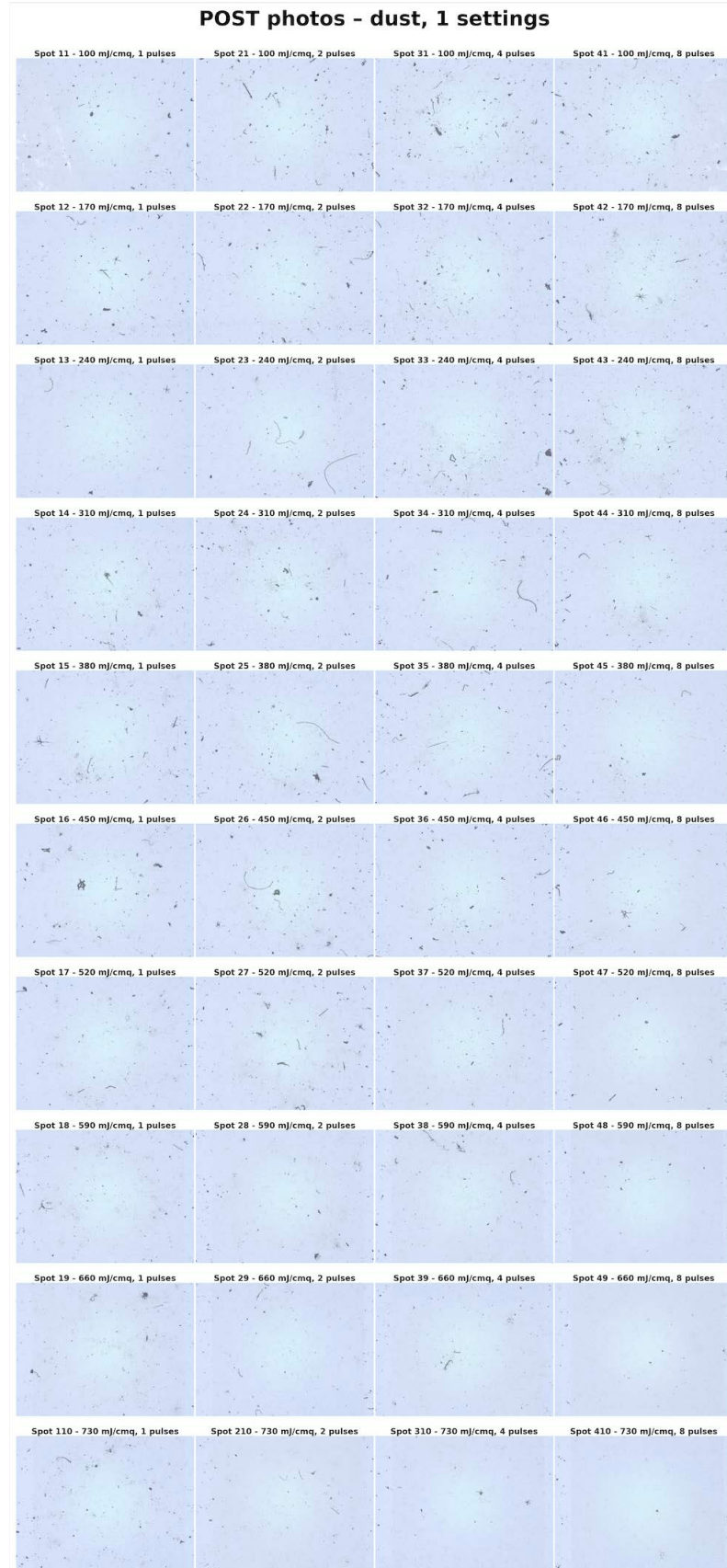


Figure 6.3: Photos at x50 of the dust sample treated with 1 laser setting after the laser process.

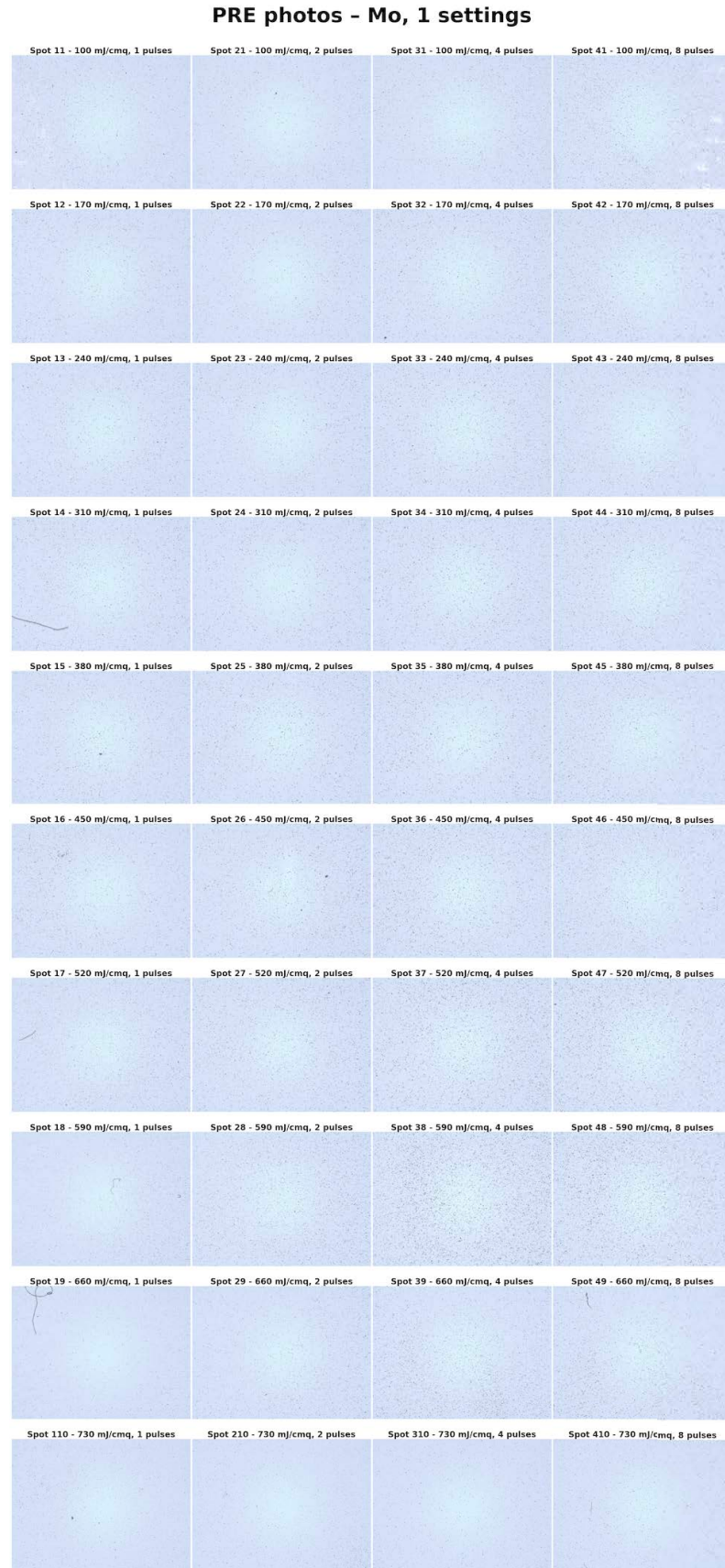


Figure 6.4: Photos of the Mo sample treated with 1 laser setting before the laser process.

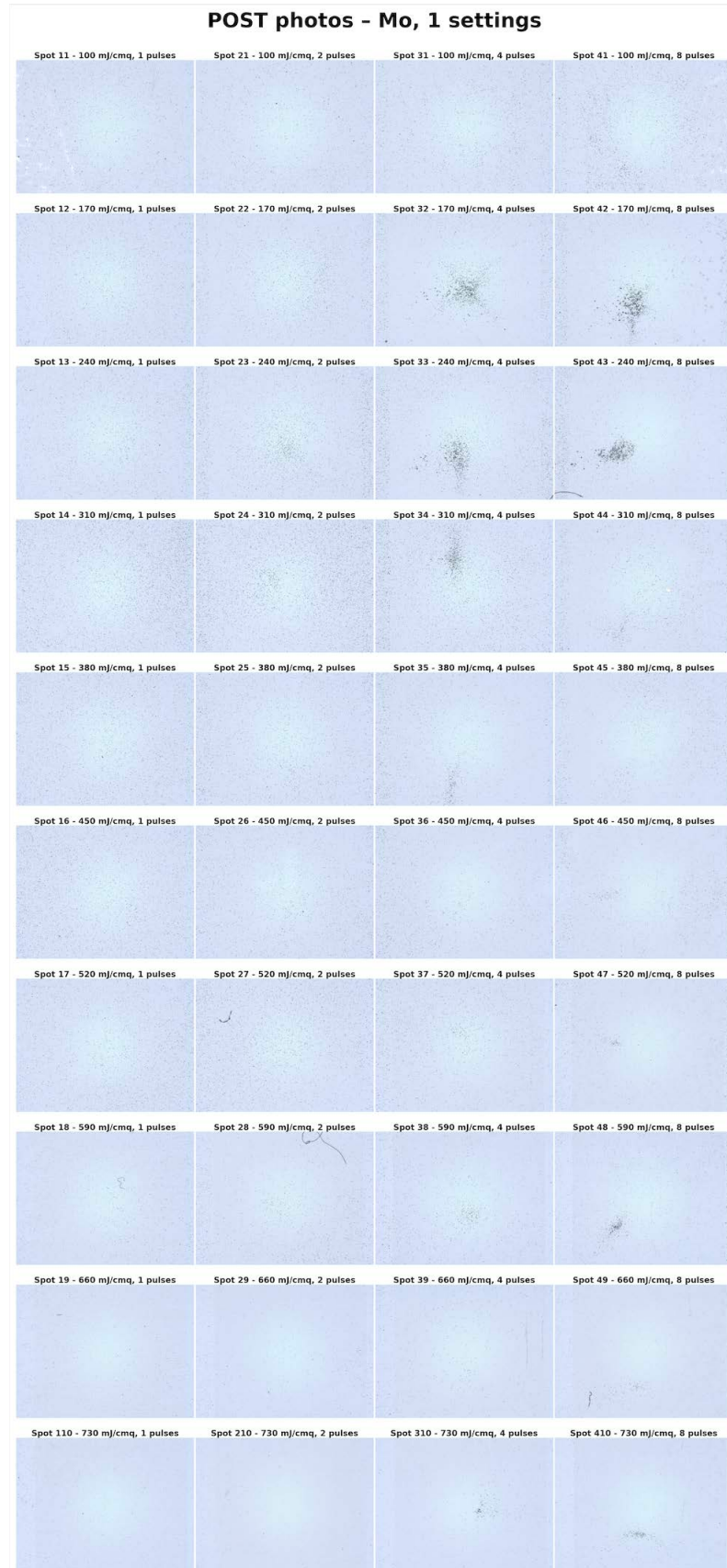


Figure 6.5: Photos of the dust sample treated with 1 laser setting after the laser process.

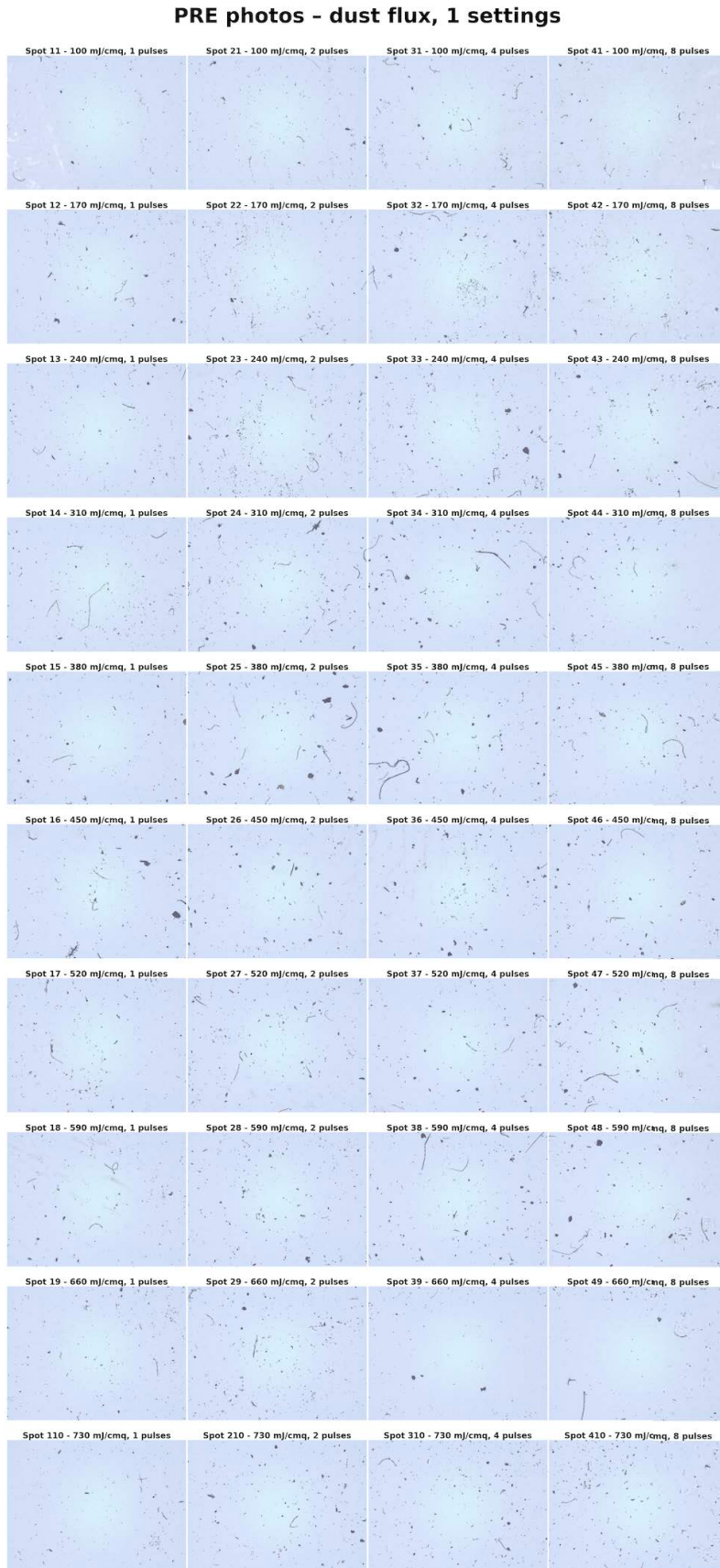


Figure 6.6: Photos of the dust sample treated with 1 laser setting and 8 liters/min N₂ flux before the laser process.

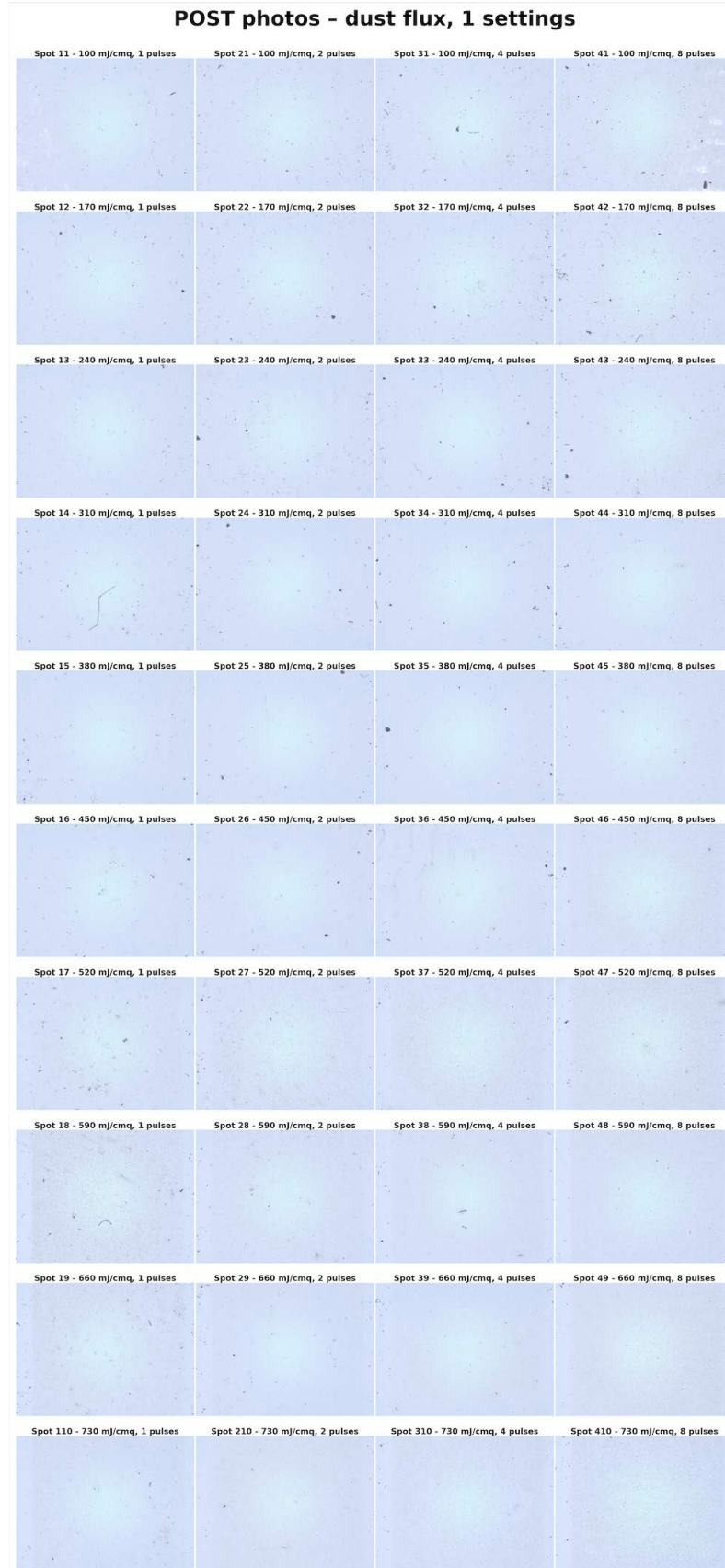


Figure 6.7: Photos of the dust sample treated with 1 laser setting and 8 liters/min N₂ flux after the laser process.

6.4 Analyzed quantities: PAC and NoP

From the CSV output file, we filter the set of found particles by imposing an area cut $A > 4 \text{ px}$. This value has been found as the optimal one for reducing fluctuation due to the background while cutting out the minimum number of small particles possible [20]. The filtered CSV file contains all the information on the selected particles that we can start analyzing. Here we define the two evaluated quantities for the analyses shown in the following sections.

- *Number of Particles* (NoP): the number of rows of the filtered file, excluding the ones containing the global statistics of the picture
- *Percentage of Area Covered* (PAC): it is obtained by summing over all the "Area" values and dividing by the total area covered by the field of view: $PAC = \sum_i A_i / A_{tot}$, where A_i is the area of the i -th particle (row in the CSV file) and A_{tot} is the area of the photo.

The PAC provides a more reliable measure of the actual increase or decrease in particle contamination, as it is less sensitive to fluctuations caused by small or numerous particles that may be incorrectly identified as individual particles or clustered together during detection (as is discussed in Sect. 6.5).

6.5 Luminosity threshold study

The key parameter that allows the microscope software to distinguish pixels belonging to a particle from those belonging to the background is the luminosity threshold. This threshold is used to binarize the images: the intensity of each pixel is compared to the threshold value and classified accordingly. Choosing this value is crucial, as it directly influences the reliability of the analysis.

Because the illumination is coaxial, the images are acquired in bright-field mode, where particles appear dark against a bright background. If the threshold is too low, some lighter particles may not be detected, leading to false negatives. Conversely, if the threshold is too high, brighter pixels from the substrate background may be mistakenly identified as particles, producing false positives.

The optimal threshold strongly depends on the surface roughness of the substrate, because rough surfaces introduce local variations in reflectivity and illumination that affect the background pixel intensity. In a bright field configuration, a smooth surface would produce a uniform background. However, when the surface is rough, irregularities scatter and absorb light differently across the image. As a result, the background becomes heterogeneous: some regions appear darker, while others remain bright.

To find the optimal threshold, some brand new microscope slides were analyzed at different threshold values. Two different situations were studied: a clean slide that was taken straight out of the box and imaged with the microscope, and a clean sample that was taken out of the box, cleaned with IPA, and then imaged with the microscope.

For this study, we analyzed the photos with threshold values ranging from 100 to 250, discretized in unitary steps, and, for each threshold value, we extracted the NoP and the PAC.

The results for the two different samples are shown in Fig. 6.8. For the slide in Fig. 6.8a we observe an abrupt increase in the NoP and of the PAC for a threshold $T \simeq 225$, while for the slide in Fig. 6.8b this happens for a threshold $T \simeq 180$. From this analysis alone, the

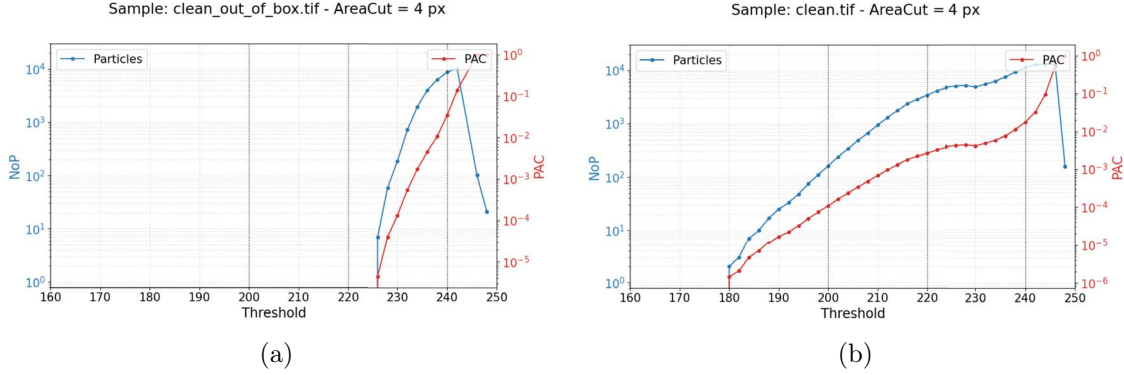


Figure 6.8: NoP and PAC vs luminosity threshold for two different slides. Panel (a) shows the results for a clean slide taken straight out of the box, while panel (b) shows the results for a new slide cleaned with IPA.

IPA cleaning procedure seems to affect the background and reduce the "limit threshold" (for which the software starts to detect particles). To assess this effect, additional tests were performed on different slides. A clean slide was analyzed after being taken out of the box. Then, it was cleaned with IPA and analyzed again.

The plots for this microscope slide are shown in Fig. 6.9. It can be seen that the sample taken directly out of the box has a lower limit threshold than that found for the sample reported in Fig. 6.8a, $T \simeq 185$, and this does not change significantly after the cleaning procedure, reaching a value of $T \simeq 180$. We can then conclude that the IPA cleaning procedure is not responsible for changes in the limit threshold: the ideal luminosity threshold can be different even for slides treated in the same way.

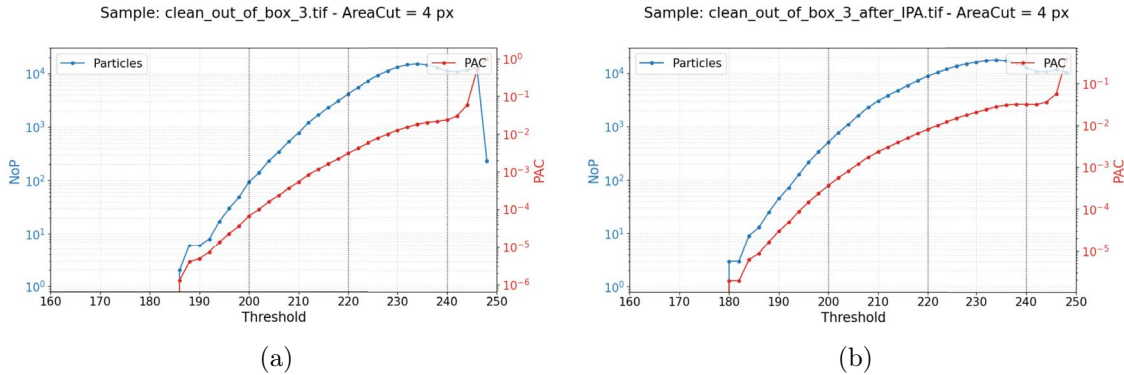


Figure 6.9: NoP and PAC vs luminosity threshold for the same slide in two different conditions. Panel (a) shows the results for the slide taken straight out of the box, panel (b) is for the same slide after being cleaned with IPA.

The limit luminosity threshold was also studied for samples covered with dust (environmental and Mo) that had been laser processed: we analyzed a spot free from dust particles on various samples at different luminosity threshold values. In particular, the dust and Mo samples treated with no flux, 1 and 2 laser settings (labeled as Dust1, Dust2, Mo1 and Mo2) were studied for this purpose. The NoP and PAC versus luminosity threshold plots for these samples are shown in Fig. 6.10. The two dust samples have a limit threshold $T \simeq 180$, whereas the two Mo samples show very different values. False positives start to appear for the Mo1 sample at a luminosity threshold $T \simeq 220$ and for the Mo2 sample

at $T \simeq 170$. On the basis of Fig. 6.10, we chose a conservative threshold $T = 160$: all images reported in the following are analyzed with this threshold value. For comparison, we also show the plots resulting with a threshold $T = 200$, a value initially used copying from previous work of the group: $T = 200$ optimized for silicon wafers as substrates, used for dust monitoring in Virgo [20].

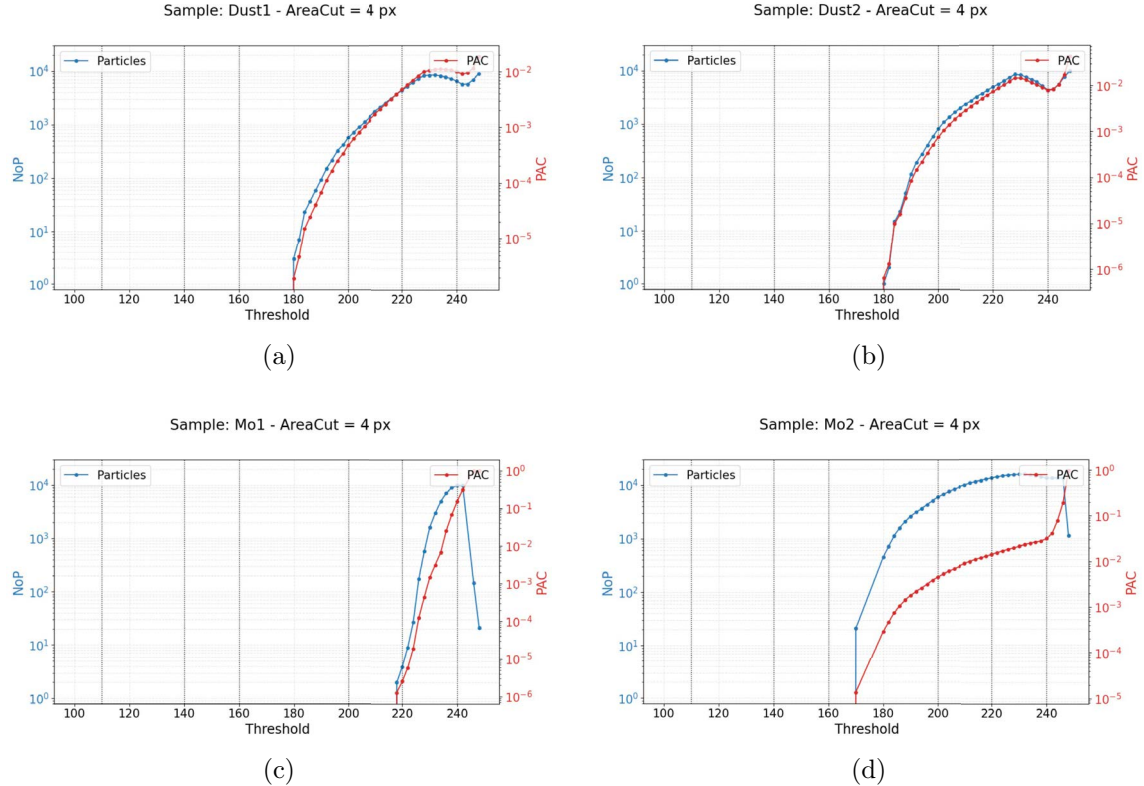


Figure 6.10: NoP and PAC vs luminosity threshold for the background of 4 different samples analyzed in the laser cleaning test.

6.6 Particles' diameter distributions

As a first analysis we study the numerical distributions of the detected particles versus their size, comparing pictures of the same area before and after the DLC treatment. The chosen binning is based on the quantization induced by the pixels, and the bins are equally spaced. In particular, the diameter error ΔD for a particle is ± 2 px, which corresponds to $4.18 \mu\text{m}$. The bin width is $\Delta b = 2 \cdot \Delta D = 4$ px = $8.36 \mu\text{m}$. This ensures that each bin covers an interval equal to the total uncertainty of the measurement.

The results for the two samples treated with one laser setting and the dust sample treated with N₂ flux are shown in Fig. 6.12, 6.13 and 6.14. Fig. 6.11 presents a zoom of one spot (number 410 of the dust sample treated with N₂ flux, 6.14) for reference, showing the values adopted for the X and Y axes in all the histograms in the grids. Fig. 6.12 for Mo shows a pre-treatment distribution consistent with what is expected from the diameter percentiles characteristic of this type of dust (see Sect. 5.2). In addition, the distribution of the particles on spots at the low EDs ($<400 \text{ mJ/cm}^2$) is not modified by the laser processing, except in a few cases (spot 32, 42, 33 and 43) where an excess of larger particles is visible after the cleaning. These specific photos show an accumulation of Mo particles

in the center of the spots (see Fig. 6.5). This could cause the software to identify two closely positioned particles as one, which could explain the increase in the number of larger particles after the DLC procedure. This phenomenon is not visible in other treated Mo samples. For higher EDs, the cleaning procedure has an effect: the distribution changes after the DLC and the counts are typically lower in the histograms of the post-treatment images, indicating a decrease in the number of particles.

The dust samples (6.13 and 6.14) show a pre-cleaning distribution (blue line in the histograms) that, as expected, decreases with increasing size. The counts of the lowest bin (corresponding to a diameter range of [1.9, 6.3] μm) increase after the laser processing at high EDs, while the counts of the last bins (corresponding to larger particles) decrease or vanish. This suggests that, with these laser parameters, the cleaning procedure may be effective for larger particles, but not for smaller ones.

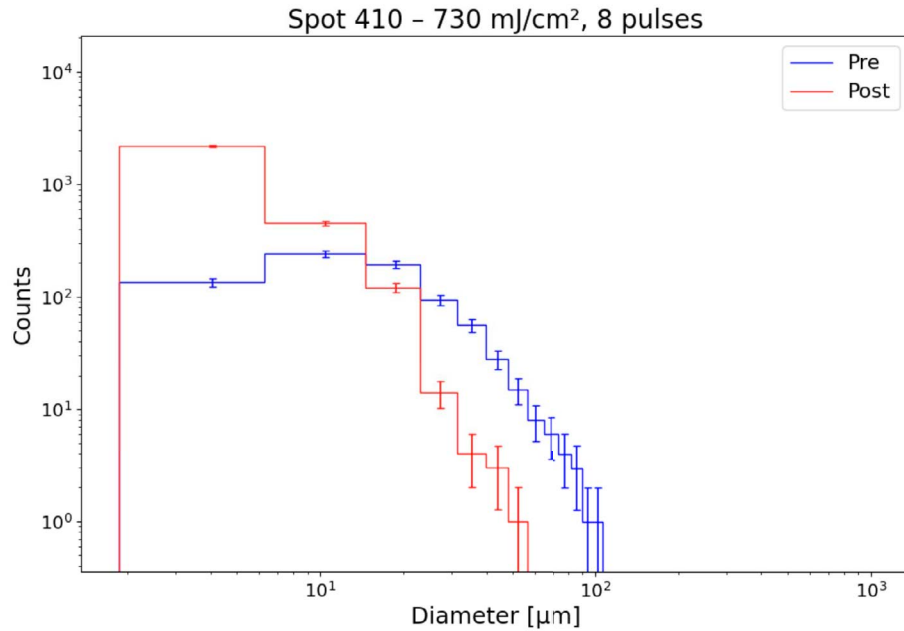


Figure 6.11: Pre (blue line) and post (red line) histograms of the spot treated at 730 mJ/cm^2 , with 8 pulses on the environmental dust sample treated with N_2 flux. Here a zoom of the plot on the bottom right of the grid in Fig. 6.14 is shown for reference.

Diameter distribution histogram - Mo sample, 1 settings - thr 160

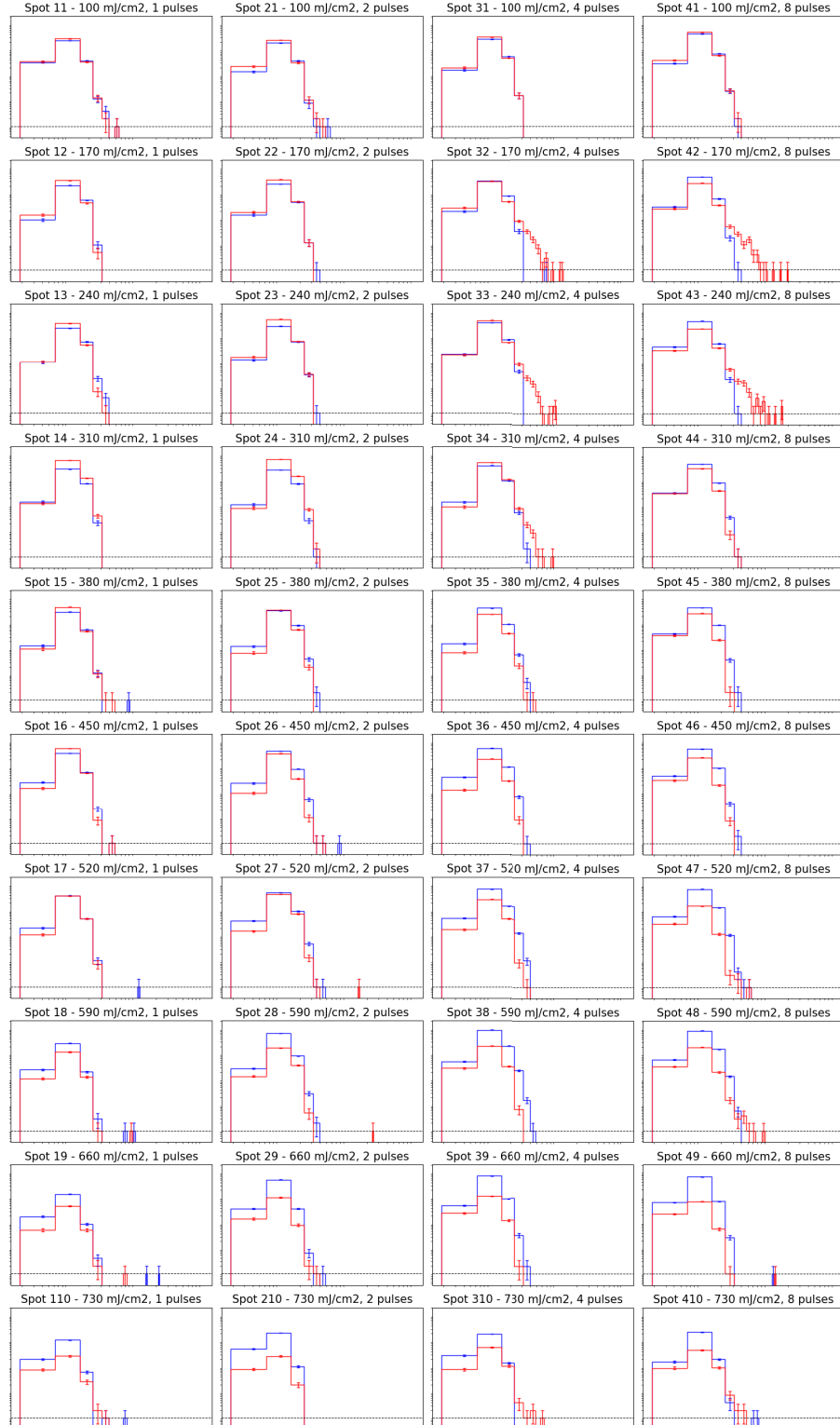


Figure 6.12: Histograms of the size distribution for the Mo sample treated with 1 laser setting. The ED increases from top to bottom, the number of pulses increases from left to right. The distribution pre cleaning is shown in blue, post cleaning in red. The dashed horizontal line corresponds to counts = 1.

Diameter distribution histogram - dust sample, 1 settings - thr 160

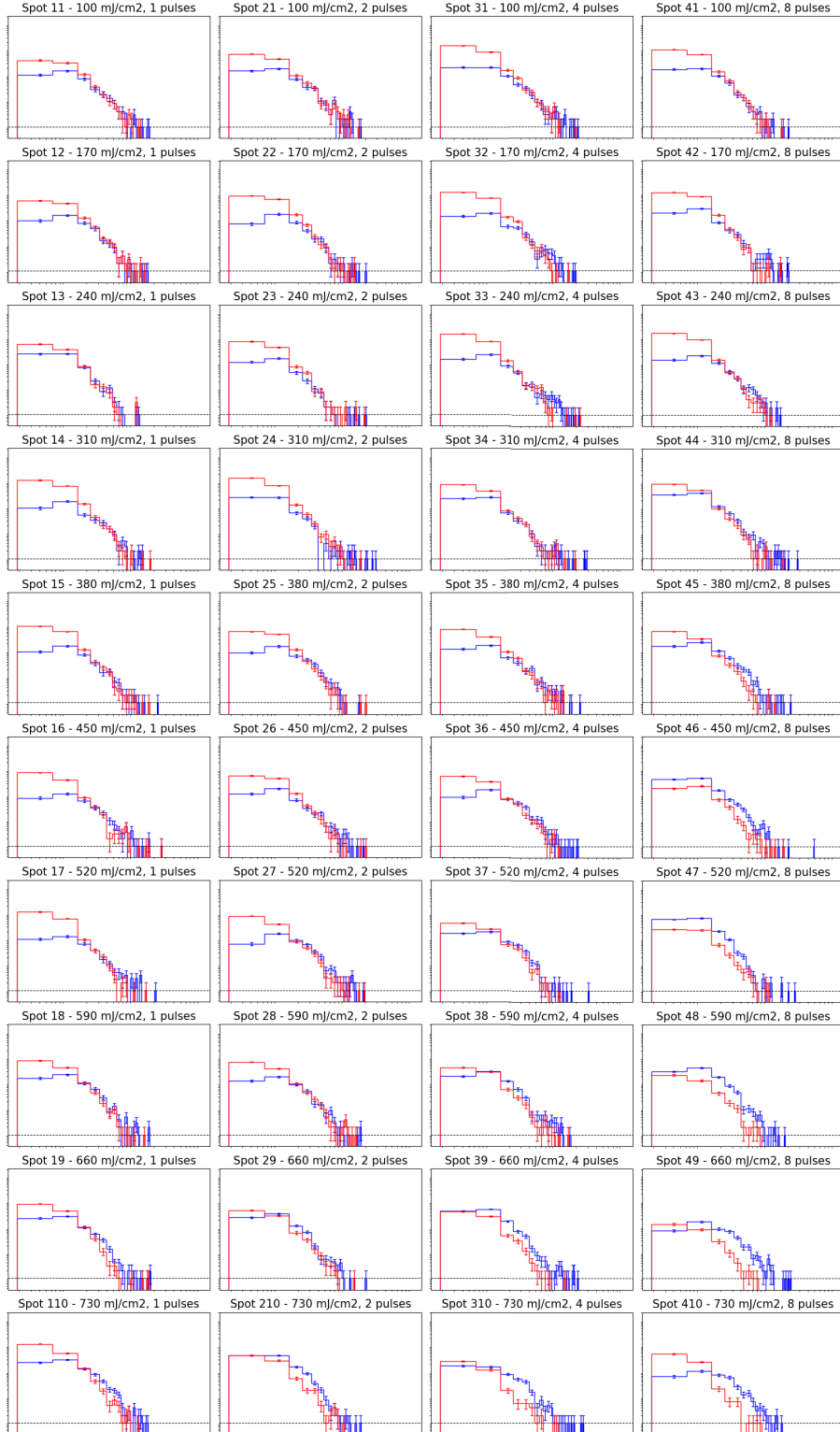


Figure 6.13: Histograms of the size distribution for the dust sample treated with 1 laser setting. The ED increases from top to bottom, the number of pulses increases from left to right. The distribution pre cleaning is shown in blue, post cleaning in red. The dashed horizontal line corresponds to counts = 1.

Diameter distribution histogram - dust flux sample, 1 settings - thr 160

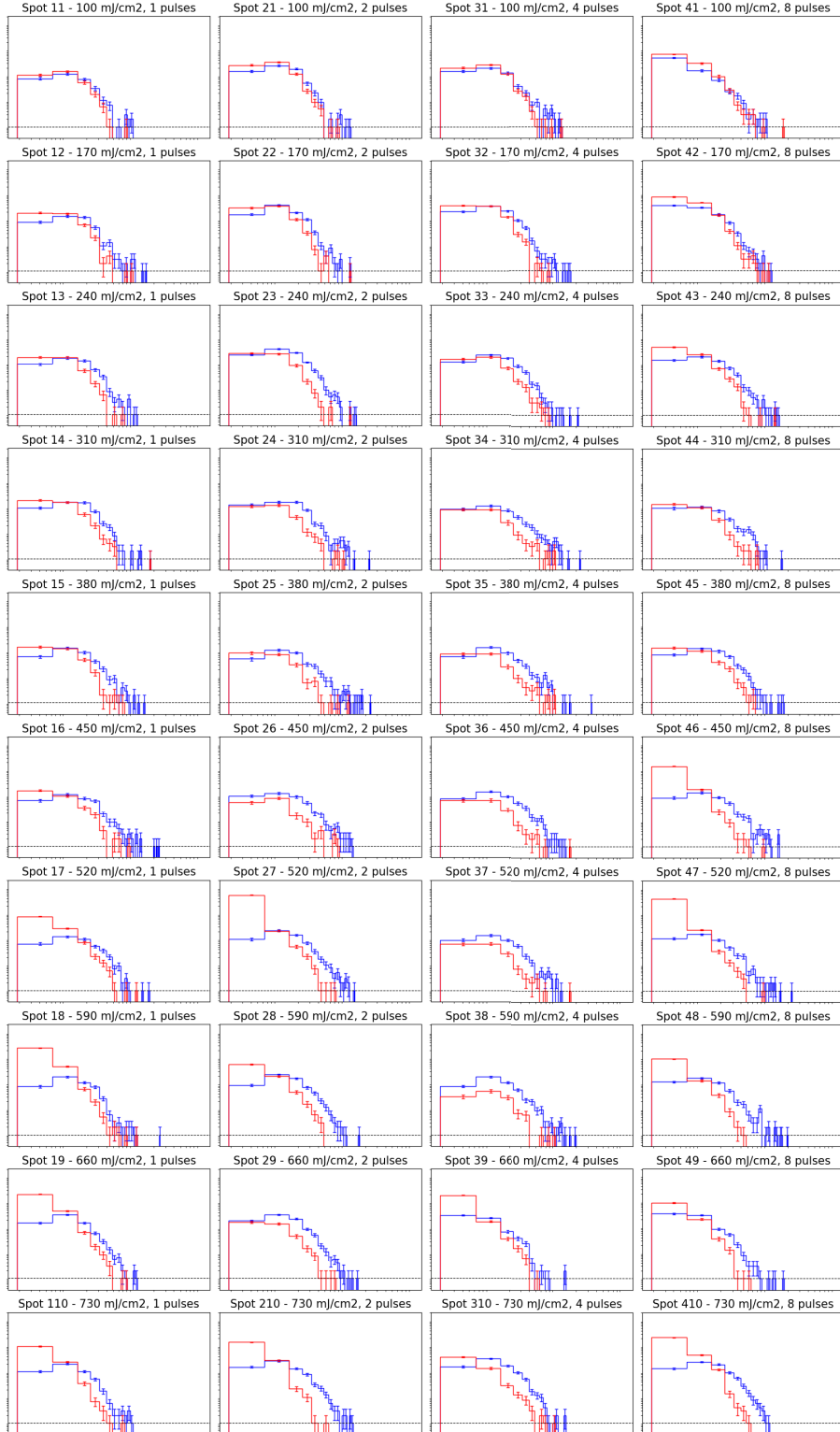


Figure 6.14: Histograms of the size distribution for the dust sample treated with 1 laser setting and N₂ flux. The ED increases from top to bottom, the number of pulses increases from left to right. The distribution pre cleaning is shown in blue, post cleaning in red. The dashed horizontal line corresponds to counts = 1.

6.7 Comparison of PAC and NoP before and after processing

Our main methods to quantify the efficiency of the DLC process are: to measure the ratio of the NoP (post/pre DLC), and to measure the ratio of the PAC (post/pre DLC) in the area subject to the laser cleaning.

At a $\times 50$ magnification, the FoV matches well the area covered by the laser spot, since only a small percentage ($\sim 9.7\%$) of the processed area is not included in the photos (as already mentioned in Sect. 6.1).

As the cleaning efficiency is expected to depend on the energy density and the number of pulses, the results are shown as a function of these two quantities.

Fig. 6.15, 6.16 and 6.17 show the PAC and NoP ratio post/pre cleaning for the different treated samples. Generally, the PAC and NoP ratios decrease as a function of the ED. This effect is particularly evident for the Mo sample treated with 1 laser setting compared to that treated with 2 laser settings (Fig. 6.15). For the dust samples, the different laser settings used show a similar behavior of the PAC and NoP ratios (Fig. 6.16). In general, 8 pulses seem to be more efficient, while the other pulse numbers all lead to similar results. Especially for the dust samples (with and without N_2 flux, Fig. 6.16 and 6.17), the NoP ratio is much more affected by fluctuations with respect to the PAC ratio, reaching values greater than 1.

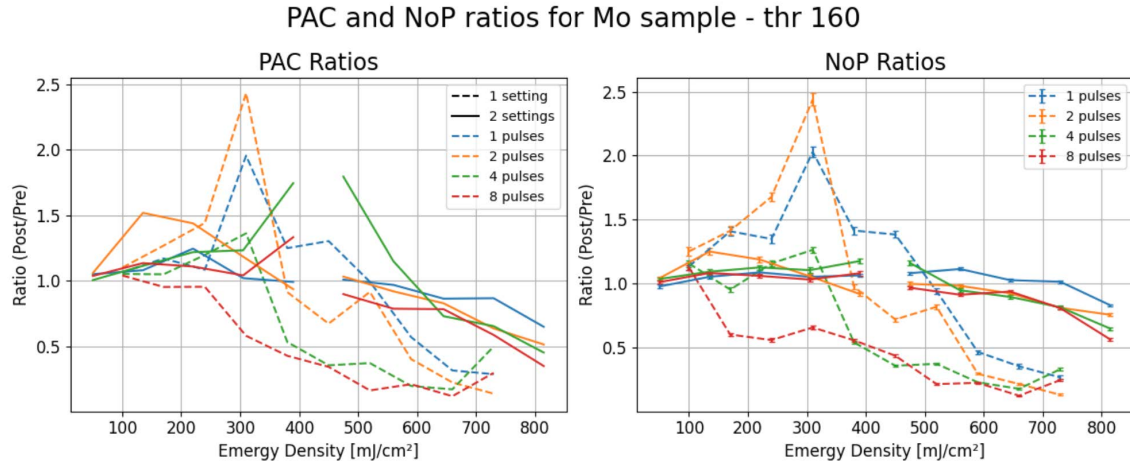


Figure 6.15: PAC and NoP ratio (post/pre cleaning) for the Mo samples treated with 1 and 2 laser settings (dashed and solid lines) vs the ED in mJ/cm^2 . The different colors correspond to different numbers of pulses.

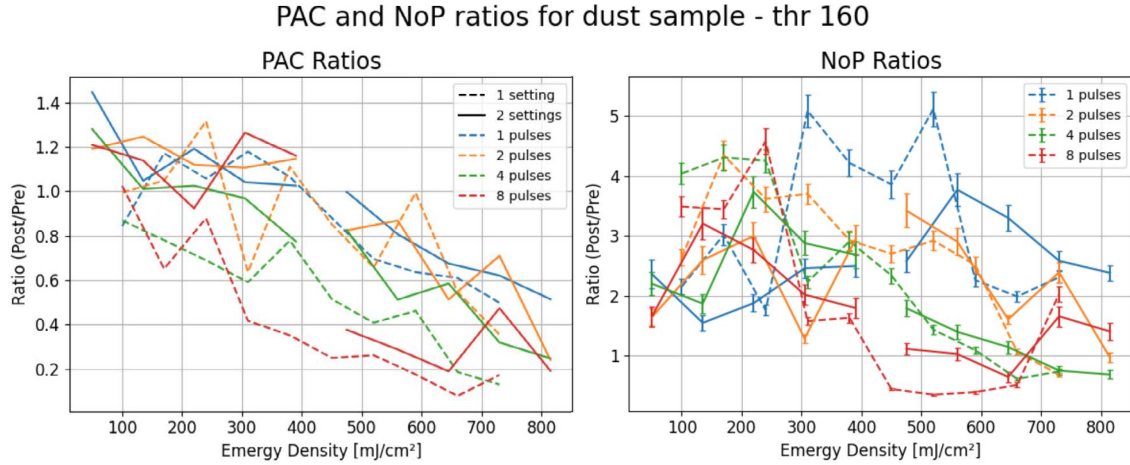


Figure 6.16: PAC and NoP ratio (post/pre cleaning) for the dust samples treated with 1 and 2 laser settings (dashed and solid lines) vs the ED in mJ/cm^2 . The different colors correspond to different numbers of pulses.

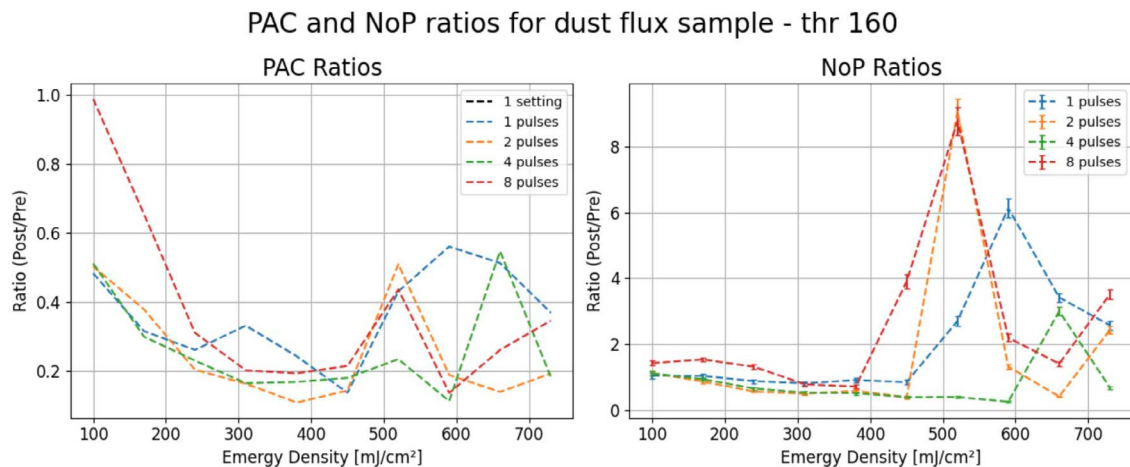


Figure 6.17: PAC and NoP ratio (post/pre cleaning) for the dust sample treated with 1 laser setting and 8 L/min N_2 flux vs the ED in mJ/cm^2 . The different colors correspond to different numbers of pulses.

6.8 Cleaning efficiency for a fixed diameter range

Because of the large fluctuation shown in Fig. 6.16 and 6.17, we decide to analyze separately the effect of the technique on particles of different sizes. We plot for each diameter range (the bins in the histograms) the NoP ratio as a function of the ED for the 4 applied pulse numbers. This analysis was performed for the first 6 diameter bins. The results for the two samples treated with no flux, one laser setting and the dust sample treated with N₂ flux are shown in Fig. 6.18, 6.19 and 6.20.

As discussed in Sect. 5.2, the Mo particles have known diameter percentiles, with the 90th percentile being 24.1 μm . This means that, when viewing the plots in Fig. 6.18, only the first 4 plots can be considered statistically relevant, and any particles detected at larger diameters are due to other types of dust contamination. The plots in Fig. 6.18 show a decrease in the NoP ratio with increasing ED, indicating the efficacy of the DLC treatment. For the more significant bins (between 6 and 23 μm), a marginal effect of the pulse repetition is evident, with the lower ratios corresponding to the larger number of pulses.

The two dust sample plots, Fig. 6.19 and 6.20, show that for the diameter range [1.9, 6.3] μm (first plot on the top left) the ratio reaches values > 1 , indicating an increase in the counts for that size after the DLC. For particles with a diameter $> 14.6 \mu\text{m}$ the laser cleaning becomes more effective: the ratios are typically < 1 and decrease with increasing ED and repetition number. This behavior is expected if the laser cleaning procedure works, meaning that the technique can be considered efficient for particles larger than a certain size. The process might also be effective for smaller particles, but we cannot affirm this with these analysis, as a cleaning effect for smaller diameters is not be evident because of the appearance of small particles on the dust samples for high EDs, discussed in the following section.

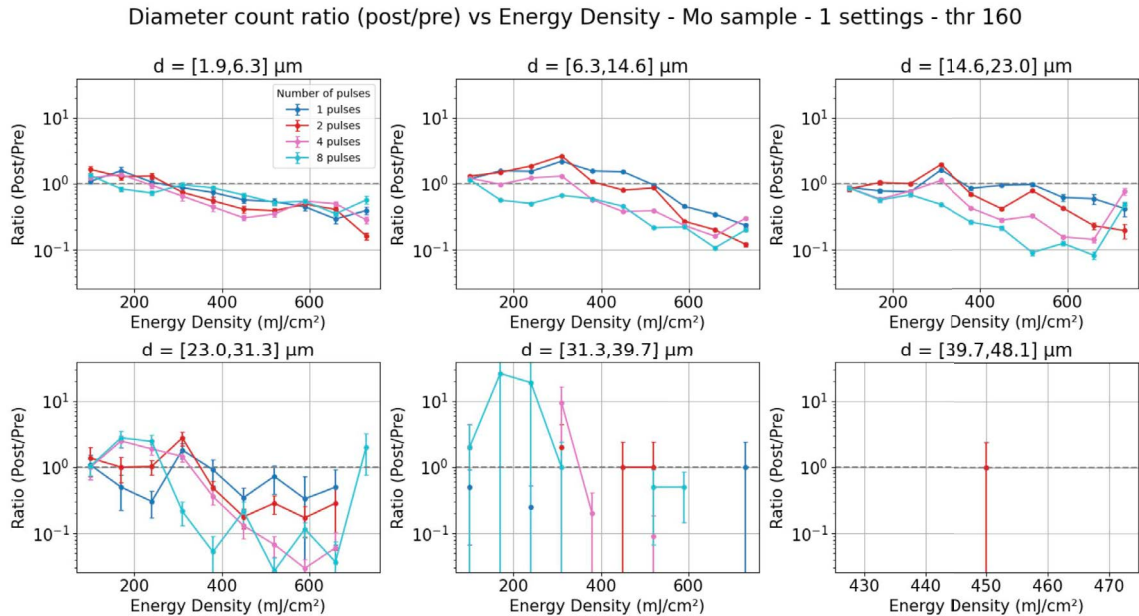


Figure 6.18: NoP ratio versus the ED for different diameter ranges, for the Mo sample treated with 1 laser setting. Different colors correspond to different numbers of pulses.

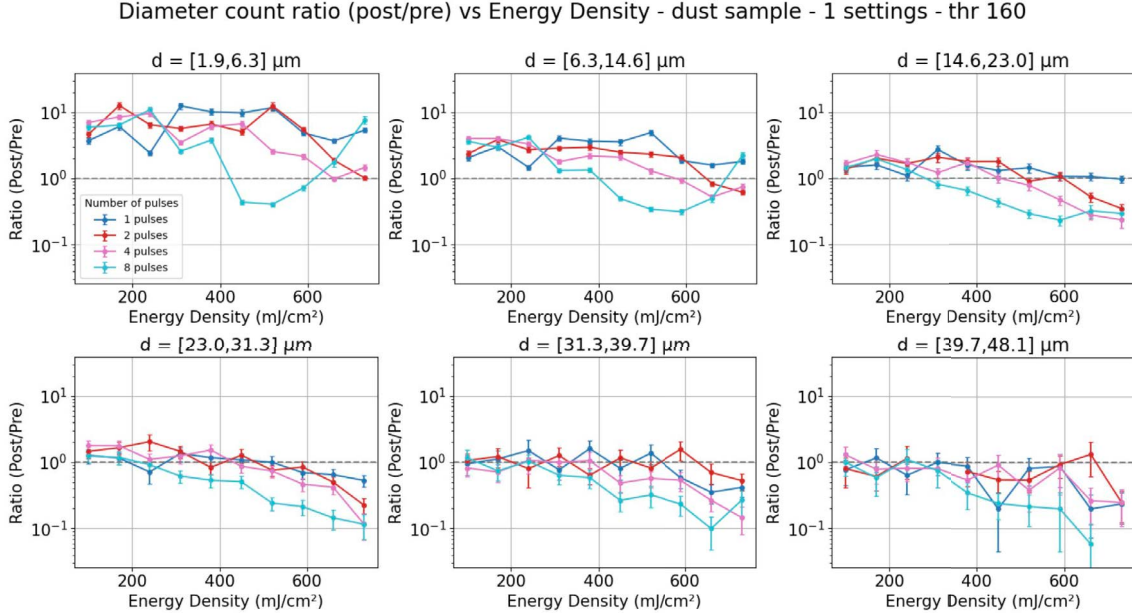


Figure 6.19: NoP ratio versus the ED for different diameter ranges, for the dust sample treated with 1 laser setting. Different colors correspond to different numbers of pulses.

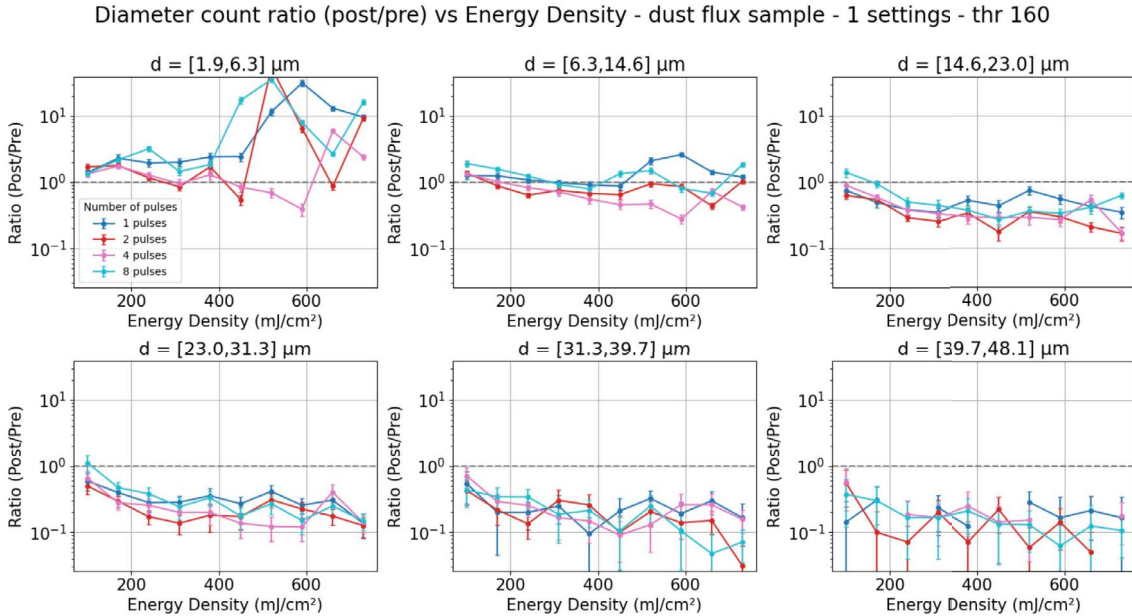


Figure 6.20: NoP ratio versus the ED for different diameter ranges, for the dust sample treated with 1 laser setting and N_2 flux. Different colors correspond to different numbers of pulses.

6.9 Study of the small particles

The size distribution histograms (discussed in Sect. 6.6) and the PAC and NoP ratio (Sect. 6.7 and 6.8) highlight an excess of small particles after the DLC procedure on the dust samples. This effect is visible for high EDs ($\gtrsim 400 \text{ mJ/cm}^2$), and it is more evident in the sample treated with N_2 flux. Fig. 6.21a shows the spot treated at 730 mJ/cm^2 and

8 pulses for the dust sample treated with N₂ flux. Some small, rounded particles forming a pattern defined by cracks in the glass substrate (indicating damage resulting from high absorption) are visible on this spot, along with some larger particles. These particles are uniformly distributed in the areas in which they appear. Most of them have a diameter of $\sim 1\mu\text{m}$, with some larger particles reaching $\sim 4 - 5\mu\text{m}$ (see Fig. 6.21b), and they all look more circular and symmetric than regular environmental dust. This last aspect is discussed in Sect. 6.9.1, where a circularity analysis is presented. Analysis of the small particles using tilted light on the microscope (Fig. 6.21c) shows that they are elevated with respect to the substrate. Attempting profilometry with the microscope was unsuccessful, indicating that these particles have a height $z < 1\mu\text{m}$. The presence of the small rounded particles on the dust samples could either indicate a fragmentation of larger particles into smaller ones, or could be a consequence of substrate damage.

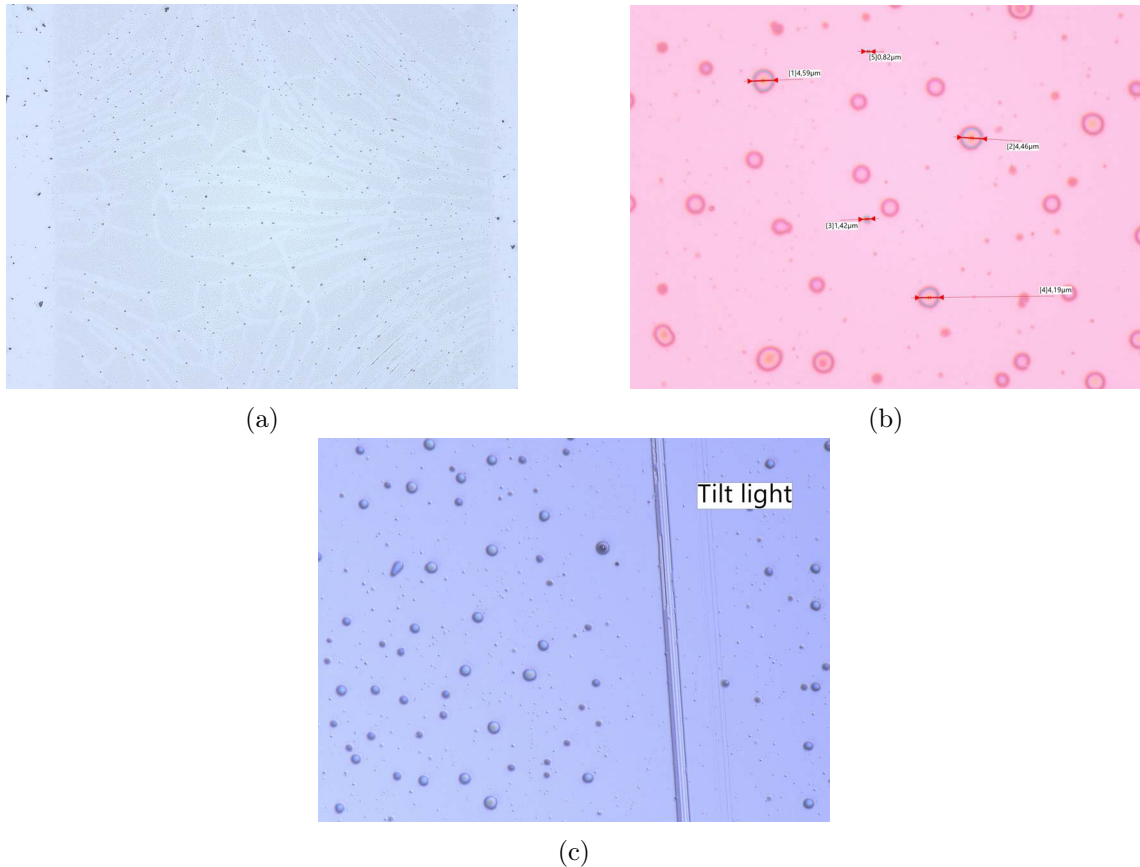


Figure 6.21: Small rounded particles on the spot on the dust sample treated with N₂ flux at 730 mJ/cm^2 , 8 pulses (a): acquired photo used for the analysis (b): size measurement of the small particles (the reported values are: 0.82, 4.59, 4.46, 1.42 and 4.19 μm) (c): photo taken with light from an inclined source with respect to the sample normal that shows the shadows of the small particles on the substrate. Photo size is $4514.4\mu\text{m} \times 6019.2\mu\text{m}$ at x50 (image a), $151.2\mu\text{m} \times 201.6\mu\text{m}$ at x1500 (image c) and $86.4\mu\text{m} \times 115.2\mu\text{m}$ at x2500 (image b).

6.9.1 Circularity

This section presents a study of the circularity of the appeared small particles on the dust samples. Circularity describes how far from a perfect circle is the projected area of the

particle. Let us first present some definitions provided by the Keyence manual [44] to characterize digital images:

- Perimeter: it is the length of the closed line that passes through the center of the outer pixels of the identified particle.
- Area: the number of pixels that compose the image
- Circularity: if A is the area of the figure in px^2 , meaning the number of pixels in the figure (or in μm^2), and P is the perimeter in px (or in μm), the circularity is $C = (4\pi A)/P^2$.
- Minimum diameter: the minimum possible distance between two parallel lines on either side of the particle.
- Maximum diameter: the maximum distance between any two pixels on the perimeter of the particle.

The circularity just defined becomes significant only for particles made of a large number of pixels. Let us consider the extreme case of a particle composed of two pixels, placed one next to the other with one side in common. For this configuration, the perimeter is equal to 2 px, since to close the contour line of the figure the software counts twice the segment that connects the two pixel centers. The area is equal to 2 px^2 , since they are two pixels. Therefore, $C = (8\pi)/4 = 2\pi$, this is a value > 1 that does not have any meaning when compared to the circularity of other larger particles. Other better estimates of circularity could be found using the definition of geometric moments [46], but this requires knowledge of the centers of all the pixels that compose the picture, which is not accessible from the microscope output. An alternative definition of circularity can be considered, which consists of the ratio of the minimum diameter over the maximum diameter ($\text{Min D} / \text{Max D}$), both displayed in the output file. In this way, we ensure that, for a particle closer to a circle, this quantity approaches 1, and for any other shape it is always < 1 .

By visual inspection, the small particles that appeared on the dust samples at high EDs (visible in Fig. 6.21) appear to be all pretty rounded. To verify this hypothesis and be able to discern these particles, we study the circularity of the particles and if and how it changes with the DLC process. We quantify the circularity as the ratio of the minimum to the maximum diameter ($\text{Min D} / \text{Max D}$), as previously discussed, for each particle. Fig. 6.23 shows a grid with histograms (normalized by the counts and the bin width) of the circularity for the spots in the dust sample treated with N_2 flux. Fig. 6.22 presents a zoom of one spot (number 410) for reference, showing the values adopted for the X and Y axes in all the histograms in the grids. The spots treated at higher EDs, that presented the appearance of the small particles, show no evidence of an increase of counts at higher circularity. Conversely, the counts at lower circularity decrease. The first few bins, corresponding to more elongated fiber-like particles, have zero counts in the post cleaning histograms, resulting in a less spread distribution over the circularity range. The scatter plot of the circularity of the particles versus their size (here the equivalent diameter is shown, calculated as $d_{eq} = 2\sqrt{A/\pi}$, where A is the area in μm^2) does not show a significant change in the circularity distribution after the DLC procedure (see Fig. 6.24). Thus, we do not confirm the hypothesis that the small particles have a higher circularity, hence we cannot use this quantity to identify and distinguish them among the usual environmental dust.

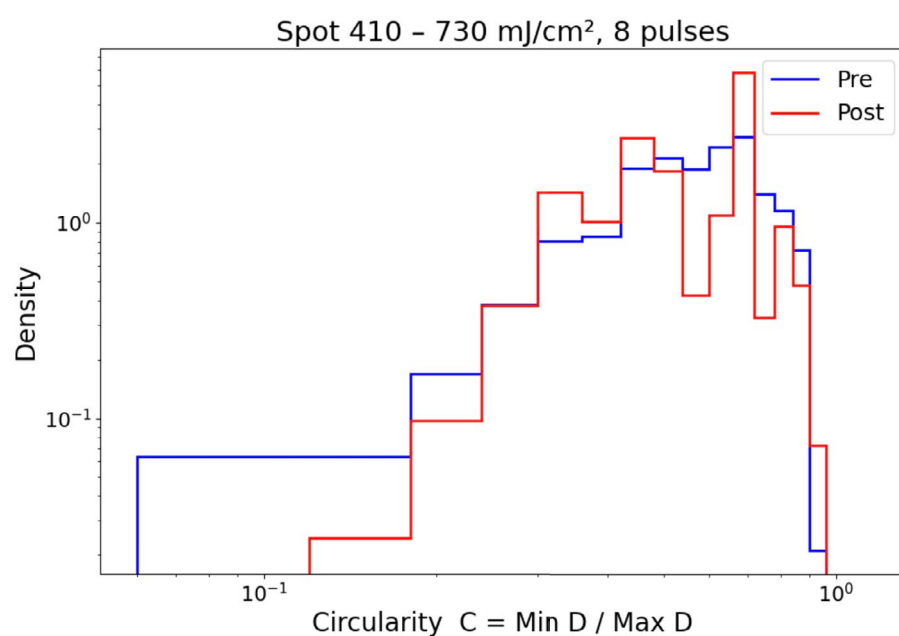


Figure 6.22: Pre (blue line) and post (red line) histograms of the spot treated at 730 mJ/cm², with 8 pulses on the environmental dust sample treated with N₂ flux. Here a zoom of the plot on the bottom right of the grid in Fig. 6.23 is shown for reference.

C = Min D / Max D Histograms - dust flux sample, 1 settings - thr 160

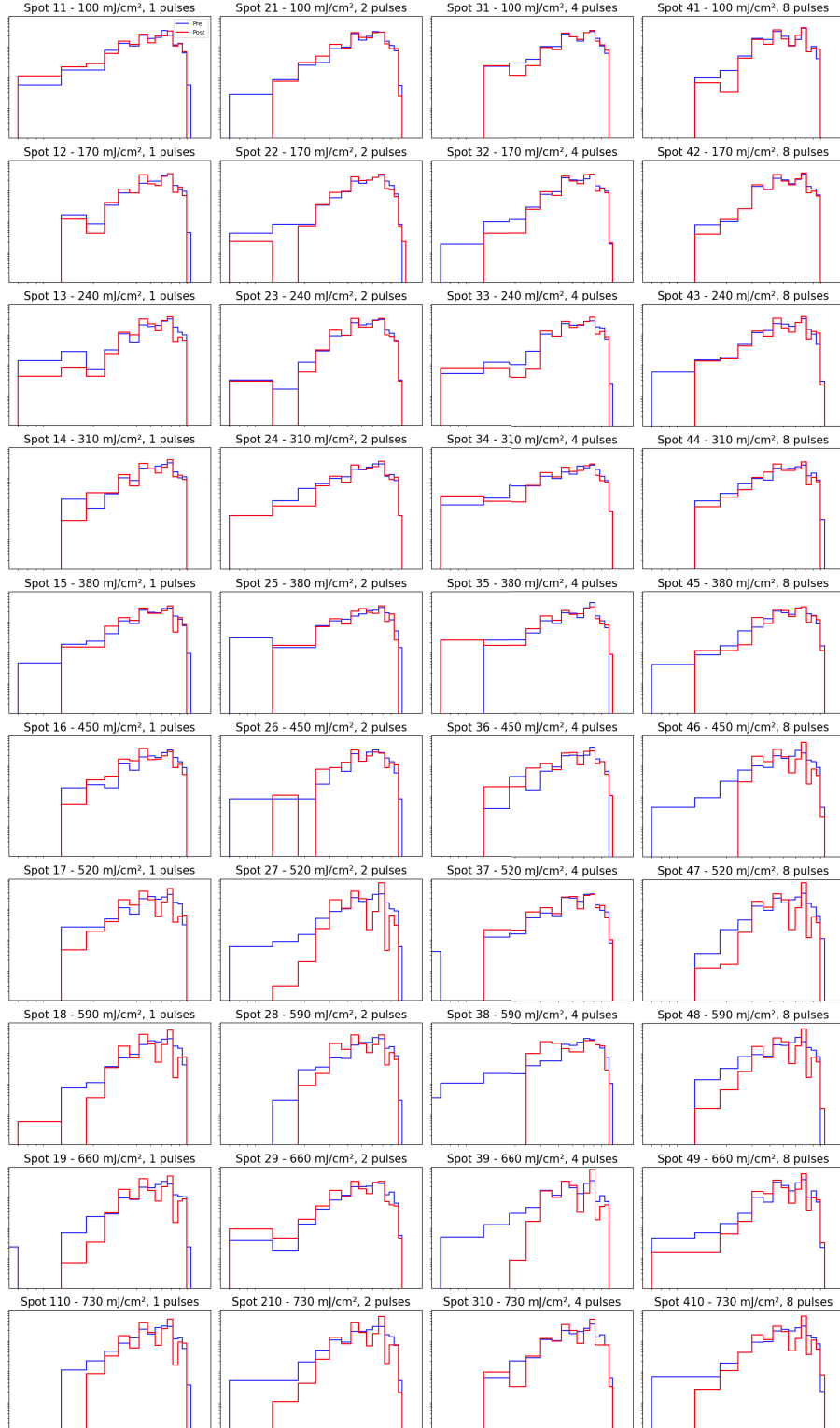


Figure 6.23: Normalized histograms of the circularity for the dust sample treated with 1 laser setting and N₂ flux. The ED increases from top to bottom, the number of pulses increases from left to right. The distribution pre cleaning is shown in blue, post cleaning in red.

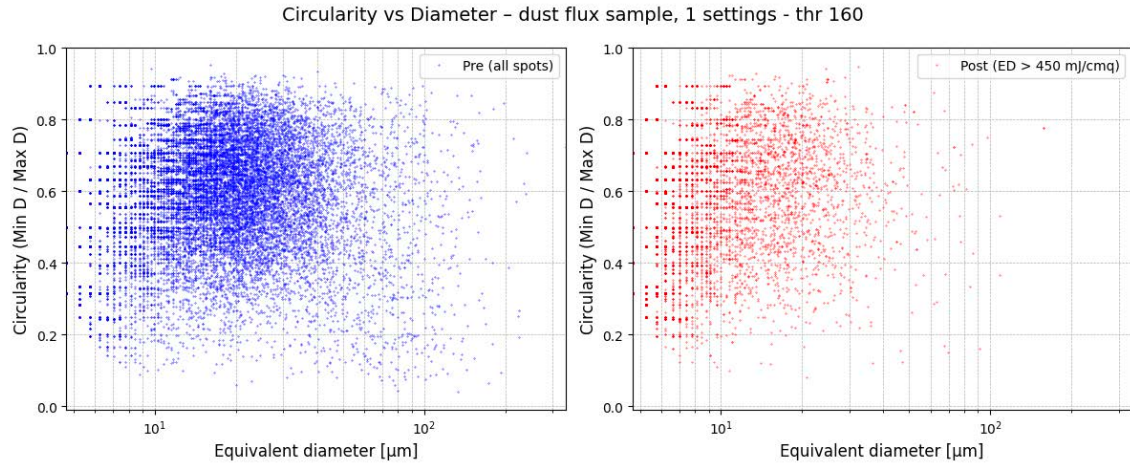


Figure 6.24: Scatter plot of the circularity versus the equivalent diameter before (on the left) and after (on the right) the DLC. The plot for the pre cleaning include all the spots, while for the post cleaning only the spots with $ED > 450 \text{ mJ/cm}^2$ are shown, since we want to isolate a possible effect of the small appeared bubble-like particles on the circularity, and these particles are visible only for higher EDs.

6.9.2 Raman spectroscopy on the smaller particles

To determine the composition of the small rounded particles and try to establish whether their appearance was due to substrate damage or dust fragments, a Raman spectroscopy inspection was conducted.

Raman spectroscopy is an experimental technique that uses the interaction of a light (in the visible or near-infrared wavelength range) with a material's chemical bonds to investigate its vibrational properties. It provides a fingerprint of the material of interest by reconstructing the spectrum of inelastic scattered light. Inelastic scattering processes are referred to as anti-Stokes or Stokes scattering, depending on whether the energy of the emitted photon is higher or lower than that of the incident photon. Raman emission therefore corresponds to those scattering events in which part of the photon energy is exchanged with a vibrational mode of the material, producing a shift in frequency that directly reflects the underlying vibrational states. A Raman spectrum represents the intensity of the emission as a function of this frequency shift.

When a Raman test is performed, most of the scattering process is elastic and is referred to as Rayleigh scattering, which is 10^{10} times more frequent than inelastic phenomena [47]. Additionally, there are other inelastic spectroscopic phenomena that compete with Raman emission. One example is fluorescence, which is a type of photoluminescence with lifetime shorter than 10^{-5} s. Unlike Raman scattering (an instantaneous process that does not involve real electronic excitations), fluorescence requires the absorption of a photon into an electronic excited state and the subsequent radiative de-excitation. This produces an emitted spectrum that is typically way more intense than Raman. When analyzing the spectra, it is necessary to consider these unwanted contributions and subtract them to isolate the Raman peaks. The elastic Rayleigh contribution appears as an exponential tail for small wavenumbers, while fluorescence causes a linear background increase at higher Raman shifts. Fig. 6.25 shows the possible processes during a Raman test.

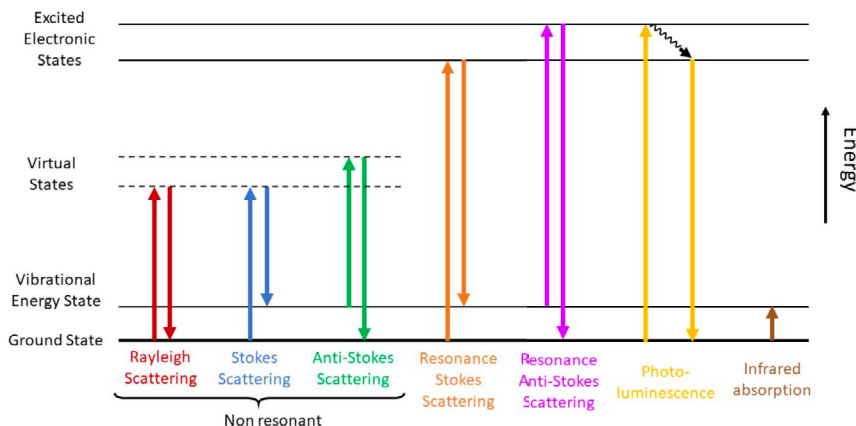


Figure 6.25: Scheme of the possible phenomena during a Raman experiment. Stokes and anti-Stokes scattering are the Raman processes. Figure from [47].

For this study, the Raman spectra are obtained with a Horiba XploRA Plus scatterometer [48], with a probing laser at 532 nm. We focused on a specific area of the Dust3 sample that had been treated with N₂ flux. This area clearly showed the small particles in excess after the laser treatment, with both dust particles and small, rounded particles visible. We collected the Raman spectra of the soda-lime glass substrate, two dust particles and one "bubble". For each spectrum, the background was fitted with a sum of two contributions

(one exponential representing Rayleigh scattering and one linear for fluorescence) at lower and higher wavenumbers, so that it could be subtracted. An example of this process is shown in Fig. 6.26.

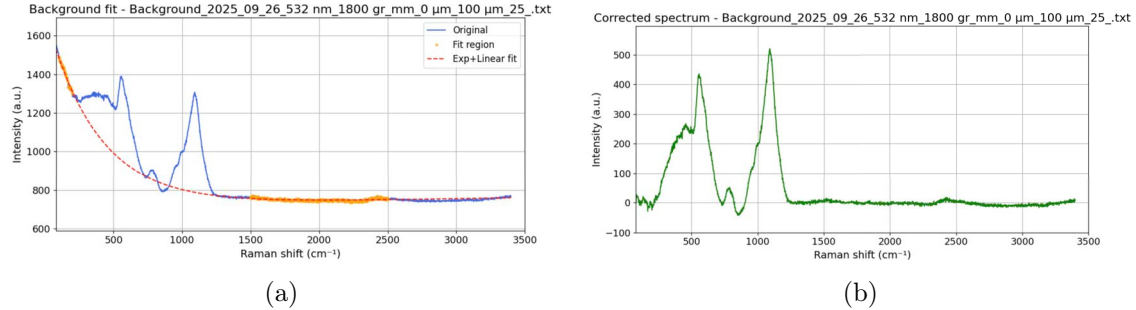


Figure 6.26: Soda-lime glass Raman spectrum. (a): raw obtained data (solid blue line) with the points used for the background fit (the yellow points) and the derived fit function to subtract (the dashed red line). (b): corrected spectrum (the exponential fitted function subtracted from the raw data).

Having characterized the Raman peaks for the substrate background and for dust particles, we compared them with the rounded particle's spectrum to determine whether it had the same peaks as the dust particle or the substrate, or if it exhibited different features. All three spectra are shown together in Fig. 6.27.

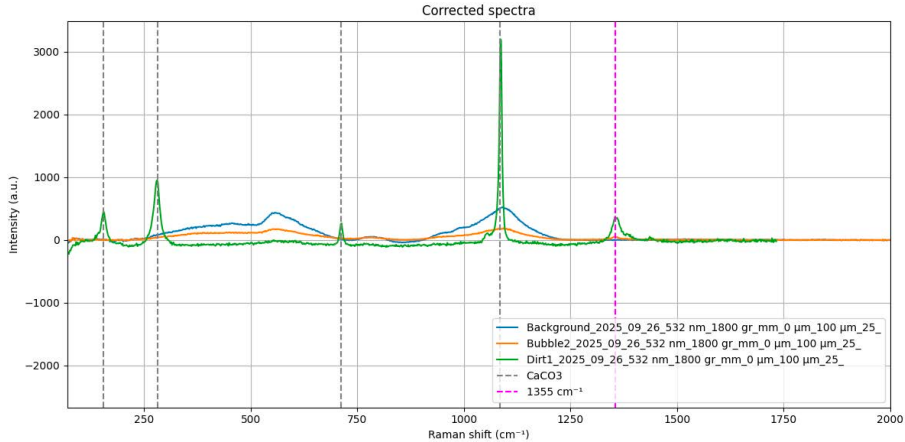


Figure 6.27: Corrected Raman spectra (with the subtraction of the exponential and linear background) for the soda-lime glass substrate (solid blue line), a dust particle (solid green line) and a small, rounded particle (solid orange line). The vertical gray dashed lines indicate the peak location of the CaCO₃ spectrum, while the vertical pink dashed line is an additional peak that is visible on both the dust particle spectrum and the small particle spectrum.

By comparing the results with spectra of known materials, the dust spectrum matches the values corresponding to calcite (CaCO₃), which are highlighted in Fig. 6.27 by the gray vertical dashed lines. An additional peak appears at a wavenumber of around 1355 cm⁻¹, which indicates the presence of another material. The rounded particle's spectrum matches the soda-lime glass substrate profile, and in addition presents a weaker peak at ~ 1355 cm⁻¹ that corresponds to that of the dust spectrum. Other characteristic peaks of the dust particle, like the one at ~ 258 cm⁻¹, are not visible in the rounded particle's

spectrum. On the basis of these results, it is not possible to state with certainty that the small spherical particles are solely dust, nor can they be unambiguously attributed to damage of the substrate.

Chapter 7

Conclusion

Dust particles present in the environments of a gravitational-wave (GW) interferometer like Virgo can be harmful to the detection of signals, since they can cause stray light, which gives a noise contribution in the low-frequency region. Micron-level dust particles are unavoidable, even in clean, in-vacuum spaces in which the detectors are placed, and they can either fall through the laser beam, or deposit on optical components, especially the test masses.

The goal of this thesis was to conduct an exploratory study of a contactless cleaning technique, Dry Laser Cleaning (DLC), applied to glass substrates for a future possible application to GW interferometers. First, we gave an estimate of the adhesion forces for micron and sub-micron dust particles on a substrate, and numerically simulated some physical processes involved during laser cleaning.

We then conducted some exploratory DLC tests for two types of dust particles deposited on microscope slides. Soda-lime glass microscope slides were used, and two types of dust particles were analyzed: molybdenum particles with a diameter $d \sim 15 \mu\text{m}$ and environmental dust particles. Molybdenum was used to test the technique on particles of known size and composition, while environmental dust is likely more similar to the one that could be found in the real detector environments. We used a KrF excimer laser at a wavelength of 248 nm and with a pulse duration of 22 ns. At this wavelength the absorption is mostly confined to the surface layer of the substrate, limiting bulk heating. Furthermore, given that the pulse duration is relatively long compared to the timescales of electronic excitation and relaxation, the deposited energy is largely thermalized during the pulse. Consequently, thermal removal mechanisms at the dust - substrate interface are expected to dominate. Soda-lime glass strongly absorbs at the wavelength of interest, and this affected the process, causing the substrate to change color (confined to the laser spot) and cracks to form at higher energy densities. An environmental dust sample was also processed under the influence of a constant N_2 flux of 8 liters/min.

With a digital microscope, we imaged the samples before and after the DLC to study the effectiveness of this technique. The luminosity threshold, which needs to be preset for the particle identification analysis, appears to vary within a considerable range because of the roughness of the substrates, even within identical samples from the same batch. Thus, for the soda-lime glass substrate, the optimal luminosity threshold should be adjusted for each sample. As a compromise, a threshold value $T = 160$ has been found to be the most conservative for the samples processed in the DLC test.

Analysis of the particles' size distribution and the comparison of the Percentage of Area Covered (PAC) and Number of Particles (NoP) before and after the cleaning process (Sect. 6.7) showed a general increase in the DLC process' efficiency with increasing energy

density (ED), and with 8 pulses. The environmental dust samples treated at high EDs ($\gtrsim 400 \text{ mJ/cm}^2$) revealed unexpected behavior, particularly the one treated with the N_2 flux. While larger particles seem to be removed by the DLC, some new, small (diameter $d \lesssim 5 \mu\text{m}$) particles appeared uniformly on the areas where the laser impinges. We conducted further analysis to determine the origin of this phenomenon, for example if it is due to substrate damage or if fragments of dust particles had redeposited on the substrate. Analysis of the NoP ratio for each diameter range (Sect. 6.8) showed effectiveness of the DLC technique on environmental dust samples for particles with a diameter $d \gtrsim 15 \mu\text{m}$: for these particles, the NoP ratio (post/pre DLC) decreases with increasing ED, reaching a minimum value of ~ 0.1 , as shown in Fig. 6.19. The Mo sample shows a similar trend also for the smaller diameters: for particles in the range $[1.9, 6.3] \mu\text{m}$, the ratio of the NoP post/pre the DLC treatment below 1 (indicating effective cleaning) for $\text{ED} \gtrsim 300 \text{ mJ/cm}^2$ (as shown in Fig. 6.18). To characterize the new particles appearing after the DLC on soda-lime glass substrates with environmental dust, we analyzed the circularity of the particles before and after the cleaning procedure. This analysis revealed no evident change in the particles' circularity, hence circularity is not a parameter that can be used to distinguish the new small particles from the regular environmental dust. As a result of the circularity and Raman study, we cannot identify the new particles nor determine their origin. These studies are inconclusive: in case they continue to appear in future research, after some planned improvements in the setup, they will need to be investigated more in depth.

7.1 Future perspectives

Many improvements can be made to produce a more complete theoretical model and to conduct more specific tests.

Firstly, the approximated model described in Sect. 4.5 can be made more accurate by modeling electrostatic and photo-chemical effects, which are expected to be more important for shorter pulse durations, and also by considering the effect of many particles on the substrate.

A next step in this work will be the experimental measurement of the adhesion force, discussed in Sect. 4.1. For this purpose, an experimental test is already planned.

Other DLC tests can be conducted using pure fused silica substrates, which would minimize the substrate effect thanks to its low absorption. This would also help us to clarify the appearance of the new, small particles in the dust samples at high EDs. Ideally, they would not show up with fused silica substrate: if they do appear again, then they will need to be investigated in more detail. In addition, other dust types of known composition can be tested.

Another improvement would be to apply the DLC with the sample reversed, so that the cleaned particles can fall off by gravity, and not redeposit on the substrate. Additionally, the DLC process should be conducted under vacuum to avoid any effect of the atmosphere: this would allow to test the effectiveness of the technique in a situation similar to the environment of the suspended mirrors of a GW interferometer. Finally, the DLC effect should be investigated on a fused silica substrate with coating, either anti-reflection (AR) or high reflection (HR).

Appendix A

Setup photos

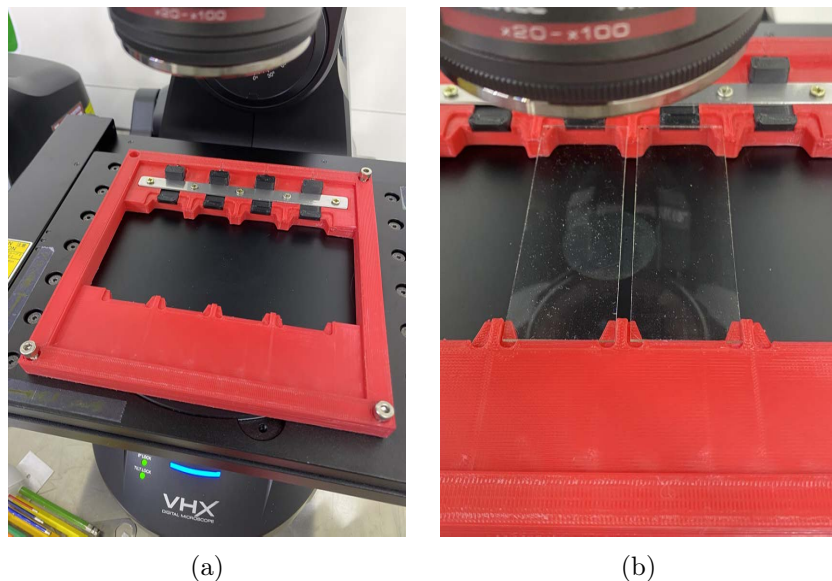


Figure A.1: Holder used for the photo acquisition of the soda-lime glass samples.

Appendix B

Photos of the samples

This appendix chapter displays photos of analyzed and treated spots of the samples treated with 2 laser settings. All the photos are taken at a x50 magnification and are $4514.4 \mu\text{m} \times 6019.2 \mu\text{m}$.

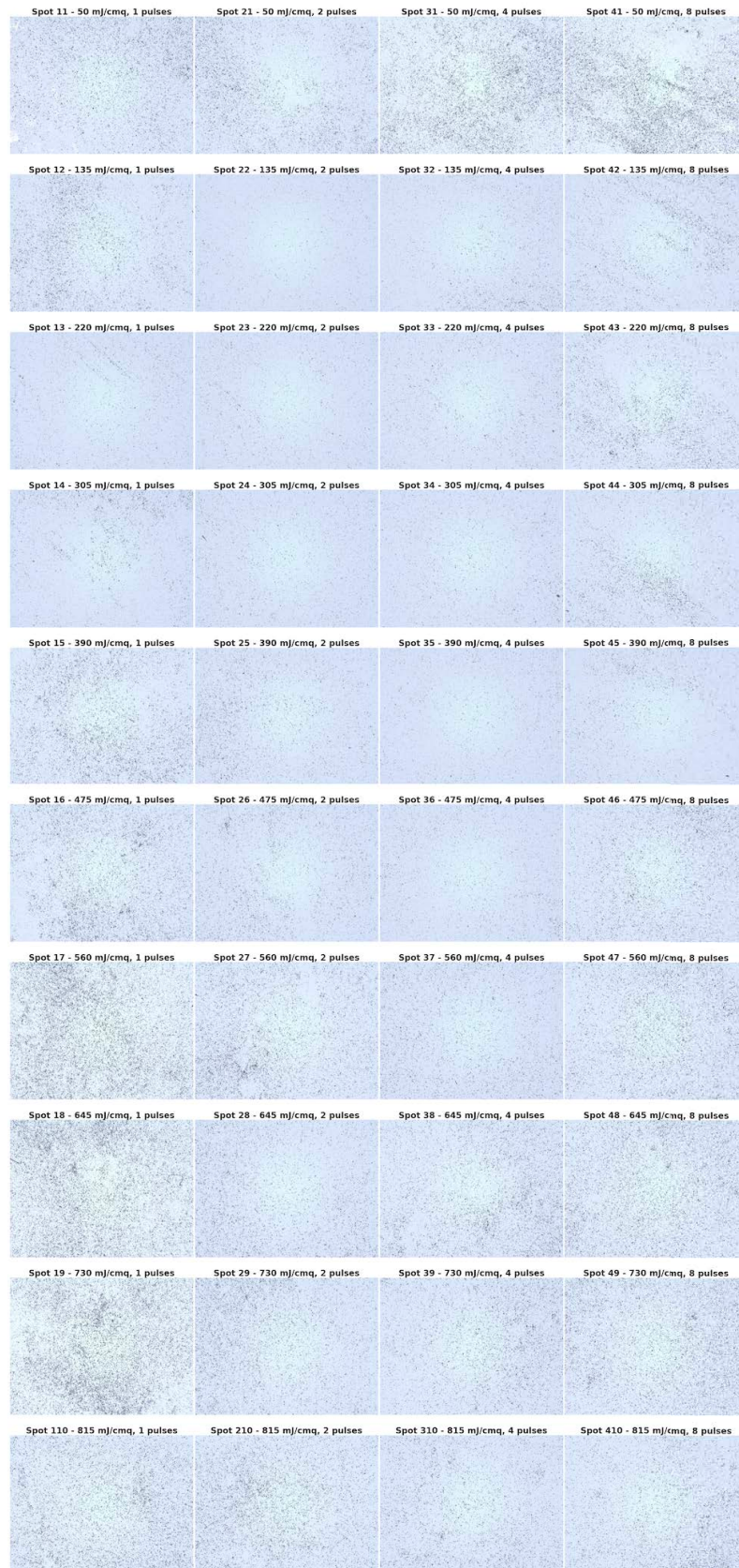
PRE photos - Mo, 2 settings

Figure B.1: Photos of the Mo sample treated with 2 laser settings before the laser process.

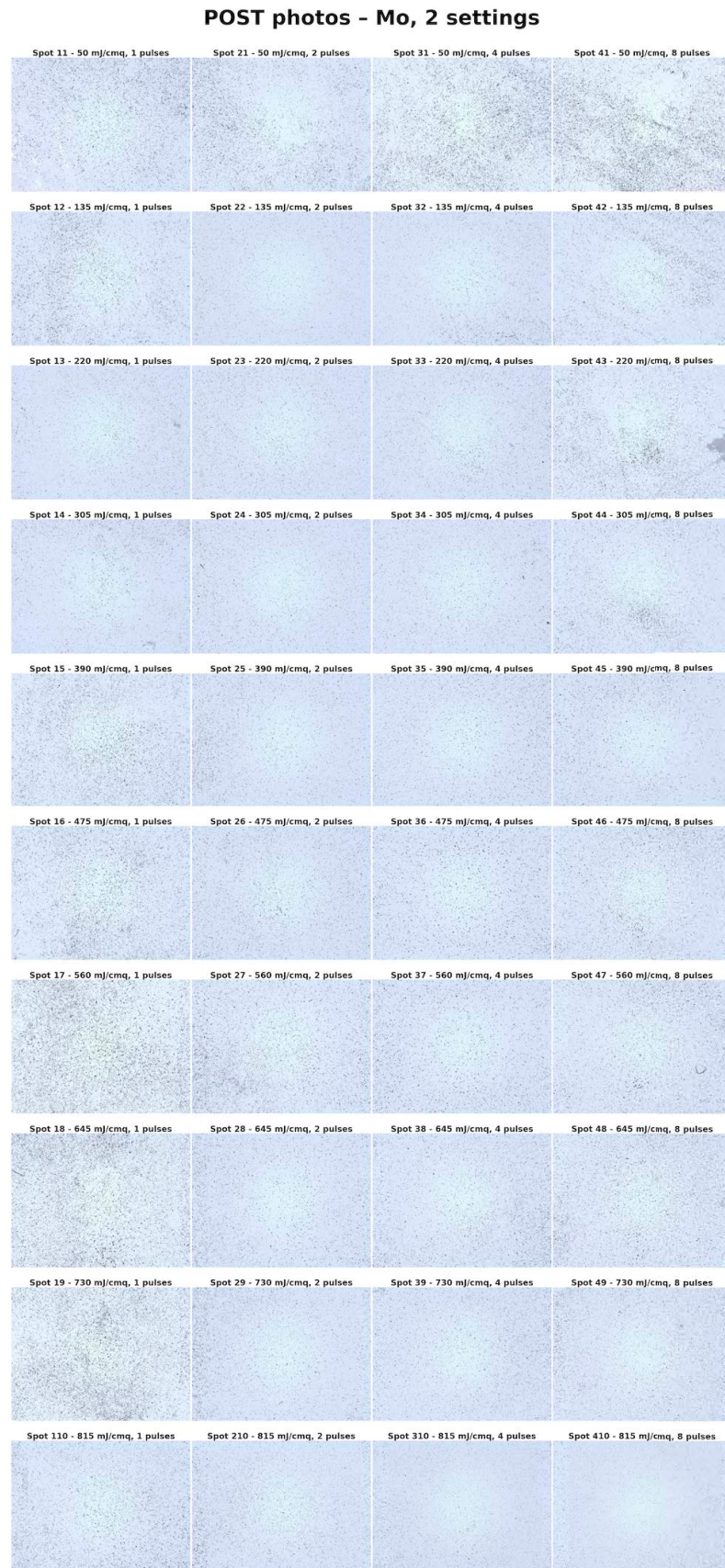


Figure B.2: Photos of the Mo sample treated with 2 laser settings after the laser process.

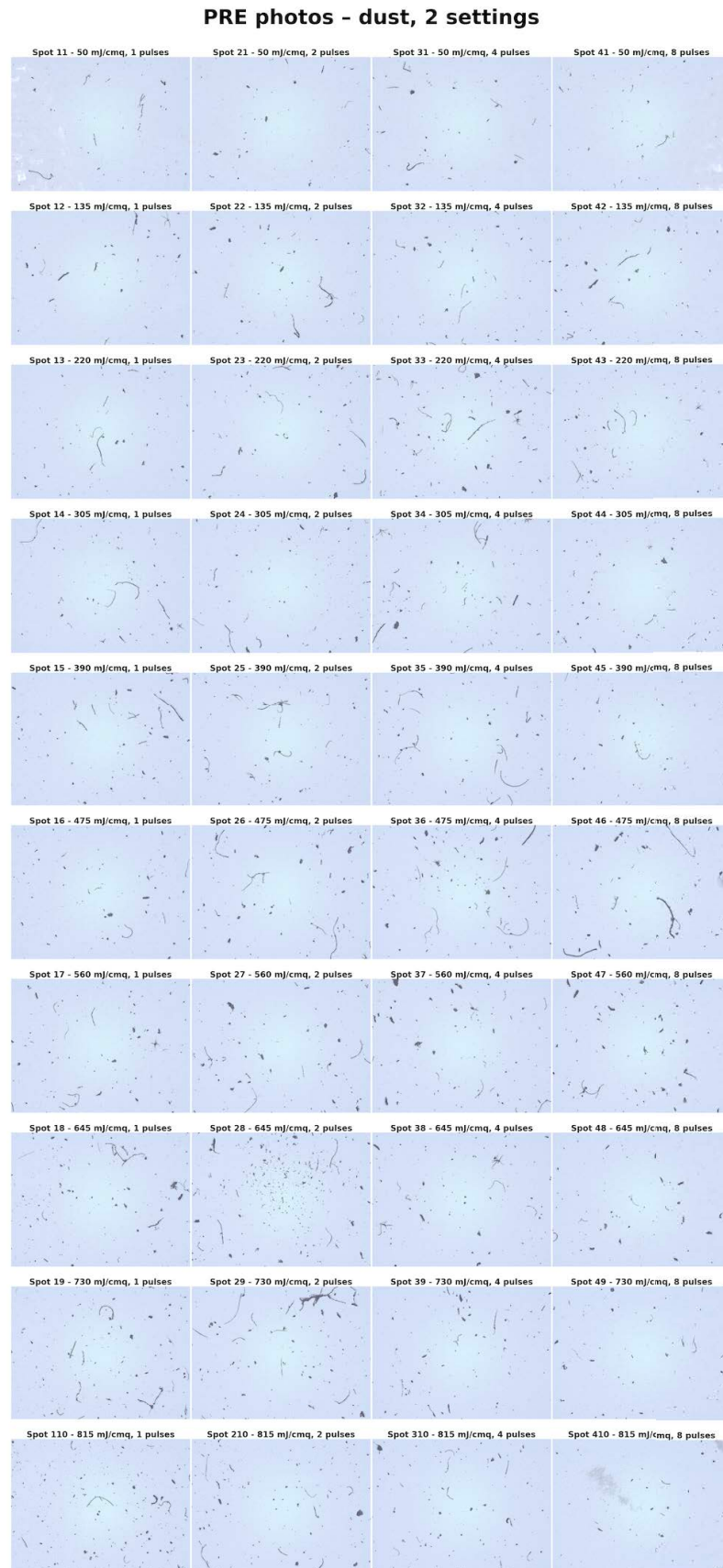


Figure B.3: Photos of the dust sample treated with 2 laser settings before the laser process.

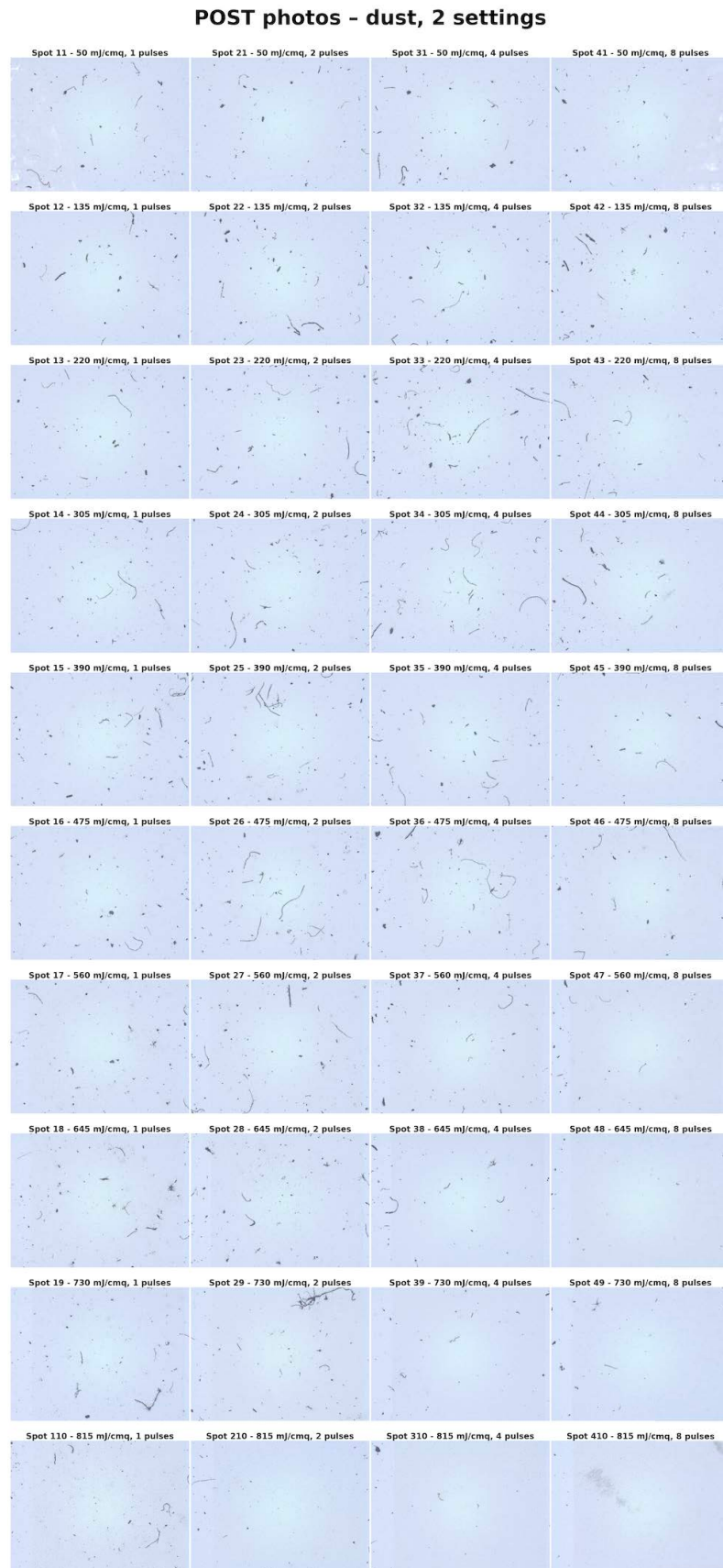


Figure B.4: Photos of the dust sample treated with 2 laser settings after the laser process.

Appendix C

Analysis plots

This appendix chapter shows additional plots that were not shown in the main text. Sect. C.1 includes all the analysis done at a luminosity threshold of 200.

Diameter distribution histogram - Mo sample, 2 settings - thr 160

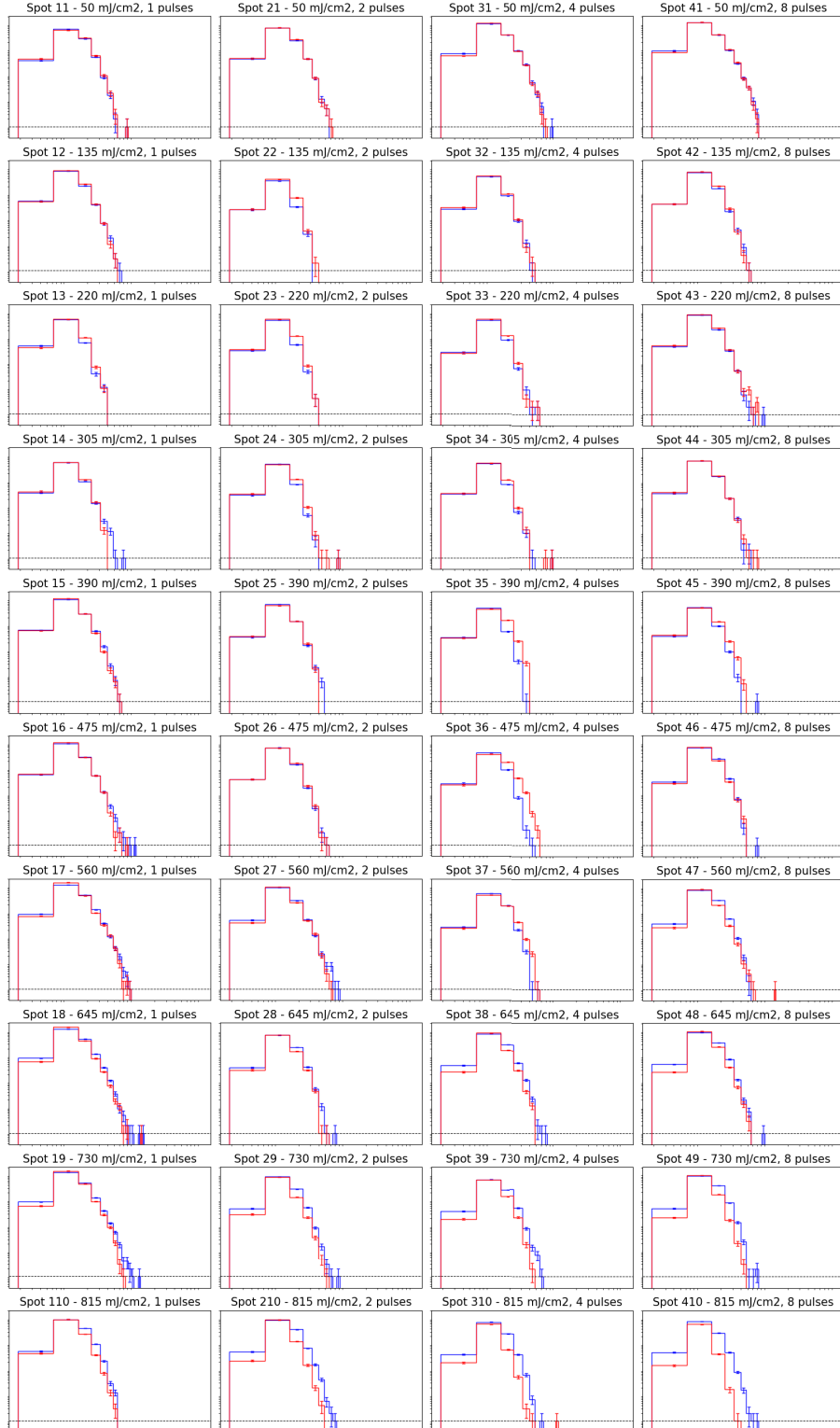


Figure C.1: Histograms of the size distribution for the Mo sample treated with 2 laser settings. The ED increases from top to bottom, the number of pulses increases from left to right. The distribution pre cleaning is shown in blue, post cleaning in red. The horizontal axis shows the diameter in log scale from 0 to $10^3 \mu\text{m}$ and the vertical axis shows the counts in log scale up to 10^4 . The dashed horizontal line corresponds to counts = 1.

Diameter distribution histogram - dust sample, 2 settings - thr 160

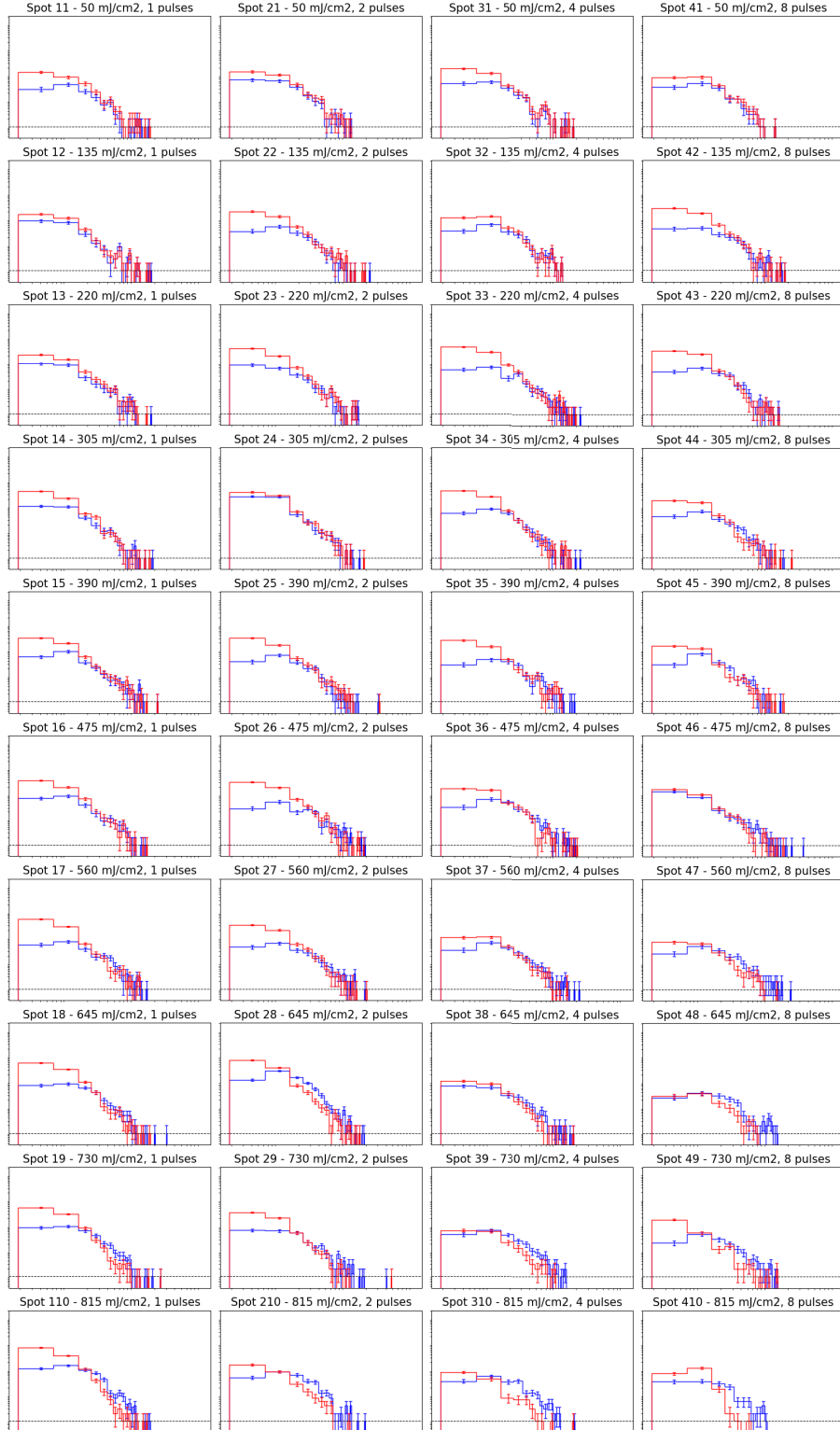


Figure C.2: Histograms of the size distribution for the dust sample treated with 2 laser settings. The ED increases from top to bottom, the number of pulses increases from left to right. The distribution pre cleaning is shown in blue, post cleaning in red. The horizontal axis shows the diameter in log scale from 0 to $10^3 \mu\text{m}$ and the vertical axis shows the counts in log scale up to 10^4 . The dashed horizontal line corresponds to counts = 1.

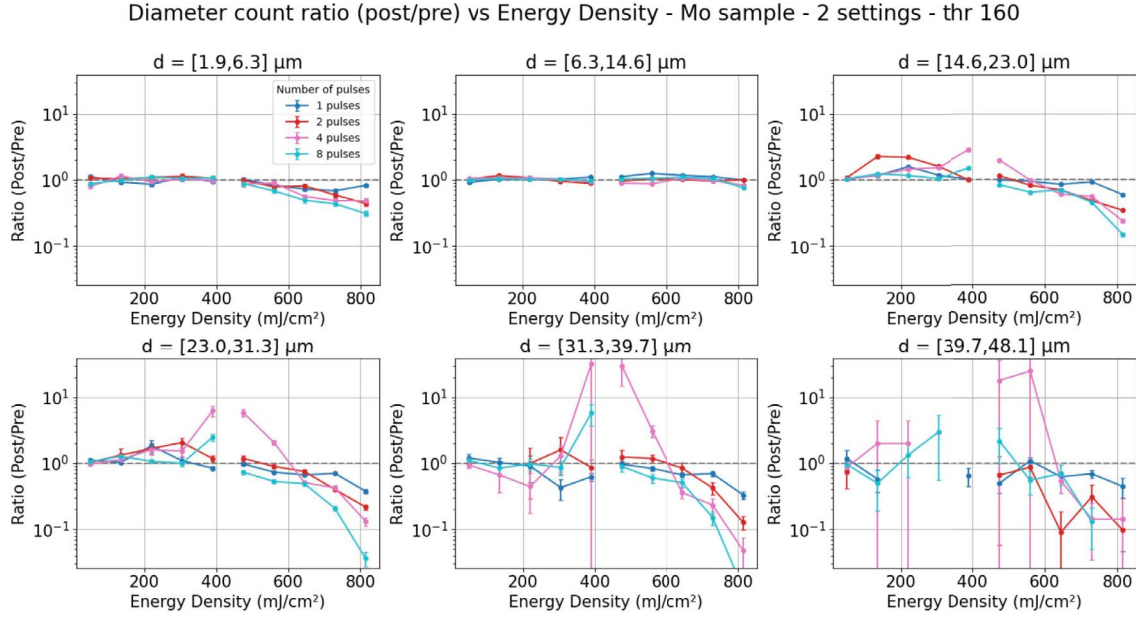


Figure C.3: NoP ratio vs the ED for different diameter ranges, for the Mo sample treated with 2 laser settings. Different colors correspond to different numbers of pulses.

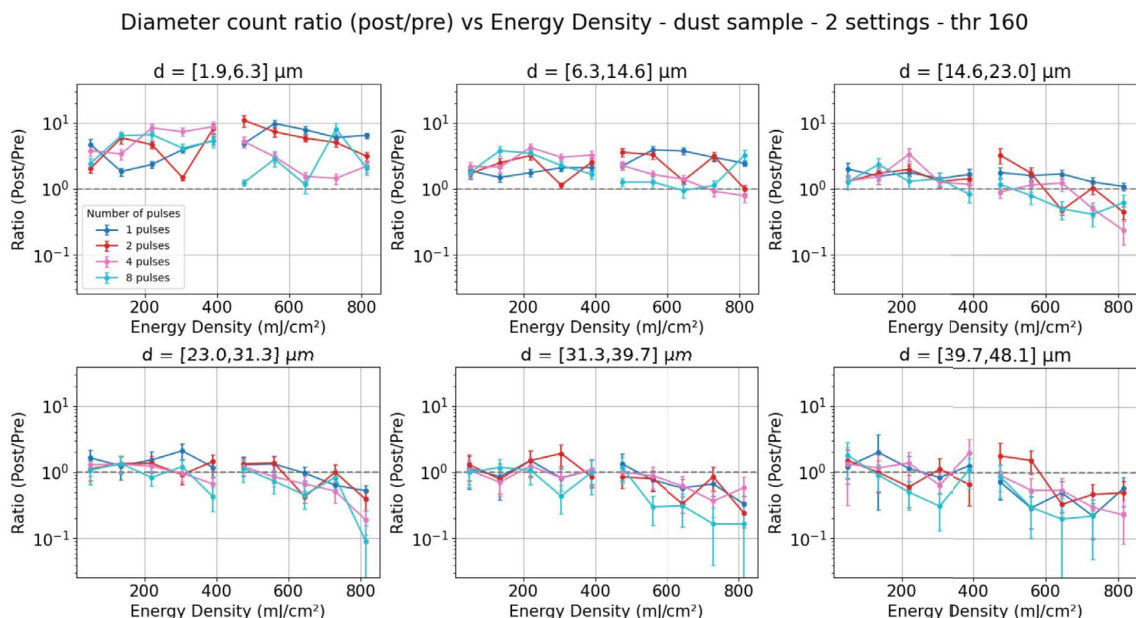


Figure C.4: NoP ratio vs the ED for different diameter ranges, for the dust sample treated with 2 laser settings. Different colors correspond to different numbers of pulses.

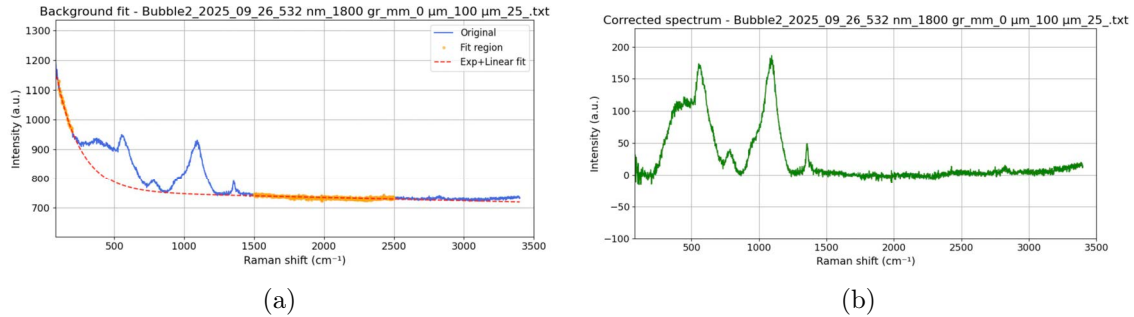


Figure C.5: Rounded particle Raman spectrum. (a): raw data (solid blue line) with the points used for the background fit (the yellow points) and the derived fit function to subtract (the dashed red line). (b): corrected spectrum (the fitted function subtracted from the raw data).

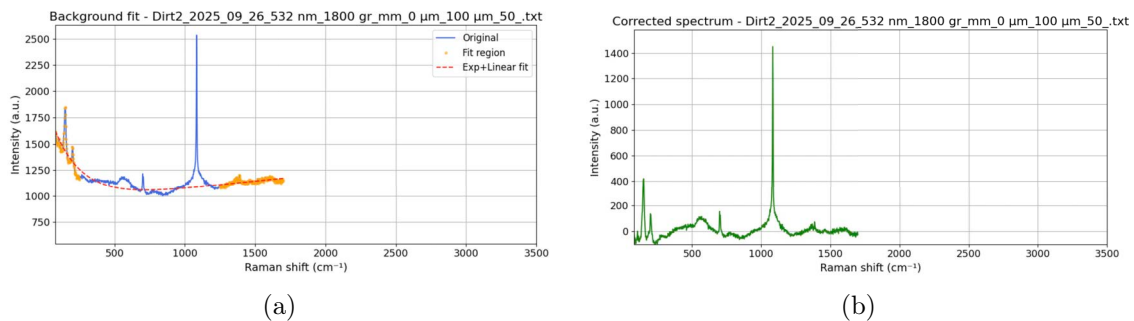


Figure C.6: Dust particle Raman spectrum. (a): raw data (solid blue line) with the points used for the background fit (the yellow points) and the derived fit function to subtract (the dashed red line). (b): corrected spectrum (the fitted function subtracted from the raw data).

C.1 Luminosity threshold 200 plots

In this appendix section the plots discussed in Chapter 6 are reported for a luminosity threshold of 200 instead of 160. This is the traditional value used for research on Si wafers.

C.1.1 PAC/NoP ratio

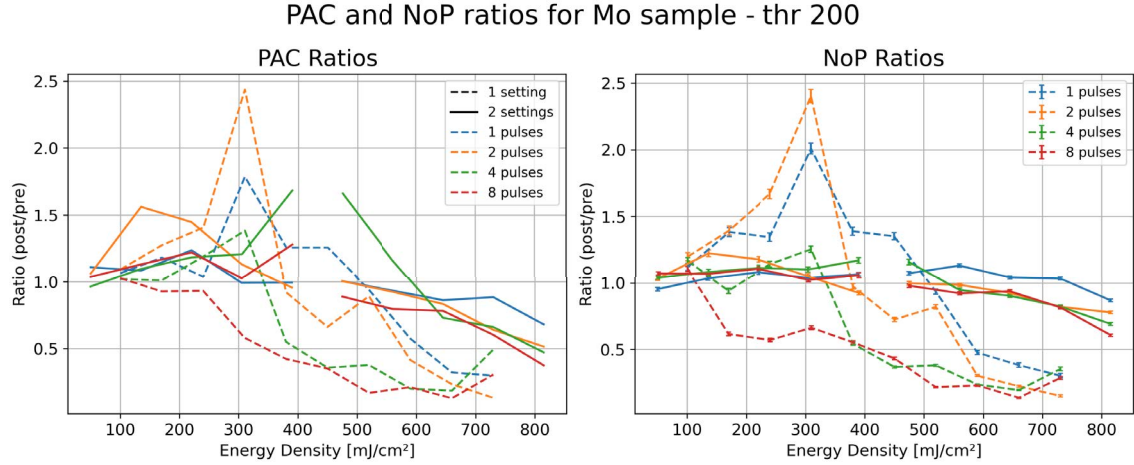


Figure C.7: PAC/NoP ratio versus the ED for the Mo samples with a luminosity threshold of 200. The dashed lines represent the sample treated with one laser setting, the solid line the one treated with two laser settings. Different colors correspond to different pulse numbers.

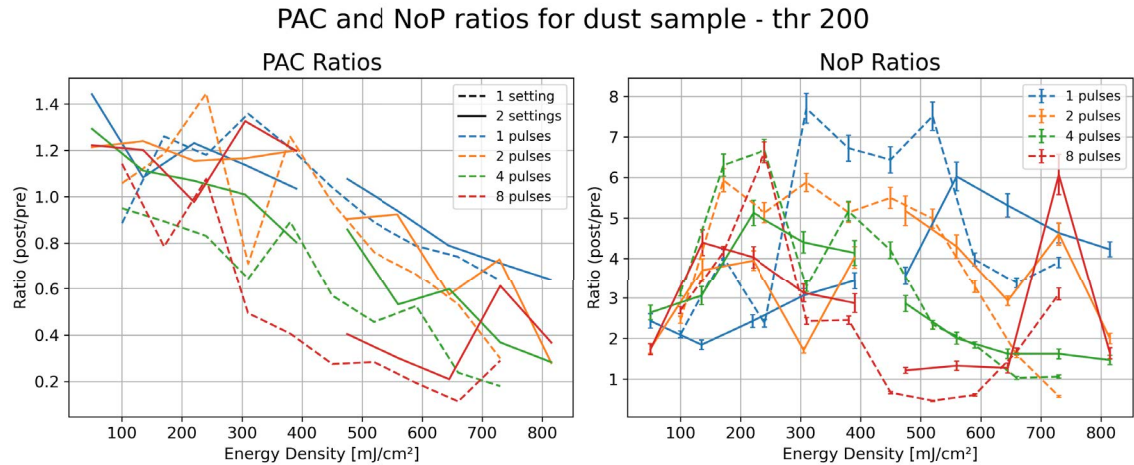


Figure C.8: PAC/NoP ratio versus the ED for the dust samples with a luminosity threshold of 200. The dashed lines represent the sample treated with one laser setting, the solid line the one treated with two laser settings. Different colors correspond to different pulse numbers.

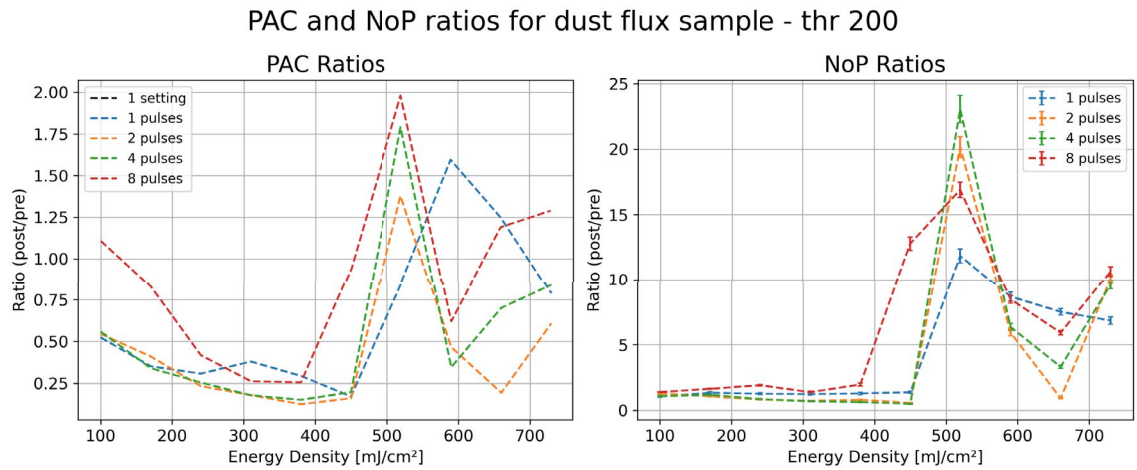


Figure C.9: PAC/NoP ratio versus the ED for the dust sample treated with N_2 flux with a luminosity threshold of 200. The dashed lines represent the sample treated with one laser setting, the solid line the one treated with two laser settings. Different colors correspond to different pulse numbers.

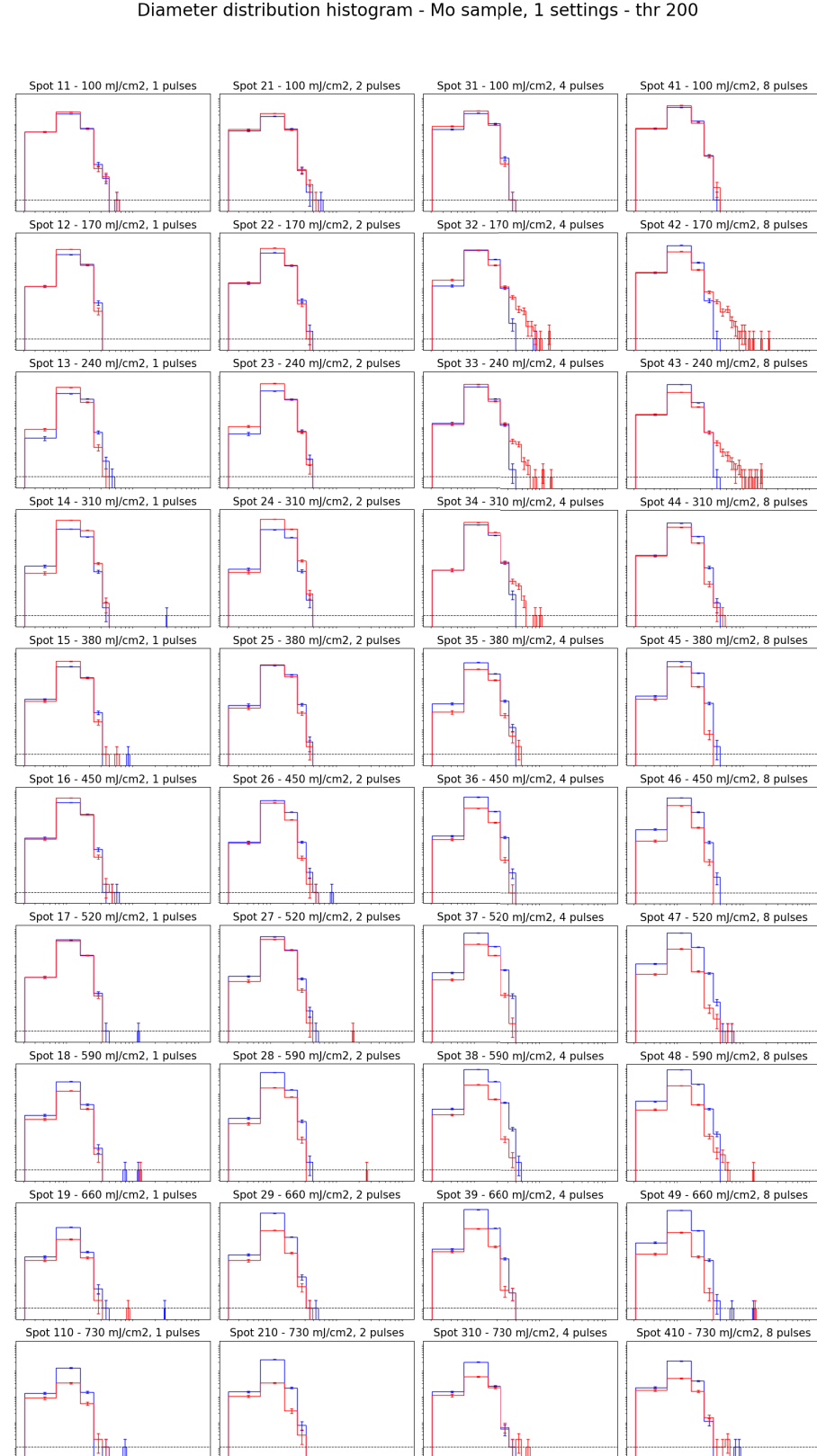


Figure C.10: Histograms of the size distribution for the Mo sample treated with 1 laser setting with a luminosity threshold of 200. The ED increases from top to bottom, the number of pulses increases from left to right. The distribution pre cleaning is shown in blue, post cleaning in red.

Diameter distribution histogram - dust sample, 1 settings - thr 200

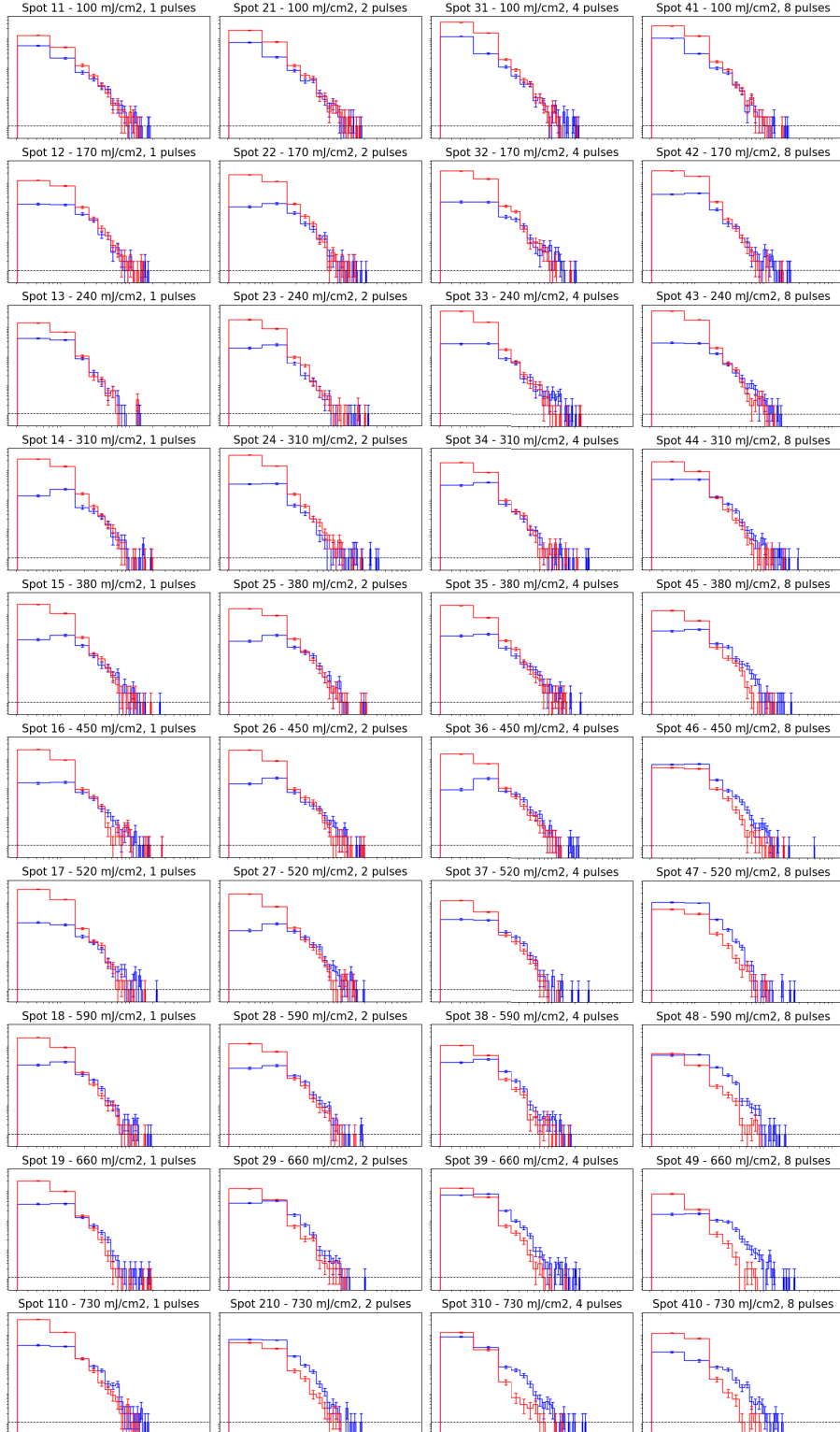


Figure C.11: Histograms of the size distribution for the dust sample treated with 1 laser setting with a luminosity threshold of 200. The ED increases from top to bottom, the number of pulses increases from left to right. The distribution pre cleaning is shown in blue, post cleaning in red.

Diameter distribution histogram - dust flux sample, 1 settings - thr 200

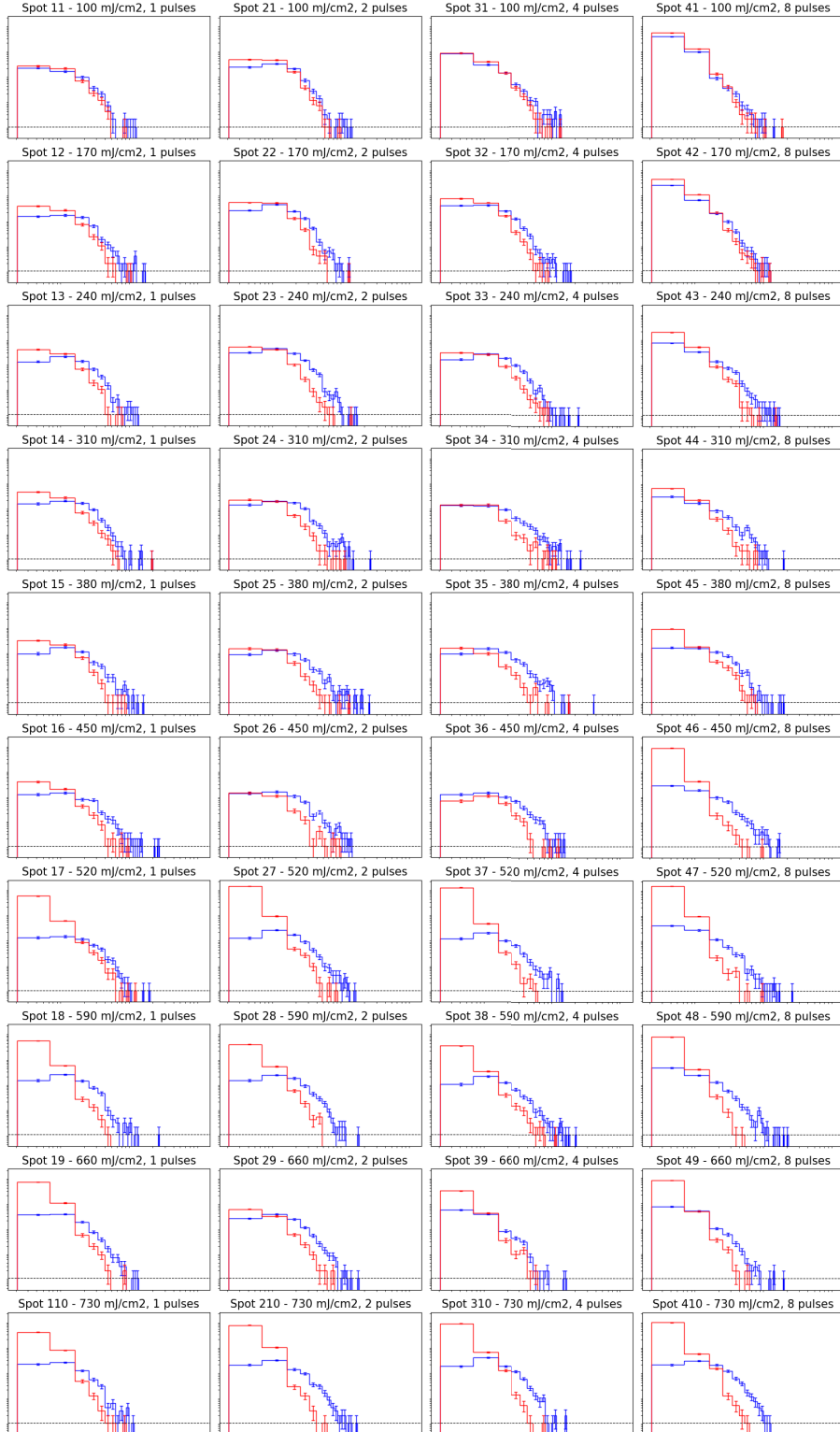


Figure C.12: Histograms of the size distribution for the dust sample treated with 1 laser setting, N₂ flux with a luminosity threshold of 200. The ED increases from top to bottom, the number of pulses increases from left to right. The distribution pre cleaning is shown in blue, post cleaning in red.

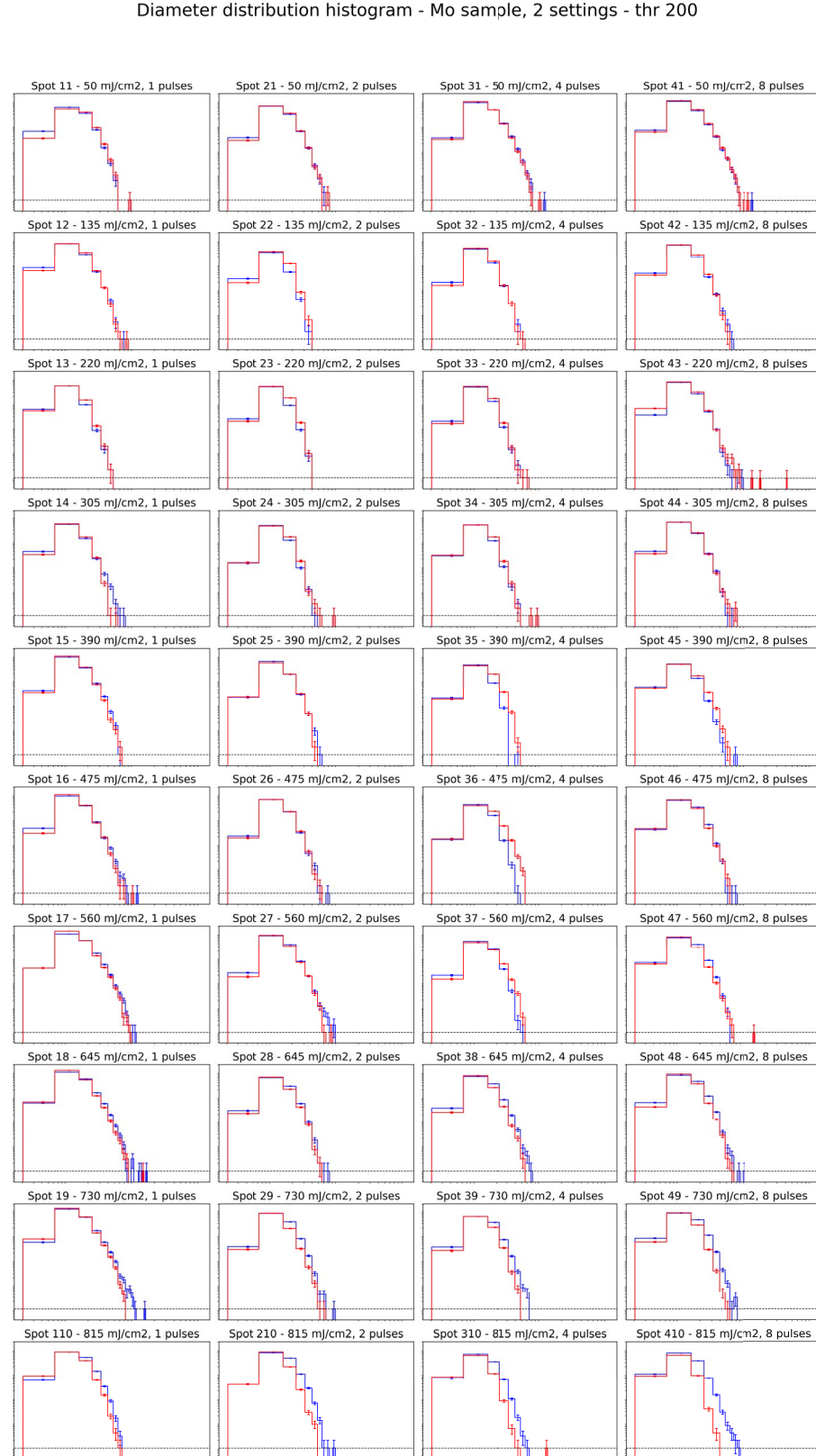


Figure C.13: Histograms of the size distribution for the Mo sample treated with 2 laser setting with a luminosity threshold of 200. The ED increases from top to bottom, the number of pulses increases from left to right. The distribution pre cleaning is shown in blue, post cleaning in red.

Diameter distribution histogram - dust sample, 2 settings - thr 200

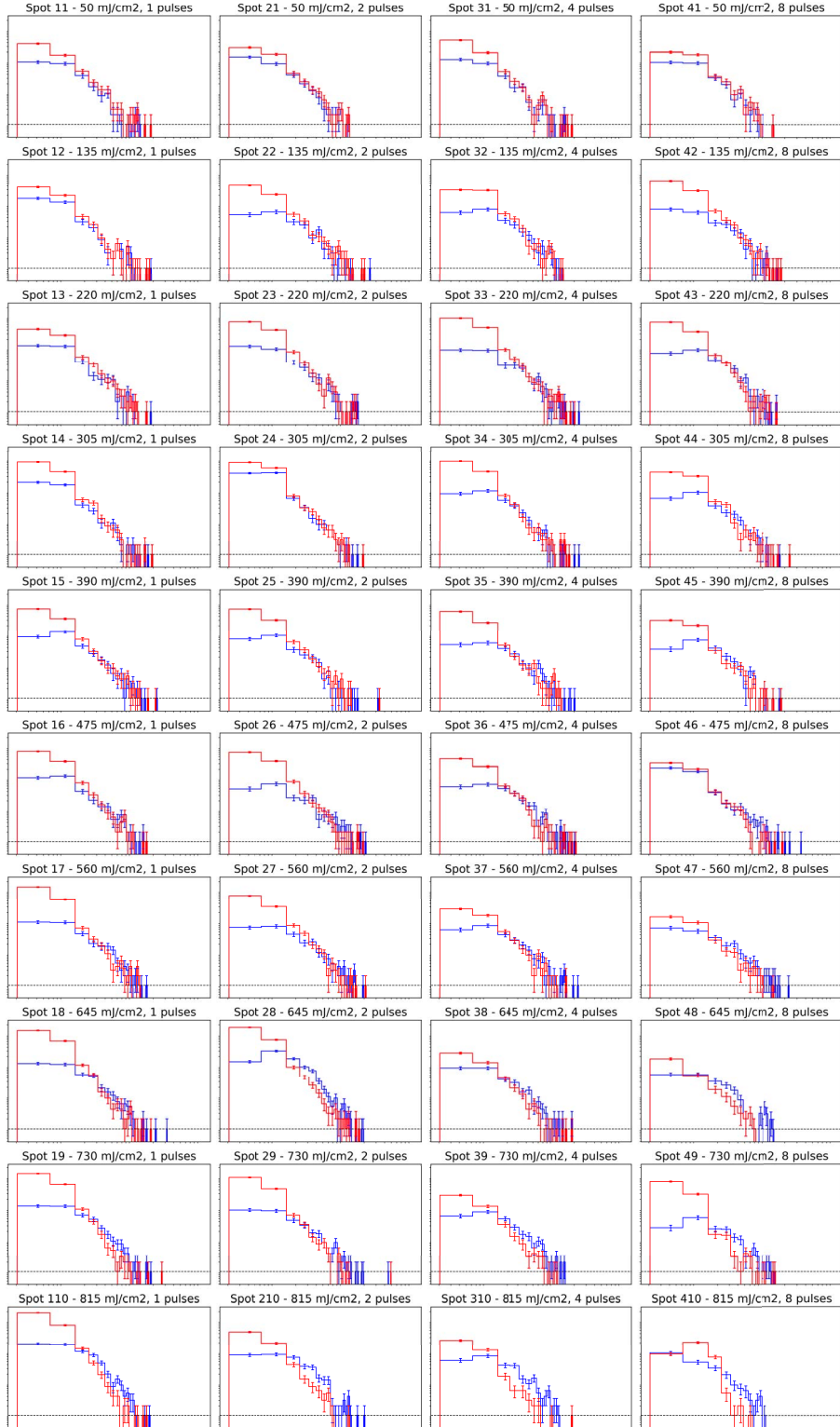


Figure C.14: Histograms of the size distribution for the dust sample treated with 2 laser setting with a luminosity threshold of 200. The ED increases from top to bottom, the number of pulses increases from left to right. The distribution pre cleaning is shown in blue, post cleaning in red.

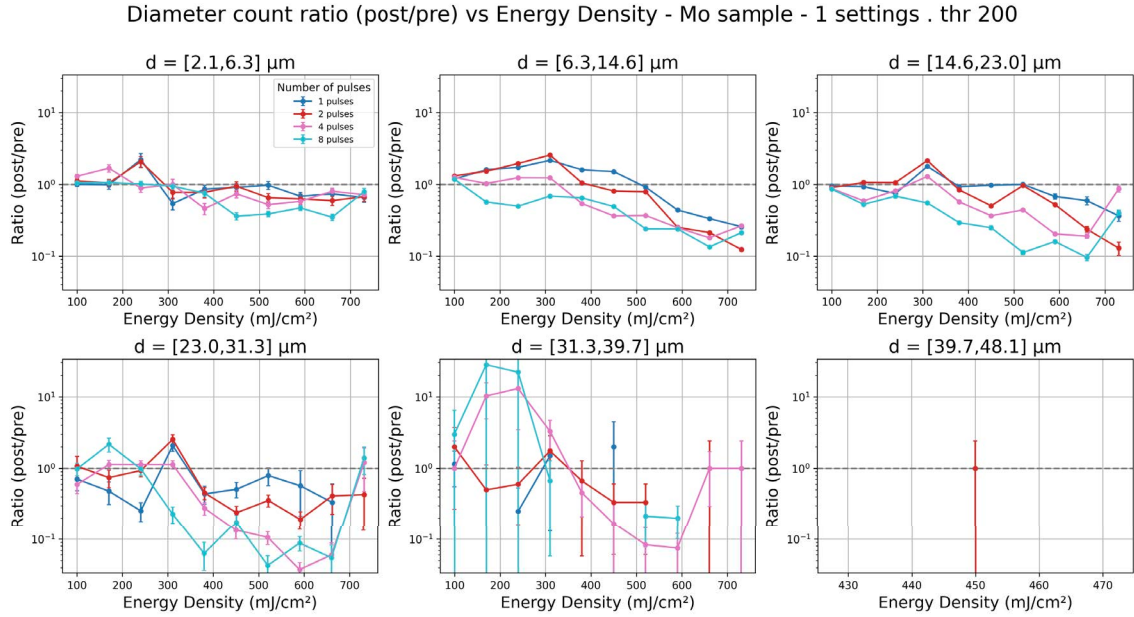


Figure C.15: NoP ratio versus ED for each diameter range, for different numbers of pulses. Plots for the Mo sample treated with 1 laser setting with a luminosity threshold of 200.

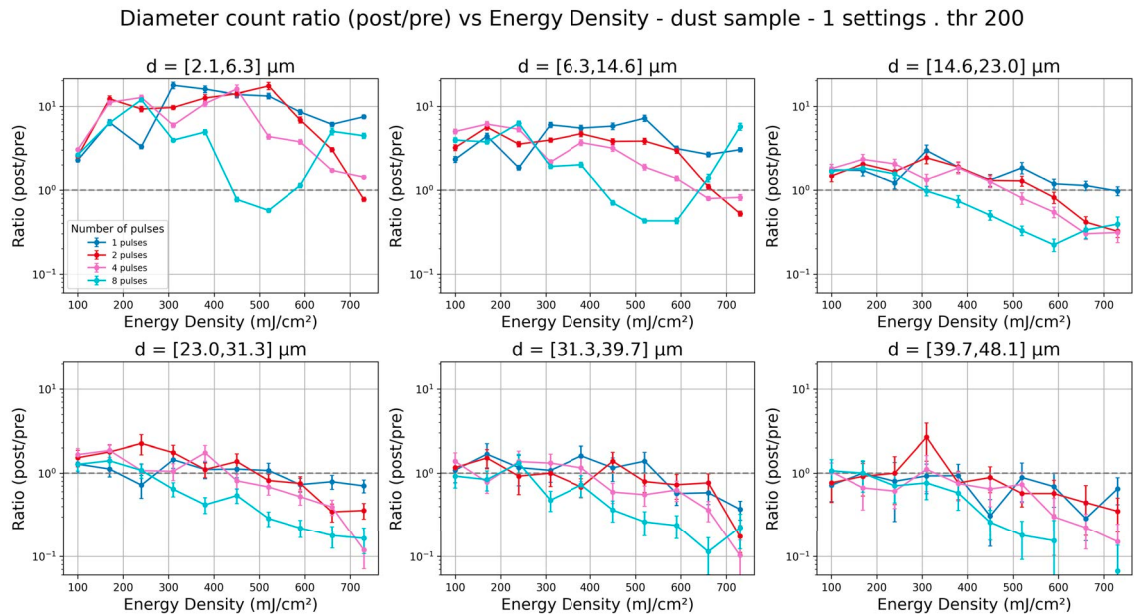


Figure C.16: NoP ratio versus ED for each diameter range, for different numbers of pulses. Plots for the dust sample treated with 1 laser setting with a luminosity threshold of 200.

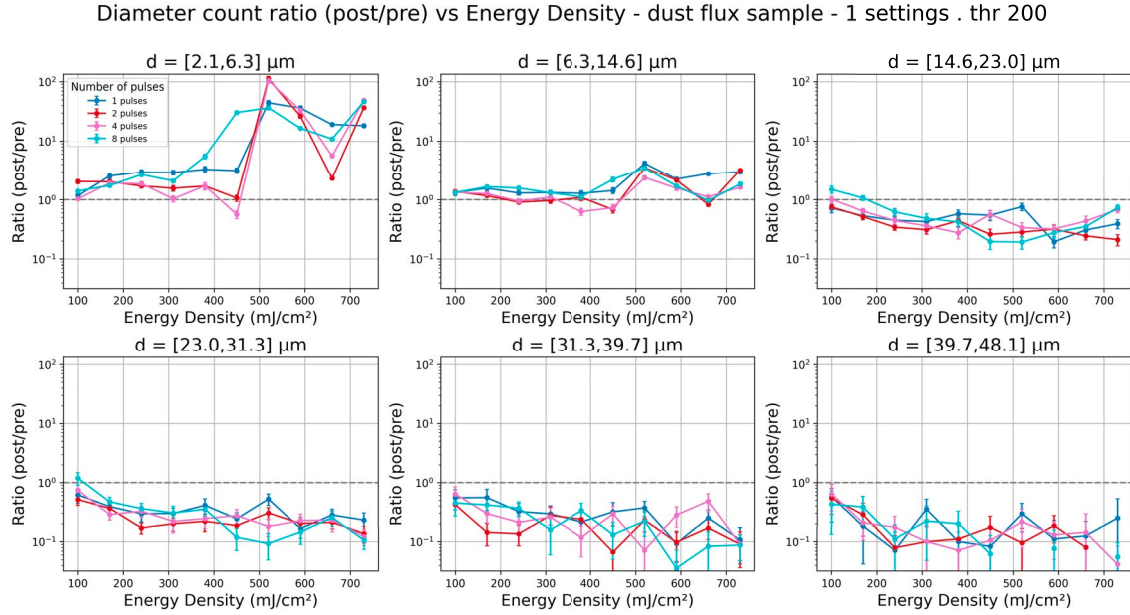


Figure C.17: NoP ratio versus ED for each diameter range, for different numbers of pulses. Plots for the dust sample treated with 1 laser setting and N_2 flux, with a luminosity threshold of 200.

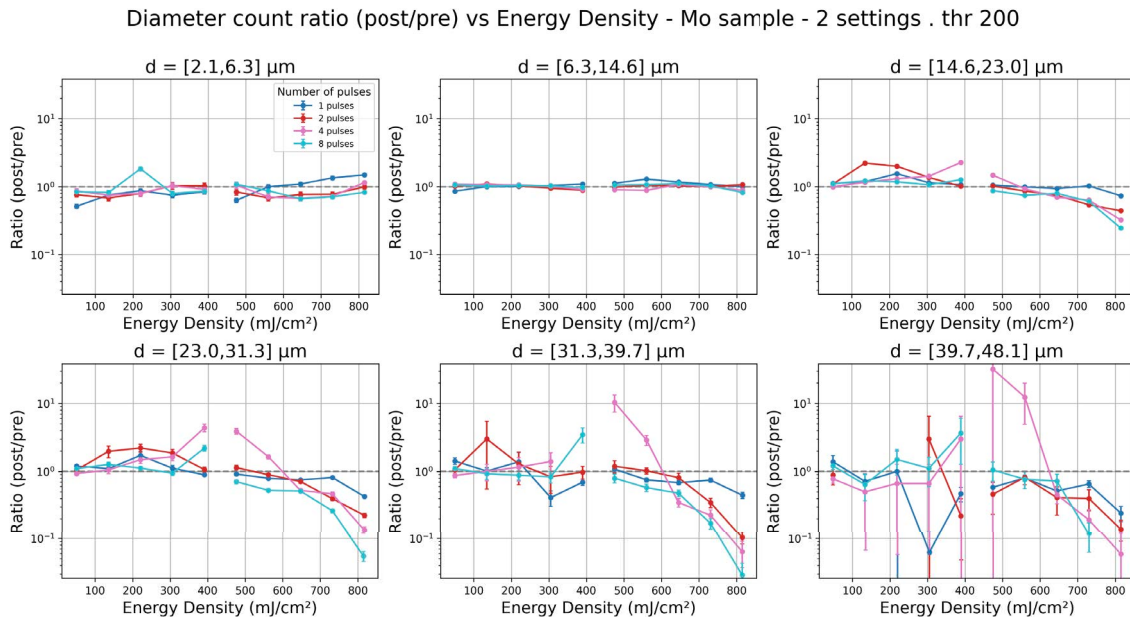


Figure C.18: NoP ratio versus ED for each diameter range, for different numbers of pulses. Plots for the Mo sample treated with 2 laser settings with a luminosity threshold of 200.

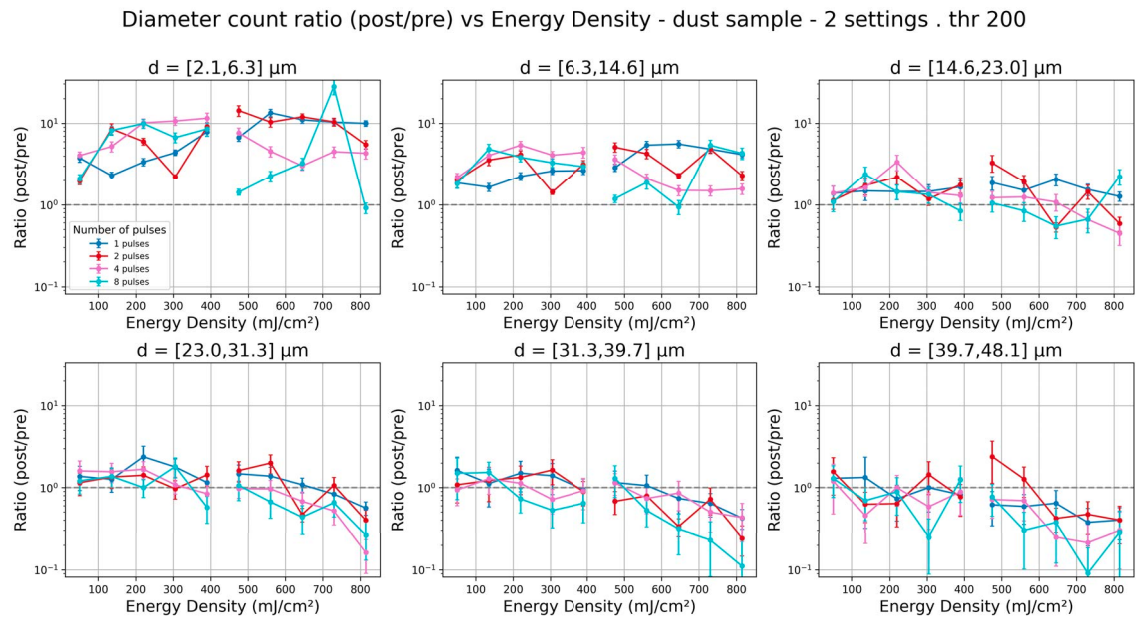


Figure C.19: NoP ratio versus ED for each diameter range, for different numbers of pulses. Plots for the dust sample treated with 2 laser settings with a luminosity threshold of 200.

Bibliography

- [1] LIGO Scientific Collaboration. *Why Detect Them?* <https://www.ligo.caltech.edu/page/why-detect-gw>. Accessed: 2025-09-11. n.d.
- [2] Andrea Moscatello. “Light Scattering from Dust Contamination in Gravitational-Wave Interferometric Detectors”. Supervisor: Giacomo Ciani, Co-supervisor: Livia Conti. Master’s thesis. Padova, Italy: Università degli Studi di Padova, 2022.
- [3] Edoardo Milotti. *The transverse-traceless gauge*. Lecture notes. Oct. 2024.
- [4] C. J. Moore D. Hilditch. *Gravitational Waves: Theory, Sources and Detection*. Technical Report / Course Notes EAG11. Instituto Superior Técnico, Universidade de Lisboa, 2018. URL: https://centra.tecnico.ulisboa.pt/media/cms_page_media/1140/EAG11_Gravitational_Waves.pdf.
- [5] Virgo Collaboration / Virgo Scientific Website. *Astrophysical Sources of Gravitational Waves*. [https://www.virgo-gw.eu/science/gw-universe astrophysical-sources-of-gw/](https://www.virgo-gw.eu/science/gw-universe	astrophysical-sources-of-gw/). Accessed: 2025-09-17. 2021.
- [6] Edoardo Milotti. *Compact Binary Coalescences*. Lecture notes. Dec. 2024.
- [7] KAGRA Collaboration LIGO Scientific Collaboration Virgo Collaboration. *GWTC: The Gravitational-Wave Transient Catalog*. <https://gwosc.org/eventapi/html/GWTC/>. Accessed: 2025-11-23. 2025.
- [8] European Gravitational Observatory (EGO). “*GWTC-4.0: Updated Gravitational Wave Catalog Released*”. <https://www.ego-gw.it/blog/2025/08/26/gwtc-4-0-updated-gravitational-wave-catalog-released/>. Accessed: 2025-11-23. Aug. 2025.
- [9] Charlotte Bond et al. “Interferometer techniques for gravitational-wave detection”. In: *Living Reviews in Relativity* 19.3 (2017). DOI: [10.1007/s41114-016-0002-8](https://doi.org/10.1007/s41114-016-0002-8). URL: <https://doi.org/10.1007/s41114-016-0002-8>.
- [10] Eric D. Black and Ryan N. Gutenkunst. “An introduction to signal extraction in interferometric gravitational wave detectors”. In: *American Journal of Physics* 71.4 (Apr. 2003), pp. 365–378. DOI: [10.1119/1.1531578](https://doi.org/10.1119/1.1531578).
- [11] Michele Maggiore. *Gravitational Waves. Vol. 1: Theory and Experiments*. Oxford University Press, 2007. ISBN: 978-0-19-171766-6, 978-0-19-852074-0. DOI: [10.1093/acprof:oso/9780198570745.001.0001](https://doi.org/10.1093/acprof:oso/9780198570745.001.0001).
- [12] Diego Bersanetti et al. “Advanced Virgo: Status of the Detector, Latest Results and Future Prospects”. In: *Universe* 7.9 (2021), p. 322. DOI: [10.3390/universe7090322](https://doi.org/10.3390/universe7090322). URL: <https://www.mdpi.com/2075-4434/7/9/322>.
- [13] Sheila E. Dwyer, Georgia L. Mansell, and Lee McCuller. “Squeezing in Gravitational Wave Detectors”. In: *Instruments* 6.1 (2022), p. 5. DOI: [10.3390/instruments6010005](https://doi.org/10.3390/instruments6010005). URL: <https://doi.org/10.3390/instruments6010005>.

- [14] Alessandro Longo et al. “Adaptive scattered light noise subtraction in GW detectors”. In: *Classical and Quantum Gravity* (2025). URL: <http://iopscience.iop.org/article/10.1088/1361-6382/ae0c50>.
- [15] Ronaldas Macas et al. “Impact of noise transients on low latency gravitational-wave event localization”. In: *Phys. Rev. D* 105 (10 May 2022), p. 103021. DOI: 10.1103/PhysRevD.105.103021. URL: <https://link.aps.org/doi/10.1103/PhysRevD.105.103021>.
- [16] Ronaldas Macas et al. “Impact of noise transients on low latency gravitational-wave event localization”. In: *Phys. Rev. D* 105 (2022), p. 103021. DOI: 10.1103/PhysRevD.105.103021.
- [17] Eric C. Fest. *Stray Light Analysis and Control*. SPIE Press, 2013.
- [18] Donald R. Huffman Craig F. Bohren. *Absorption and Scattering of Light by Small Particles*. John Wiley & Sons, Ltd, 1998. ISBN: 9783527618156. DOI: <https://doi.org/10.1002/9783527618156>. URL: <https://onlinelibrary.wiley.com/doi/abs/10.1002/9783527618156>.
- [19] Andrea Moscatello, Giacomo Ciani, and Livia Conti. *Scattered light noise due to dust particles contamination in the vacuum pipes of the Einstein Telescope*. 2025. arXiv: 2510.26919 [gr-qc]. URL: <https://arxiv.org/abs/2510.26919>.
- [20] Andrea Moscatello. “Stray Light from Particle Contamination in the Virgo and Einstein Telescope Gravitational Waves Detectors”. TDS: VIR-0914A-25. Doctoral Thesis. Università degli studi di Padova, 2025. URL: <https://tds.virgo-gw.eu/ql/?c=22097>.
- [21] Feng Song and Xuechun Lin. “Overview of Cleaning Technology”. In: *Laser Cleaning: Fundamentals and Applications*. Singapore: Springer Nature, 2024, pp. 1–35. ISBN: 978-981-97-6631-4. DOI: 10.1007/978-981-97-6631-4_1. URL: https://doi.org/10.1007/978-981-97-6631-4_1.
- [22] Francesco Sciortino. *Interaction Potentials Between Macroscopic Bodies*. Lecture notes, available online. Department of Physics, Sapienza University of Rome. 2023.
- [23] Daniel Maugis. “JKR and DMT Contact Model”. In: *Handbook of Nanophysics: Nanotubes and Nanowires*. Ed. by Klaus D. Sattler. CRC Press, 2010, pp. 9–1–9–17.
- [24] Bengt Kasemo. “Surface Forces”. In: *Theoretical Models for Surface Forces and Adhesion*. Springer Science & Business Media, 2013, pp. 169–210.
- [25] Feng Song and Xuechun Lin. “Overview of Cleaning Technology”. In: *Laser Cleaning: Fundamentals and Applications*. Singapore: Springer Nature, 2024, pp. 93–101. ISBN: 978-981-97-6631-4. DOI: 10.1007/978-981-97-6631-4_1. URL: https://doi.org/10.1007/978-981-97-6631-4_1.
- [26] Mihai Oane, M. Taca, and S. L. Tsao. “Two Temperature Model for Metals: A New “Radical” Approach”. In: *Lasers in Engineering* 00 (2013), pp. 1–9. URL: https://www.researchgate.net/publication/260436600_Two_Temperature_Model_for_Metals_A_New_Radical_Approach.
- [27] Zhihu Zhou et al. “The Fundamental Mechanisms of Laser Cleaning Technology and Its Typical Applications in Industry”. In: *Processes* 11.5 (2023), p. 1445. DOI: 10.3390/pr11051445. URL: <https://www.mdpi.com/2227-9717/11/5/1445>.
- [28] Y. -F. Lu et al. “Laser cleaning of micro-particles from a solid surface - theory and application”. In: *Materials Chemistry and Physics* 54 (1998), pp. 181–185.

- [29] Guodong Zhu et al. “Mechanism and application of laser cleaning: A review”. In: *Optics and Lasers in Engineering* 157 (2022), p. 107130. DOI: 10.1016/j.optlaseng.2022.107130.
- [30] Lidaris. *Laser-Induced Damage Threshold (LIDT)*. <https://lidaris.com/lidt-infobase/laser-induced-damage-threshold-lidt/>. Accessed: 2025-10-11.
- [31] ISP Optics. *Fused Silica UV Grade (SiO_2) Transmission Curve Datasheet*. Technical datasheet. ISP Optics. 2022. URL: <https://www.ispoptics.com/>.
- [32] Precision Portal. *Materials — Precision Portal Wiki*. Accessed: 12 November 2025. 2025. URL: <https://wiki.precisionportal.eu/materials/>.
- [33] Hilgenberg GmbH. *Precision Tubes and Optical Glasses – Technical Datasheet*. https://www.hilgenberg-gmbh.de/fileadmin/user_upload/PDF/HIL_Datenblatt_EN_0100_0522.pdf. Accessed: 2025-11-16. 2022.
- [34] Corning Incorporated. *HPFS® 7979, 7980, 8655 Fused Silica Optical Materials Product Information*. Product information sheet. Corning Incorporated. 2015. URL: <https://www.corning.com/worldwide/en/products/advanced-optics/product-materials/semiconductor-laser-optic-components/high-purity-fused-silica.html>.
- [35] Mikhail Polyanskiy. *RefractiveIndex.INFO — Refractive index database*. Accessed shelf: GLASS-glasses; book: Soda lime glass; page: Kamptner et al. 2024: n, k 0.191 - 1.69 um. 2025. URL: <https://refractiveindex.info> (visited on 11/14/2025).
- [36] Advanced Technical Products. *All About Soda Lime Glass: Composition and Properties*. Accessed: 26 October 2025. 2024. URL: <https://advancedtechnicalprod.com/industry-news-blog/all-about-soda-lime-glass-composition-and-properties/>.
- [37] AZoM. *Molybdenum (Mo) – Properties, Applications*. Accessed on October 26, 2025. 2001. URL: <https://www.azom.com/properties.aspx?ArticleID=616> (visited on 10/26/2025).
- [38] Nuclear Power. *Molybdenum – Specific Heat, Latent Heat of Fusion, Latent Heat of Vaporization*. Accessed on October 26, 2025. 2021. URL: <https://www.nuclear-power.com/molybdenum-specific-heat-latent-heat-vaporization-fusion/> (visited on 10/26/2025).
- [39] P. Tolias. *Non-retarded room temperature Hamaker constants between elemental metals*. arXiv preprint arXiv:2003.00571. v3. 2020. URL: <https://arxiv.org/abs/2003.00571>.
- [40] *Hamaker constants (A) for several materials*. https://www.researchgate.net/figure/Hamaker-constants-A-in-10-20-J-for-several-materials_tbl1_274625177. Accessed: 2025-11-30.
- [41] Jacob N. Israelachvili. “Intermolecular and Surface Forces”. In: *Intermolecular and Surface Forces*. 3rd ed. San Diego: Academic Press, 2011. Chap. 13.
- [42] David S Bradshaw and David L Andrews. “Manipulating particles with light: radiation and gradient forces”. In: *European Journal of Physics* 38.3 (Mar. 2017), p. 034008. DOI: 10.1088/1361-6404/aa6050. URL: <https://doi.org/10.1088/1361-6404/aa6050>.
- [43] Alessandro Tonon. “Synthesis of MoS₂ thin films by pulsed laser processing”. Master’s thesis. Padova, Italy: Università degli Studi di Padova, 2022. URL: <https://hdl.handle.net/20.500.12608/34673>.

- [44] Keyence Corporation. *VHX-7000 Digital Microscope User Manual*. Document No. 96M16688. 2021. URL: https://cores.research.asu.edu/sites/default/files/2021-12/AS_114992_VHX-7000 UM_96M16688_WW_GB_2110_1.pdf.
- [45] A. Moscatello, C. Leoni. *Virgo logbook entry 2815*. <http://virgolab.physics.unitn.it/logbook/?r=2815>. 2025-07-25.
- [46] Paul L. Rosin and Jovisa Zunic. “2D Shape Measures for Computer Vision”. In: *Handbook of Mathematical Models in Computer Vision*. Springer, 2008. Chap. 12, pp. 289–309. DOI: 10.1002/9780470175668.ch12. URL: https://www.researchgate.net/publication/27651396_2D_Shape_Measures_for_Computer_Vision.
- [47] Valeria Milotti. “Controlled Direct Synthesis of Graphene Nanoribbons without Metal Catalyst”. Doctoral Thesis. University of Vienna, 2021.
- [48] HORIBA. *XploRA PLUS Raman Spectrometer Brochure*. Brochure. HORIBA Scientific. 2023. URL: https://static.horiba.com/fileadmin/Horiba/Products/Scientific/Molecular_and_Microanalysis/XPLORA_SERIES/XploRA_PLUS/XploRA-PLUS-Raman-Spectrometer-Brochure.pdf.